DISCLAIMER:

This document does not meet the
current format guidelines of
the Graduate School at
The University of Texas at Austin.

It has been published for
informational use only.

The Thesis Committee for Kumar Sundaram Das
Certifies that this is the approved version of the following thesis:

Gas-hydrates saturation estimation in Krishna-Godavari basin, India

APPROVED BY
SUPERVISING COMMITTEE:

Supervisor:

Mrinal K. Sen

Robert Tatham

Kyle Spikes

Gas-hydrates saturation estimation in Krishna-Godavari basin, India

by

Kumar Sundaram Das, M.S.

Thesis

Presented to the Faculty of the Graduate School of

The University of Texas at Austin

in Partial Fulfillment

of the Requirements

for the Degree of

Master of Science in Geologic Sciences

The University of Texas at Austin

May 2013

Dedication

Dedicated to my family, my teachers, my friends and Austin.

Acknowledgements

Last two years in Austin have been a great learning experience for me. This journey would not have been possible without some of the most wonderful people, who I have met and learnt from during this time.

To my mentor Dr.Mrinal Sen, I express my deepest gratitude for accepting me under his tutelage and being a perennial source of inspiration. I have gained immensely from his vast knowledge and experience. His constant support and guidance has made this work possible.

I would like to acknowledge Dr. Robert Tatham and Dr.Kyle Spikes, for their suggestions on perfecting my thesis and for serving on my MS thesis committee.

I am grateful to Dr.Kalachand Sain and the National Geophysical Research Institute, India for making this project possible. A major portion of my research was carried out at the gas hydrates group at NGRI. For the successful completion of the project a lot of credit goes to Dr.Sain, for he provided me with the data and means to complete this project. Without his support my stay at NGRI would not have been possible.

I thank Dr. Maheshwar Ojha and Dr. Ranjana Ghosh for helping me out at each and every step during my stay at NGRI. I'd also like to thank Dr. N.Satyavani who has been of great help during my work. I shall cherish sweet memories of new friendships that I developed at NGRI in the warm Indian summer.

I'd forever be grateful to the Jackson school of geosciences and University of Texas at Austin, for helping me realize my dream of a graduate degree and also for the help in my development as a researcher. I also appreciate the staff at UT, especially Philip Guerrero, for being of such great help in almost any matter.

I'm also grateful to my friends for making my stay in Austin so memorable and as always to my family who mean everything to me.

Abstract

Gas-hydrates saturation estimation in Krishna-Godavari basin, India

by

Kumar Sundaram Das, M.S. Geo. Sci.

The University of Texas at Austin, 2013

Supervisor: Mrinal K. Sen

Gas hydrates are an unconventional energy resource. They may become an important source of energy for India in the future. They occur offshore along the continental margin. They are currently in exploratory and evaluation stages and their quantification is an important task. The goal of this thesis is to demonstrate a new technique for the estimation of gas hydrates volumes. The region of study is the Krishna-Godavari basin. It is located on the eastern offshore areas of India. The presence of gas hydrates has been proven by drilling into marine sediments as a part of the Indian National Gas Hydrates Program. Borehole subsurface and surface seismic data were collected during this expedition. I use a 2D seismic reflection line and borehole log data for my study. The method I use for estimation of gas hydrates saturation uses a combination of inversion of seismic reflection data and development of seismic attributes. My approach can be broadly described by following steps:

1. Process the seismic data to remove noise. Use stacked and migrated data along with well logs to perform poststack seismic inversion to obtain impedance information in volumetric portions of the subsurface.
2. Use NMO corrected CDP gather records of the seismic reflection data along with subsurface well logs to perform prestack seismic inversion to obtain impedance volumes.
3. Compare the results from step1 and step 2 and use the best results to perform multi-attribute analysis using a neural network method to predict resistivity and porosity logs at the well location. Use the transform equations obtained at the well location to predict the well logs throughout the seismic section in the desired zone of interest.
4. Use an anisotropic equivalent of Archie's law that relates resistivity and porosity to saturation to predict saturation throughout the seismic reflection section.

The majority of the previous work done in the region is limited to gas hydrates quantification only at the well location. By using neural networks for multi-attribute analysis, I have demonstrated a statistical based method for the prediction of log properties away from well location. My results suggest gas hydrates saturation in the range of 50-80% in the zone of interest. The estimated saturation of gas hydrates matches up very closely with the saturation estimates obtained from the cores recovered during coring of the boreholes. Hence my method provides a reliable method of quantification of gas hydrates by making best possible use of seismic and well log data. The unique combination of impedance derived attributes and neural-network includes the non-linear behavior in the predictive transform relationships. The use of an anisotropic formulation of Archie's law to estimate saturation also produces accurate results confirmed with the observed gas-hydrates saturation.

Table of Contents

List of Tables

List of Figures

Chapter 1: Introduction

This chapter introduces gas hydrates and discusses some of their physical properties. I also present the occurrences of gas hydrates in different parts of the globe. This is followed by a discussion of some of the geophysical methods used to explore for gas hydrates, which provides the background for the exploration and resource quantification of gas hydrates from surface seismic observations. My research focuses on gas hydrate exploration in the offshore areas of India. Therefore, I include discussion on a gas-hydrates project undertaken by the Indian government, and the data that were collected in the expedition that are used in my study. I then briefly present the motivation behind my current work and objectives, and then I layout the chapter-by-chapter progression of my thesis.

1.1 GAS HYDRATES PROPERTIES AND PRESENCE

Gas hydrates are naturally occurring compounds that form when methane is trapped within a crystalline structure of water or ice. They are also known as methane hydrates or clathrates. Clathrates are a class of chemical substances formed by the inclusion of different molecules in the molecular structure of another molecule (Giavarini and Keith, 2011). A schematic representation of a gas hydrate molecular structure, shown in Figure 1.1, depicts a spherical gas molecule trapped within a cage-like structure made of water molecules that are bonded together by hydrogen bonds. The trapped molecules are free to move within the cage-like structure. The hydrate structure is stabilized by an attractive van der Waals force that acts between the guest molecule and the water molecules (Giavarini and Keith, 2011). Three necessary conditions for the formation of gas hydrates (Giavarini and Keith (2011) are 1) presence of sufficient water, 2) the presence of guest molecules such as methane, ethane, carbon dioxide or another gas

molecule that can fit within the cage structure of hydrates, 3) a thermodynamically stable range of pressure and temperature conditions for the occurrence of gas hydrates, which are typically high pressure and low temperature values. Phase diagrams (Figure 1.2) display the pressure (depth) and temperature conditions under which gas hydrates are stable. The figure includes two scenarios in which gas hydrates have been reported in permafrost and marine environments (Riedel et al., 2010). The scenarios have different thermal gradients. Gas hydrates are stable at pressure and temperature conditions in the range between the phase boundary of gas hydrates and the geothermal gradient of the region. The depth range over which gas-hydrates are stable is known as the gas hydrates stability zone (GHSZ). From the examples for gas hydrates occurrence presented in Figure 1.2, the depth and temperature values required for formation of gas hydrates in a permafrost region are 200-1050m and -10^{o} - $+15^{o}$C. In marine locations the GHSZ occurs when the seafloor depth is greater than 1200m, and the required depth and temperature values are 1200-1500m and 5^{o}- $+15^{o}$C. The pressure and temperature conditions favorable for the formation of gas hydrates are typically found within a few hundreds of meters of the unconsolidated sediments on the continental shelf (Riedel et al., 2010).

Figure 1.3 shows known occurrences of gas hydrates around the world. Worldwide occurrences of gas hydrates have been reported in both continental margins and permafrost regions (Markl et al., 1970; Stoll et al., 1971; Bily and Dick, 1974; Neave et al., 1978; Shipley et al., 1979). Major marine drilling operations including the Ocean Drilling Program (ODP) and Integrated Ocean Drilling Program (IODP) have confirmed the occurrence of gas hydrates in deep-water sediments along the continental margins. Examples include the Cascadia Margin (Westbrook et al., 1994; Tréhu et al., 2003; Riedel et al., 2006), and the Blake Ridge (Paull et al., 1996). Ocean drilling projects carried out by the national gas hydrates exploration programs in Japan (e.g., Fuji et al.,

2008), India (Collett et al., 2008), China (Yang et al., 2008) and Korea (Park et al., 2008) and the Gulf of Mexico (Boswell et al., 2009) have also shown the presence of gas hydrates in continental slopes. In permafrost regions, the Mallik well has proven the presence of gas hydrates (Dallimore et al., 1999; Dallimore and Collett, 2005).

1.2 GEOPHYSICAL PROPERTIES OF GAS HYDRATES

Geophysical methods have become an important tool for exploration of gas hydrates. Some of the reasons that justify (Riedel et al., 2010) the importance of using geophysical exploration methods are indirect assessments of the resource potential of gas hydrates (concentration of gas hydrates), mapping the geographical extent of gas hydrates reserves in a region (depth and area), understanding the physical conditions required for gas hydrates formation (depth and temperature), and investigation of the reservoir type and quality (lithology, porosity and permeability) (Reidel et al., 2010)

Gas hydrates have quite anomalous physical properties that make them readily detectable using surface geophysical techniques. Table 1 describes the physical properties of gas hydrates, in comparison to water. The P-wave velocity and density of pure synthetic methane hydrates from laboratory experiments are, respectively, 3300 m/s and 0.90 g/cc (Waite et al., 2000). The density of gas hydrate is very close to that of water, but its compressional velocity is more than double of that of water. Formation of gas hydrates replaces water from the pore space of sediments with solid gas hydrates, which causes a reduction in porosity and a significant increase in the elastic moduli of the bulk host rock. This causes an increase of the compressional and shear seismic wave velocities (Yuan et al., 1996). An alternate explanation that has been proposed for the mechanism explains the increase in velocities of sediments with gas hydrates is when gas hydrates act as cementing material for the grains of the rock, thus becoming a part of the load bearing

frame of the rock, leading to an increase in bulk and shear moduli of the rock (for example, Helgerud et al., 1999; Chand et al., 2004; and Sava and Hardage, 2006).

Surface seismic and bore-hole well log observations are commonly used geophysical methods for the identification of gas hydrates. One of the most prominent markers in surface seismic observations for gas hydrates in marine sediments is the bottom simulating reflector (BSR) on the seismic reflection sections, which often coincides with the base of the GHSZ. It is a physical boundary across which there is a major change in the physical properties. Figure 1.4 is a marine seismic reflection profile from the Krishna-Godavari basin, the location of this study. The BSR can be identified as the reflection event that cuts across the geological reflectors on the section (yellow line). Because the base of the gas hydrates stability zone (GHSZ) is controlled by pressure and temperature, the BSR has the unusual characteristic of mimicking the bathymetry of the seafloor due to the drop in impedance from the base of the GHSZ to the underlying sediments. The BSR also has a polarity opposite to that of the seafloor reflection. The figure also shows enhanced reflectivity observed below the BSR. This can be attributed to the underlying free gas. Drastic changes in pore-space filling material above the BSR, the gas hydrates and below the BSR, free gas, causes a large P-impedance change across the BSR. Because the seismic P-wave energy reflected back from any interface is directly proportional to the impedance change, the amplitude of the P-wave reflected back at the BSR is large compared to other reflectors, causing a bright amplitude event which can be observed on the P-P surface seismic data.

Well log data are also useful in demarcating gas hydrate zones. Figure 1.5 shows logging while drilling (LWD) well logs recorded in the region of study. Borehole data from LWD technology uses sensors placed on the drill bit to collect data at regular intervals from a borehole during the drilling operation (Evans, 1991). They provide in

situ measurements of physical properties of the sediments through which the bit is passing. Some of the LWD logs commonly used for identification of gas hydrates are the porosity, resistivity and sonic velocity (Riedel et al., 2010). Commonly used well log properties as indicators for presence of gas hydrates are high electrical resistivity and high P-wave velocity (Mathews, 1986; Collett, 1993; Goldberg, 1997; Collett and Ladd, 2000; Guerin and Goldberg, 2002; Murray et al., 2006). Because gas hydrates are highly resistive to the flow of electrical current (Makogon, 1997), their presence is conspicuous in the resistivity logs. A comparison of the resistivity well log in Figure 1.5 shows clear deflection in the electrical resistivity in the gas hydrates stability zone (GHSZ). The region with gas hydrates has electrical resistivity of at least two orders of magnitude greater than overlying and underlying sediments. Gas hydrates have considerably higher bulk and shear moduli than water (Helgerud et al., 2009); hence their presence increases the P- and S-wave velocities of the sediments in which they are formed. An example of this is depicted in Figure 1.5 where a significant change (+7%) in the P-wave velocity obtained from the sonic log can be observed. The values of 1750-1800 m/s are well below the values of 3500 m/s for pure hydrates which are related to an interaction of the gas-hydrates with the sediments. However, because gas hydrates and water have very similar densities, no significant change is observed in the density log.

Constituents	K (GPa)	G (GPa)	ρ (g/cm^3)	Vp (m/s)	Vs (m/s)
Gas Hydrate	8.27	3.49	0.922	3545	1945
Water	2.29	0	1.000	1513	-

Table 1.1: Comparison of physical constants of water and gas hydrates. The values for gas hydrates and water are valid at 11^{o}C and 1 MPa (Helgerud et al., 2009). Vp and Vs are calculated from the physical parameters.

1.3 GAS HYDRATES SCENARIO IN INDIA

Gas hydrates have an important role to play in the energy scenario of India (Sain and Gupta, 2008; 2012). Because India depends chiefly on imports of oil and gas to meet its energy demands, future energy security includes the potential for a source of energy that may be harnessed. With the goal to investigate the occurrences of gas hydrates in India, the Indian National Gas Hydrate Program (NGHP), Expedition 01, was designed and executed (Collett et al., 2008). It was aimed at understanding the geologic and geochemical factors affecting the formation of gas hydrates along the coast of the Indian Peninsula and convergent margins near the Andaman Islands region. Downhole logging and coring surveys were conducted to confirm the presence of gas hydrates. Logging while drilling (LWD) was conducted while drilling 12 holes at 10 locations, and post-drilling wireline logging was conducted at 13 other drill sites. Core samples were collected from 21 holes. Temperature gradients were measured at 11 locations. These observations confirmed the presence of multiple thick zones of gas hydrate accumulation in Krishna-Godavari basin, Andaman Islands and Mahanadi Basin (Figure 1.6).

1.4 REGION OF STUDY

The region of study for my thesis is the Krishna-Godavari basin located in the eastern margin of India (Figure 1.6). The locations of the seismic line (Figure 1.4) and the borehole log data (Figure 1.5) are also shown in this figure. The Krishna-Godavari (KG) basin is a passive rift margin on the eastern coast of India. It developed as a result of the rifting and drifting of the Indian plate from the Antarctica-Australian plate during the late Jurassic and Early Cretaceous.(Shastri et al., 1981; Biksham and Subrwhmanyam, 1988). It covers an area of 24,000 km^2 on the onshore and 145,000 km^2 in the offshore region. The NE-SW trending horst and graben fault systems from the late Jurassic rift cut across the older NW-SE trending Permian-Triassic Gondwana grabens, which include the

Mahanadi and Pranhita-Godavari grabens (Shastri et al., 1981). A map showing the region of study is marked with a black boundary in the Figure 1.6.

1.5 DATA

Both seismic reflection and well log data were used in this study. The seismic data used here is a high resolution NW-SE 2D seismic line in the Krishna- Godavari basin as shown in Figure 1.4, with the general location shown in Figure 1.6. Both seismic and borehole well-log data were provided by the gas-hydrate group at National Geophysical Research Institute (NGRI), India, during my short visit there. The digital time sampling interval of seismic reflection data was 1 ms. The shortest source-receiver distance was 70m. The shot and receiver intervals were at 12.5 m, and the recording length was 4s. The data were acquired using a 1500m long streamer comprising 120 channels and a 320 in^3 air gun array, yielding 60 CMP fold coverage. As seen in Figure 1.4, the BSR can be identified with its characteristic bright amplitude and a polarity opposite to that of the seafloor, cutting across the dipping reflectors in the NE section of the profile. The BSR is not clear in the mid-section of the seismic profile, but careful viewing of the data reveals a faint signature of the BSR in the SW section of the seismic line.

The borehole logs used for the present study (see Figure 1.5 and location in Figure 1.6) are from a well drilled during the NHGP Expedition 01 (Collett et al., 2008). It is not exactly situated along the seismic line used for the present study. It has its nearest location to CDP 490 on the 2D seismic line and is offset 30 m from the 2D line(Figure 1.4). Logging while drilling (LWD) was begun at a depth of 1049m and continued upto a total depth of 2103.5m. Although many log measurements were taken during well logging, I used only the sonic, resistivity (deep), neutron porosity, and density logs for

the purpose of my study. Figure 1.5 shows some of the logs used in the study, which were recorded during the drilling of well 10A in NGHP Expedition 01.

1.6 MOTIVATION AND OBJECTIVE

Gas hydrates with their worldwide presence, are increasingly gaining importance as a future energy resource (Kvenvolden, 1993).The determination of the quantity of gas hydrates is an important step in the process of the exploration of gas hydrates because it would help in understanding of gas hydrates energy supply potential. Accurate methods of quantification of amount of gas hydrates in this scenario become important as the present estimates of total in place methane resources from laboratory and field studies have great uncertainties (Milkov, 2004; Klauda and Sandler, 2005).

Different methods have been used to estimate gas hydrates saturation. Some of these methods are based on estimating gas hydrates saturation from seismic velocities, described, in detail, in a review paper by Sain et al. (2008; 2012). Some of the examples of this type of approach are found in Wood et al.,(1994), Yuan et al., (1996), Korenaga et al., (1997), Lee et al., (1993,1996). The drawback of these methods is that the relationship used to relate the gas hydrates saturation to seismic P-wave velocity does not have a physical basis (Ecker et al., 2000). Some other approaches use rock physics models to predict saturation, for example, Ecker et al., (2000), Chand et al., (2006). Rock physics models do not always correctly estimate the gas hydrates saturation because the effect of gas hydrates on elastic properties of the host rocks is not well understood (Lu and McMechan, 2002). The amplitude versus angle (AVA) analysis of surface seismic data was used for determination of seismic velocities and hence gas hydrates saturation estimation by Ojha et al., (2008; 2010). They applied AVA modeling to a seismic data set

in the Kerala-Konkan basin, India. They found that in the gas-hydrates bearing sediemnts P and S-wave velocities are 2245m/s and 895 m/s respectively. The gas-hydrates saturation obtained using these values were in the range 0.22-0.38. Well logs have been used for quantification of gas hydrates by Collet (2000), Lee and Collett (2005), Lee and Waite (2008) and Lee and Collett (2009). The drawback of well log based methods for quantification of gas hydrates is that they are limited to the estimation of gas hydrates saturation only at actual well locations.

The chief objective of my thesis is the estimation of gas hydrates saturation along the profile of the 2D seismic line in Figure 1.4. I have adopted a novel method using both surface seismic and subsurface log data to estimate gas hydrates saturation. The salient features of the present study are the use of statistical methods for saturation estimation and also the inclusion of anisotropic behavior of electrical resistivity in Archie's law (Archie, 1942) to predict gas hydrates saturation.

The method I used includes P-impedance and S-impedance obtained from inversion of surface seismic data and the use of them in a statistical multi-attribute analysis of surface seismic data using EMERGE®, a log prediction module in the commercially available Hampson-Russell® seismic analysis package. This application is an industrial version of an inversion software application, to predict equivalent log properties at all trace locations on the seismic profile. The concept is to find a statistical relationship between a limited number of multiple seismic attributes, selected from a large number of attributes using a multi-variate analysis scheme, obtained from the surface seismic data. The desired log property is then derived from log data at the well location using EMERGE®, a neural network analysis tool available in Hampson-Russell® software package. The derived transform equations are then applied to predict the log property at all seismic-trace locations on the seismic profile from the seismic

attributes. The log properties that I have estimated along the seismic profile are the electrical resistivity and neutron porosity. To include anisotropy as a factor affecting gas hydrates saturation, I extend the work done by Lee and Collett (2009) on estimation of gas hydrates saturation at the well location using an anisotropic Archie's law (Archie, 1942) applied to the estimated resistivity and porosity results and extend it to the estimation of gas hydrates saturation along the whole seismic section.

1.7 THESIS OUTLINE

In Chapter 2, I describe processing and inversion the 2D post-stack seismic data from the region of study to obtain P-impedance. I include a brief investigation of the effect of the initial low frequency impedance model on the final impedance results. Chapter 3 is the application of a prestack inversion technique to the same 2D seismic data that I used in Chapter 2, to obtain P and S impedances. A comparison of the P-impedance results obtained from Chapter 2 and Chapter 3 gives me an idea of the better impedance results. In Chapter 4, I present the prediction of porosity and resistivity logs using the attributes calculated from the P-impedance obtained from prestack inversion in Chapter 3. For well log prediction I use the multi attribute analysis and neural network applications available in the Hampson-Russell® software system. I use the well log properties thus predicted to estimate gas hydrates saturation using the modified Archie's law from Lee and Collett, 2009. I conclude with discussions of the results in Chapter 5.

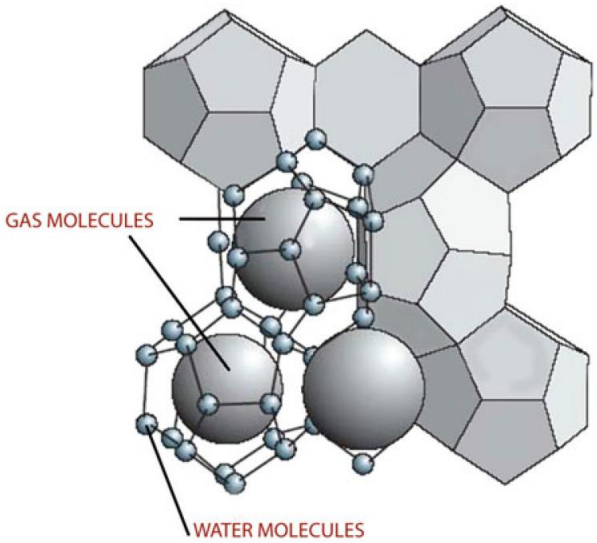

Figure 1.1: Schematic diagram of gas hydrate molecules (from Giavarini and Keith, 2011). Spherical gas molecules (e.g., methane, ethane, propane or CO_2) are trapped in the cage like structure of the water molecule. The trapped gas molecules are stabilized within the water molecules by van der Waals forces acting between the gas molecules and water. The necessary conditions required for the formation of gas hydrates are the presence of sufficient amount of water, the presence of guest molecules like as methane, carbon dioxide and the appropriate pressure and temperature conditions.

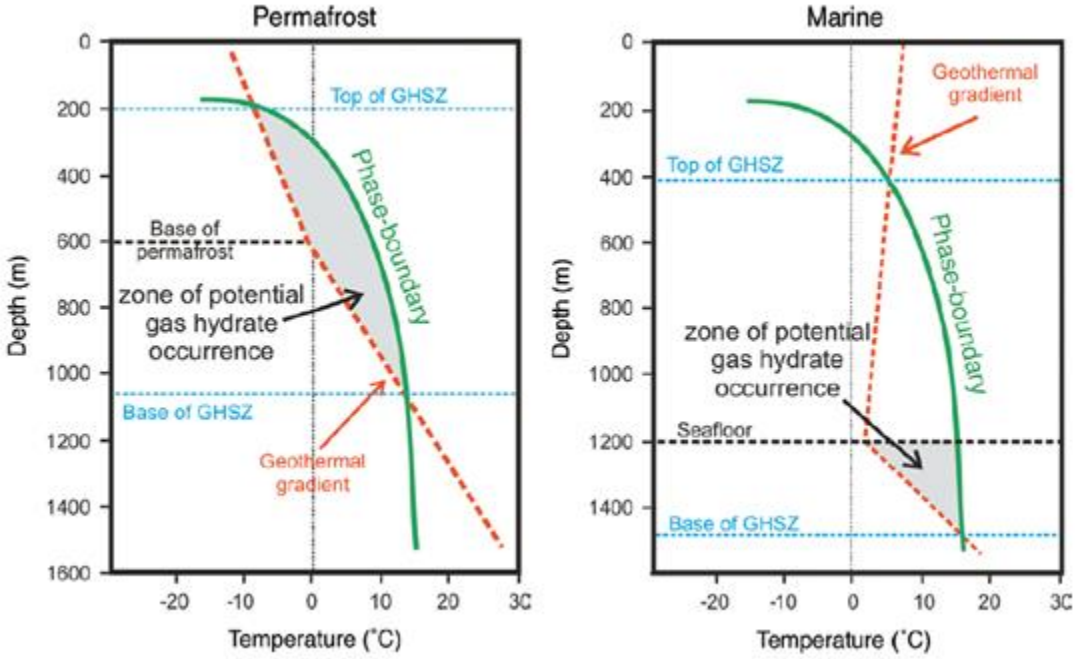

Figure 1.2: Phase diagrams of gas hydrates conditions in permafrost (left) and marine settings (right) (Riedel et al., 2010). The green line represents the phase boundary of gas hydrates and the dashed red line represents the geothermal gradient of the regions. The area enclosed within these two curves represents the zone of gas hydrates occurrence known as the gas-hydrates stability zone (GHSZ). In the permafrost region gas hydrates occur in the depth range typically 200-1050m with temperature ranging between -5^{o}C and 15^{o}C. In the marine region gas hydrates occur in the depth range is typically 400-1500m with temperature ranging between 2^{o}C and 16^{o}C.

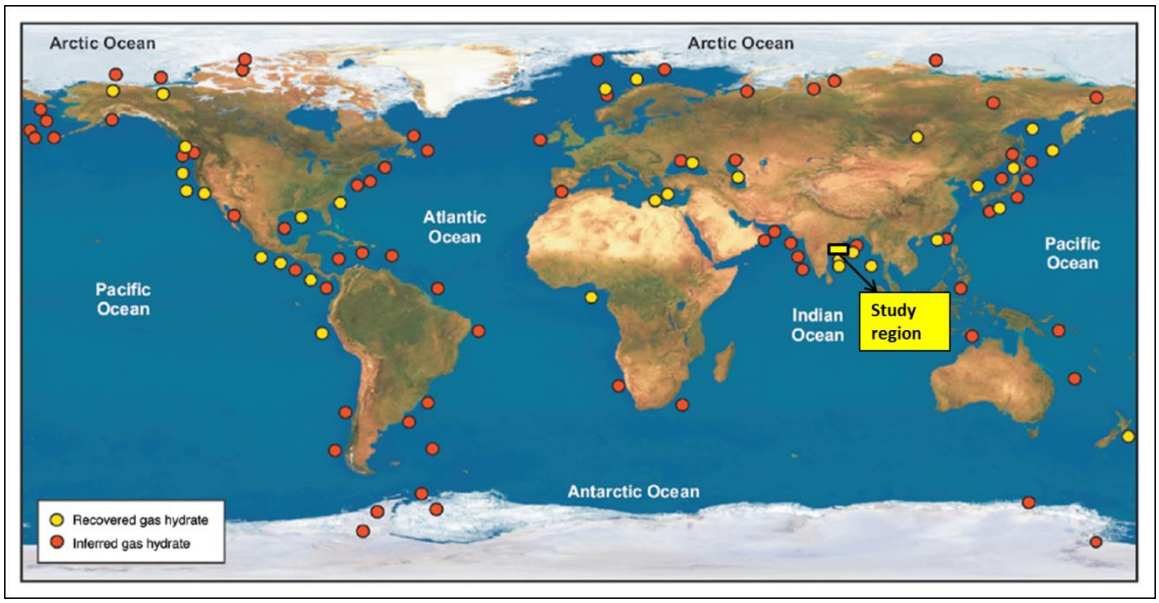

Figure 1.3: Worldwide occurrences of identified gas hydrates (Riedel et al., 2010). The yellow dots show the places with recovered gas hydrates and the red dots the places with inferred gas hydrates. Occurrences are mostly along continental margins, but include a few in permafrost regions (e.g. Canada). The present study region (Krishna-Godavari) basin, highlighted in yellow box, is located on the western offshore of India.

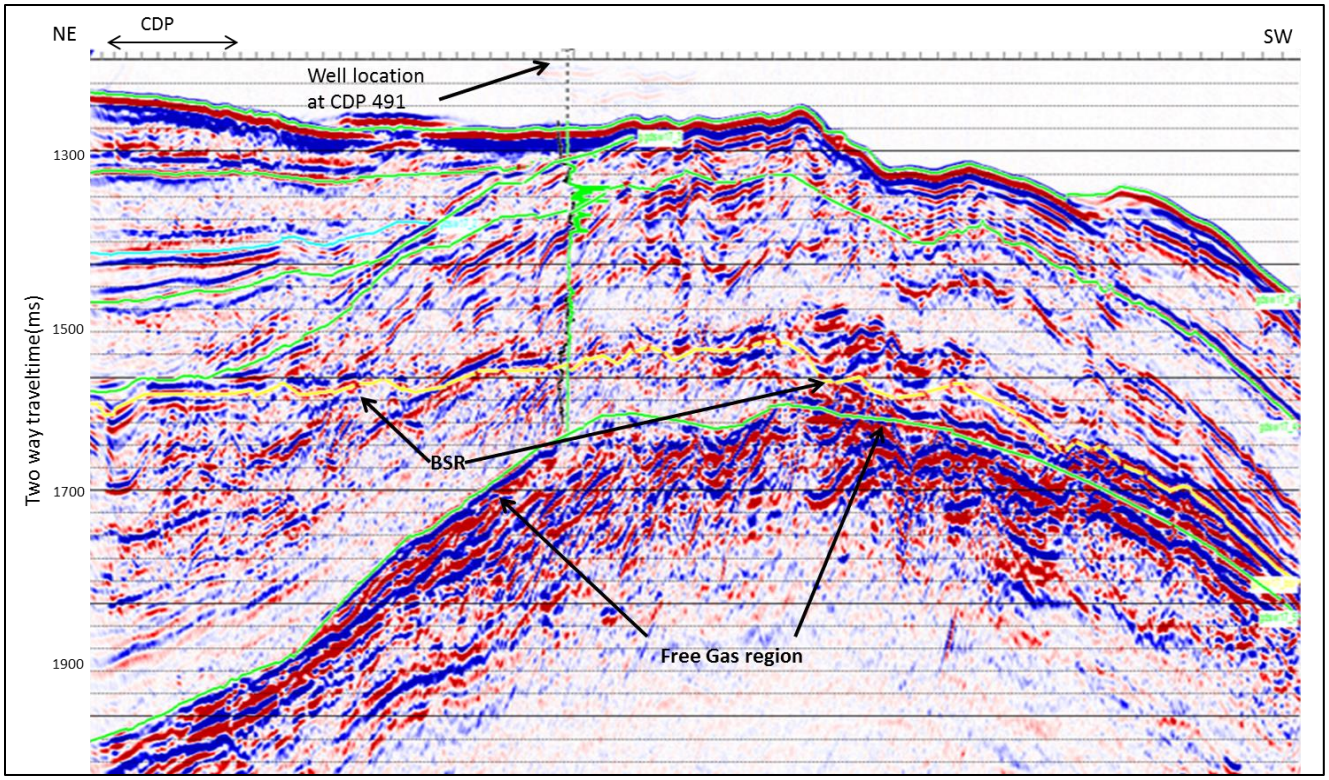

Figure 1.4: Seismic section of the study region (Krishna-Godavari basin) with well location on the seismic section at CDP 490. The interpreted seismic horizons are shown in the colour green. The BSR is represented by the yellow horizon interpreted on the seismic section. It is prominent towards the NE section where it can be seen cutting across the geological layers. Another factor that is indicative of the BSR is the opposite polarity of the reflector to that of the seafloor. The bright amplitude feature beneath the BSR is attributed to free gas in the region (Collett et. al, 2009).

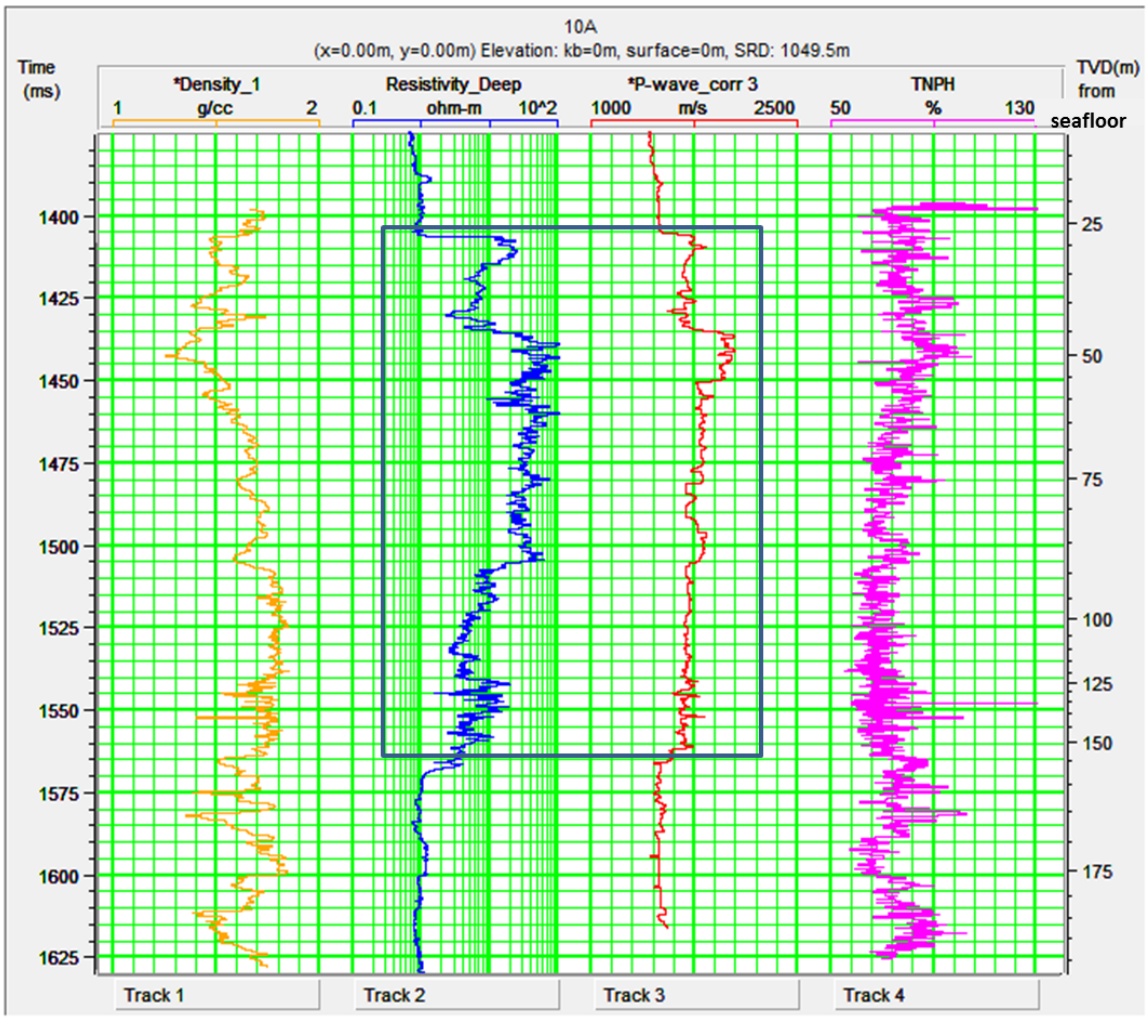

Figure 1.5: Borehole well logs displayed in two way reflection traveltime from the sea floor. The Gas hydrates stability zone (GHSZ) is indicated in the box. A major change in resistivity is observed at around 1405 ms, which is the top of gas hydrate bearing sediments, and 1570 ms, which is the base of the GHSZ. In the same zone, considerable change in P-wave velocity is also observed. Density and neutron porosity do not show any significant change but are displayed here because they are used in the study.

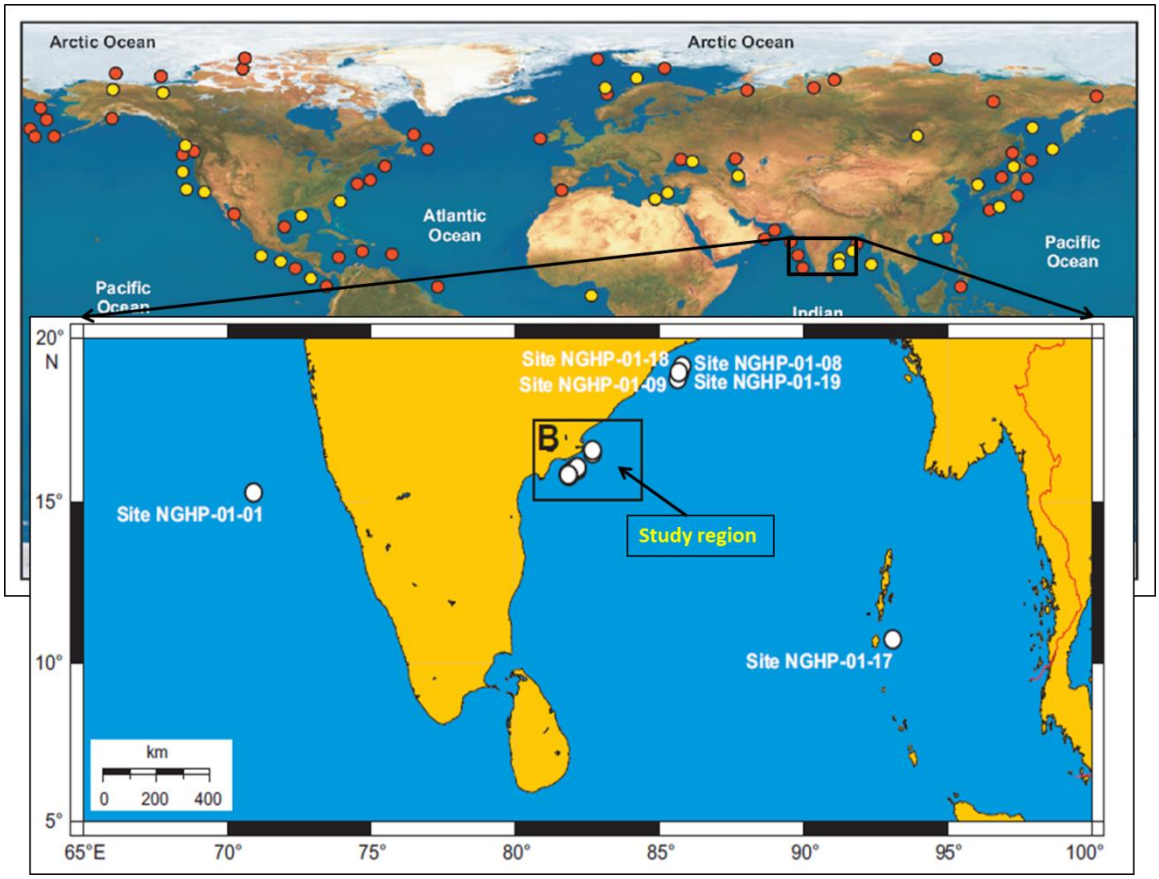

Figure 1.6: Map showing the region of study in the Krishna-Godavari basin in the Eastern offshore, India. The white dots are the drilling locations during the NGHP Expedition 01. The arrow marked black box denotes the study region.

1.7 REFERENCES

Allen, D., D. Bergt, D. Best, B. Clark, I. Falconer, J.-M.Hache, C. Kienitz, M. Lesage, J. Rasmus, C. Roulet, and P. Wraight, 1989, Logging while drilling: Oilfield Review, 1, 4–17.

Archie, G. E. (1942), The electrical resistivity log as an aid in determining some reservoir characteristics, J. Pet. Technol., 1, 55–62.

Biksham, G., and Subrahmanyam, V., 1988. Sediment transport of the Godavari River Basin and its controlling factors, J. Hydrol., 101, 275-290.

Bily, C., and J. W. L. Dick, 1974, Natural occurring gas hydrates in the Mackenzie Delta, Northwest Territories: Bulletin of Canadian Petroleum Geology, 22, 340–352.

Boswell, R., T. S. Collett, D. McConnell, M. Frye, B. Shedd, S. Mrozewski, G. Guerin, A. Cook, P. Godfriaux, R.Dufrene, R. Roy, and E. Jones, 2009, Joint Industry Project Leg II discovers rich gas-hydrate accumulations in sand reservoirs in the Gulf of Mexico: DOE–National Energy Technology Laboratory (NETL) Fire in the Ice: Methane Hydrate Newsletter, summer 2009, 1–5, http://www.netl.doe.gov/technologies/oil-gas/publications/Hydrates/Newsletter/HMNewsSummer09.pdf

Chand, Shyam, Tim A. Minshull, Jeff A. Priest, Angus I. Best, Christopher R. I. Clayton, and William F. Waite. 2006. “An Effective Medium Inversion Algorithm for Gas Hydrate Quantification and Its Application to Laboratory and Borehole Measurements of Gas Hydrate-bearing Sediments.” Geophysical Journal International 166 (2): 543–552. doi:10.1111/j.1365-246X.2006.03038.x.

Collett, T. S., 1993, Natural gas hydrates of the Prudhoe Bay and Kuparuk River area, North Slope, Alaska: AAPG Bulletin, 77, 793–812.

Collett, T. S., and J. Ladd, 2000, Detection of gas hydrate with downhole logs and assessment of gas hydrate concentrations (saturations) and gas volumes on the Blake Ridge with electrical resistivity log data: Proceedings of the ODP Scientific Results, 164, 179–191.

Collett, T. S., M. Riedel, J. Cochran, R. Boswell, J. Presley, P. Kumar, A. V. Sathe, A. Sethi, M. Lall, V. Sibal, and the NGHP Expedition 01 Scientists, 2008, Indian National Gas Hydrate Program (NGHP) Expedition 01, Initial Report: Directorate General of Hydrocarbons, Ministry of Petroleum and Natural Gas, India.

Dallimore, S. R., T. Uchida, and T. S. Collett, 1999, Scientific results from JAPEX/JNOC/GSC Mallik 2L-38 gas hydrate research well, Mackenzie Delta, Northwest Territories, Canada: Geological Survey of Canada Bulletin 544.

Dallimore, S. R., and T. S. Collett, 2005, Scientific results from the Mallik 2002 Gas Hydrate Production Research Well Program, Mackenzie Delta, Northwest Territories, Canada: Geological Survey of Canada Bulletin 585, CD ROM.

Ecker, C., Dvorkin, J., and Nur, A., 2000 Estimating the amount of gas hydrate and free gas from marine seismic data: Geophysics, 65, 565–573.

Fujii, T., T. Namikawa, T. Okui, M. Kawasaki, K. Ochiai, M. Nakamizu, and Y. Tsuji, 2008, Resource assessment of methane hydrate in the Eastern Nankai Trough, Japan: OTC Paper 19310.

Giavarini, Carlo;Hester, Keith. Gas Hydrates. Dordrecht: Springer-Verlag London Limited, 2011.

Goldberg, D., 1997, The role of downhole measurements in marine geology and geophysics: Review of Geophysics, 35, no. 3, 315–342.

Guerin, G. D., and D. Goldberg, 2002, Sonic waveform attenuation in gas hydrate-bearing sediments from the Mallik 2L-38 research well, Mackenzie Delta, Canada: Journal of Geophysical Research, 107, B5, 2088, doi: 10.1029/2001JB000556.

Helgerud, M., J. Dvorkin, A. Nur, A. Sakai, and T. Collett, 1999, Elastic-wave velocity in marine sediments with gas hydrates: Effective medium modeling: Geophysical Research Letters, 26, 2021–2024.

Helgerud, M. B., W. F. Waite, S. H. Kirby, and A. Nur (2009), Elastic wave speeds and moduli in polycrystalline ice Ih, sI methane hydrate, and sII methane-ethane hydrate, J. Geophys. Res., 114, B02212, doi:10.1029/2008JB006132.

Klauda, J., and S. Sandler, 2005, Global distribution of methane hydrate in ocean sediment: Energy & Fuels, 19, 469.

Korenaga, J., Holbrook, W. S., Singh, S. C., and Minshull, T. A., 1997, Natural gas hydrates on the southeast US margin: Constraints from full waveform and travel time inversion of wide-angle seismic data: J. Geophys. Res., 102, 15345–15365.

Kvenvolden, K. A., 1993, Gas hydrates—Geological perspective and global change: Rev. Geophys., 31, 173–187.

Lee, M. W., Hutchinson, D. R., Dillon, W. P., Miller, J. J., Agena, W. F., and Swift, A. B., 1993, Method of estimating the amount of in-situ gas hydrates in deep marine sediments: Marine Petr. Geol., 10, 493–506.

Lee, M. W., Hutchinson, D. R., Collett, T. S., and Dillon, W. P., 1996, Seismic velocities for hydrate-bearing sediments using weighted equation: J. Geophys. Res., 101, 20347–20358.

Lee, M.W., Collett, T.S., 2009. Gas hydrate saturations estimated from fractured reservoir at Site NGHP-01-10, Krishna-Godavari Basin, India. J. Geophys. Res. 114, B07102.

Lu, S., and G. McMechan. 2002. Estimation of Gas Hydrate and Free Gas Saturation, Concentration, and Distribution from Seismic Data. GEOPHYSICS 67 (2) (March 1): 582–593.

Makogon YF (1997) Hydrates of hydrocarbons.PennWell Books, Tulsa.

Markl, R. G., G. M. Bryan, and J. I. Ewing, 1970, Structure of the Blake Bahama Outer Ridge: Journal of Geophysical Research, 75, 4539–4555.

Mathews, M. A., 1986, Logging characteristics of methane hydrate: The Log Analyst, 27, 26–63.

Milkov, A., 2004, Global estimates of hydrate-bound gas in marine sediments: How much is really out there? Earth Science Reviews, 66, no. 3, 183.

Murray, D. R., M. Fukuhara, O. Osawa, T. Endo, R. L.Kleinberg, B. K. Sinha, and T. Namikawa, 2006, Saturation, acoustic properties, growth habit, and state of stress of a gas hydrate reservoir from well logs: Petrophysics, 47, 129–137.

Neave, K. G., A. S. Judge, J. A. Hunter, and H. A. MacAulay, 1978, Offshore permafrost distribution in the Beaufort Sea as determined from temperature and seismic observations: Geological Survey of Canada, Current Research, Part C, paper 78-1C, 13–78

Ojha, M. and K. Sain, 2008. Appraisal of gas hydrates/free-gas from V_P/V_S ratio in the Makran accretionary prism, Mar. & Petrol. Geol., 25, 637-644.

Ojha, M., Sain, and T. A. Minshull. 2010. Assessment of Gas-hydrate Saturations in the MakranAccretionary Prism Using the Offset Dependence of Seismic Amplitudes: Geophysics 75 (2): C1–C6.

Park, K.P., Bahk, J.J., Y. Kwon, Kim,G.Y., Riedel,M., Holland,M., Schultheiss, P., Rose, K., and the UBGH-1 Scientific Party, 2008, Korean national program expedition confirms rich gas hydrate deposits in the Ulleung Basin, East Sea: DOE-

National Energy Technology Laboratory (NETL), Fire in the Ice: Methane Hydrate Newsletter, 6–9

Paull, C. K., R. Matsumoto, and P. Wallace, 1996, Proceedings of the Ocean Drilling Program, Initial Reports 164: Ocean Drilling Program

Ramana, M., T. Ramprasad, A. Paropkari, D. Borole, B. RamalingeswaraRao, S. Karisiddaiah, M. Desa, et al. 2009. "Multidisciplinary Investigations Exploring Indicators of Gas Hydrate Occurrence in the Krishna–Godavari Basin Offshore, East Coast of India." Geo-Marine Letters 29 (1): 25–38. doi:10.1007/s00367-008-0121-7.

Riedel, Michael, Eleanor C. Willoughby, and Satinder Chopra, eds. Geophysical Characterization of Gas Hydrates. 8801 South Yale Suite 500 Tulsa OK 74137 USA: SEG, 2010.

Riedel, M., T. S. Collett, M. J. Malone, and the Expedition 311 Scientists, 2006, Proceedings of the IODP, 311 (Integrated Ocean Drilling Program Management International, Inc.), doi: 10.2204/iodp.proc.311.2006.

Sain K., and H. K. Gupta, 2008. Gas hydrates: Indian scenario, Jour. of Geol. Soc. of India, 72, 299-311.

Sain K., and H. K. Gupta, 2012. Gas hydrates in India: Potential and Development, Gondwana Research, 22, 645-657.

Sastri, V.V., Venkatachala, B.S., and Narayanan, V., 1981. The evolution of the east coast of India, Paleogeogr.,Paleoclim., Paleoeco., 36, 23-54.

Shipley, T. H., M. H. Houston, R. T. Buffler, F. J. Shaub, K. J. McMillen, J. W. Ladd, and J. L. Worzel, 1979, Seismic evidence for widespread possible gas hydrate horizons on continental slopes and rises: AAPG Bulletin, 63, 2204–2213.

Stoll, R. D., J. I. Ewing, and G. M. Bryan, 1971, Anomalous wave velocities in sediments containing gas hydrates: Journal of Geophysical Research, 76, 2090–2094.

Tréhu, A. M., G. Bohrmann, F. R. Rack, and E. Torres, 2003, Drilling gas hydrates on Hydrate Ridge, Cascadia continental margin: Proceedings of the Ocean Drilling Program, Initial Reports, 204.

Waite, W., M. B. Helgerud, A. Nur, J. C. Pinksto, L. Stern, and S. Kirby, 2000, Laboratory measurements of compressional and shear wave speeds through methane hydrate, in G. D. Holder and P. R. Bishnoi, eds., Gas hydrates: Challenges for the future: Annals of the New York Academy of Science, 912, 1003–1010.

Westbrook, G. K., D. B. Carson, and R. J. Musgrave, 1994, Proceedings of the Ocean Drilling Program, Initial Reports, 146, Part 1.

Wood, W. T., Stoffa, P. L., and Shipley, T. H, 1994, Quantitative detection of methane hydrate through high-resolution seismic velocity analysis: J. Geophys. Res., 99, 9681–9695.

Yang, S., H. Zhang, N. Wu, X. Su, P. Schultheiss, M. Holland, G. Zhang, J. Liang, J. Lu, and K. Rose, 2008, High concentration hydrate in disseminated forms obtained in Shenhu area, North Slope of South China Sea: Proceedings of the 6th International Conference on Gas Hydrates (ICGH 2008), Vancouver, British Columbia, Canada.

Yuan, T., Hyndman, R. D., Spence, G. D., and Desmons, B., 1996, Seismic velocity increase and deep-sea gas hydrate concentration above a bottom-simulating reflector on the northern Cascadia continental slope: J. Geophys. Res., 101, 13655–13671.

Chapter 2: Poststack inversion

In this chapter I describe the application of poststack inversion to the seismic reflection data from the 2D seismic line from the region of study for the determination of P-impedance. Hampson-Russell®, a commercially available software package that includes various analysis and applications, is used for inversion. First I briefly describe the principles of poststack inversion following which I review the inversion methodology and the various steps involved in preparing the surface seismic reflection data for poststack inversion. Then I present the P-impedance results obtained from poststack inversion of the seismic data and discuss some of its implications. Finally I present a sensitivity analysis of the P-impedance result to the initial model to judge how well the geologic features can be resolved based on the low-frequency content of the initial P-impedance model.

2.1 INTRODUCTION

Impedance inversion is the process of obtaining P-impedance (ρV_P) from seismic data (Lindseth, 1979; Oldenburg et al., 1983). The goal of this chapter is to invert reflection amplitudes strengths in poststack reflection seismic data to obtain profiles of P-impedance values. Poststack seismic data is an approximation of the reflection response of the layered earth to a perpendicularly incident plane wave (Sen, 2006, p. 35). For a particular layer in the earth, its acoustic impedance is defined as the product of its P-wave velocity (Vp) and density. If the earth is approximated by a series of reflectors between layers of varying impedance, then the seismogram is equivalent to the filtered response of the earth to the impulse generated from the seismic source. It is approximated by a convolutional process between the earth acting as a filter and the wavelet that is generated from the seismic source (Russell, 1988) and can be represented as:

$$s(t) = \omega(t) * r(t), \qquad 2.1$$

where the symbol '*' denotes convolution, t is time, $\omega(t)$ is the wavelet in the time domain, $r(t)$ is the reflectivity time series computed from the contrasts in P-impedance and $s(t)$ is the seismogram in the time domain, which is a band limited time series. Generally the field seismic record includes noise. The approximate representation of an actual field seismic record is:

$$s(t) = \omega(t) * r(t) + n(t) \quad , \qquad 2.2$$

where $n(t)$ is noise in the time domain Russell (1988). The presence of noise makes impedance inversion a more difficult problem as noise cannot be modeled, thus making the inverse problem non-linear (Sen, 2006, p. 74). Hence, one of the chief prerequisites of data quality prior to post-stack inversion is the reduction of noise. This is achieved by processing the seismic data. The processed (nearly noise-free) data are approximately represented as in Equation 2.1. Reflectivity 'r' is related to impedance 'I 'by the following relation:

$$r(t) = [I(t) - I(t-1)]/[I(t) + I(t-1)] \ . \qquad 2.3$$

Equation 2.3 is valid only when the P-wave is vertically incident on the reflector. However, the field seismic data are recorded at multiple angles of incidence. Because the formulation of the poststack inversion problem is based on the premise that the incident wave is perpendicular to the reflector (Sen, 2006), this assumption is approximated through the stacking of normal moveout (NMO) corrected, common depth point (CDP) gathers.

Processing of the seismic data included static shifts, editing of noisy traces, geometry application, muting, deconvolution, common depth point (CDP) sorting, velocity analysis, stacking and time migration to enhance the signal-to-noise (S/N) ratio. The 120-channel shot gathers were further processed as follows: The raw data were

frequency filtered with a broad band pass filter (4-12-400-420 Hz). The pre-processing consists of amplitude recovery at 6 db/s; and the spherical divergence corrections. Predictive deconvolution (80 ms operator length) designed to increase the resolution and the dip move-out (DMO), to compensate for the dipping reflections, were applied to the pre-stack data prior to velocity analysis. Interactive velocity analysis was carried out at every 62.5 m (every 10^{th} CDP) with zero stretch mute. The applied seismic data processing flow is shown in Table 1 for the high signal-to-noise ratio. The normal move out (NMO) velocity analysis can generally not resolve the gas layer beneath the BSR due to the vertical resolution limits at the depth of BSR. However, the velocity increase with depth is reduced within the depth interval underneath the BSR. The predictive deconvolution suppresses reverberations and compresses the wavelet. Due to limited streamer length, we have applied 0% NMO stretch mute. The deconvolution is especially helpful to assure a clear image because the move out correction has a similar effect to a low-pass filter by stretching the traces in a time varying manner. Frequency distortion especially increases at large offsets and shallow times. For interpretation of the seismic sections, a standard NMO mute of 0% is applied to ensure high vertical resolution. An automatic gain control (AGC) is applied before the full common mid-point (CMP) stack in order to amplify the BSR and deeper structures in the migrated section. Subsequently data were stacked and Kirchoff migrated.

The processing of seismic data is done on a scientific workstation using Paradigm Focus®, a commercially available industrial seismic data processing software. As a result of the above processing steps, the seismic data can be treated as a series of reflectors in their true physical locations with the seismic waves perpendicularly incident and reflected back from them. Once this has been achieved the resultant data can be used for post-stack inversion to obtain P-impedance values.

2.2 PRINCIPLES OF IMPEDANCE INVERSION

Impedance inversion using poststack seismic data has been extensively used in geophysics (for example, Lindseth, 1979; Oldenburg et al, 1983; Cooke and Schneider, 1983). It is a favored method of inversion because of its straightforward assumptions and robustness (Russell and Hampson, 1991). Poststack inversion tackles three types of problems (Sen, 2006, p.69-70): 1) Wavelet estimation to extract a source wavelet when the reflection coefficient series ('r' in Equation 2.3) is known, 2) Reflection coefficient given the seismic wavelet ('ω' in Equation 2.1) is assumed to be known and, 3) Inverting for impedance contrasts with the desired wavelet. Poststack inversion methods are classifiable in three broad categories (Russell and Hampson, 1991): 1) The recursive inversion method, in which if the impedance of a starting layer is known (or assumed), for example the seafloor in case of marine seismic data. Then the impedance of other layers can be solved recursively using a modified version of Equation 2.1(for example, Cooke and Schneider, 1983), 2) Sparse spike inversion is an inversion method in which a sparse set of reflection coefficients are extracted from the seismic data, which is constrained with a model based on geological constraints (for example, Torres-Verdín et al., 1999). 3) Model-based methods, which rely on perturbing an initial impedance model based on geological constraints, until the synthetic seismic data matches the observed seismic data within an acceptable error tolerance. In the present studies, I use STRATA® module available in Hampson-Russell®, an industrial inversion software for the inversion of seismic data. It involves inversion for impedance given that the seismic wavelet is known. It is a model-based method (the third discussed above) of poststack inversion. Because the exact code for poststack inversion in STRATA® is proprietary and undisclosed, I present here a brief outline of the inversion methodology based on the background information which is available from the Hampson-Russell Assistant®.

Model-based methods of inversion are preferred because they overcome the challenges of removing the source wavelet completely, removal of all noise, accounting for spherical divergence and transmission losses and including out-of-plane reflections, which are encountered in other inversion methods (Sen, 2006, p. 74). A basic flow of model-based inversion is shown in Figure 2.1 which is adopted form the user's manual. Based on the guide for STRATA® the model-based poststack inversion of Hampson-Russell® can be summarized in the following steps:

1. Extraction of wavelet,
2. Identification of main reflectors from seismic data,
3. Initial P-impedance model,
4. Inversion analysis at well location, and
5. Model-based inversion for the complete 2D poststack seismic section.

Each of these steps are discussed in details in the following sections

2.2.1 Impedance inversion framework

In this section I present the theory of impedance inversion, which forms the basis of inversion in STRATA®. The following description of impedance inversion is compiled from the STRATA theory by Hampson and Galbriath (1999).

Considering the case of an N layered 1-D representation of earth at a well location, the two way traveltime through the i^{th} layer is given by:

$$t(i) = 2d(i)/v(i) \quad , \qquad 2.4$$

where, $d(i)$and $v(i)$ are, respectively, the thickness and P-wave propagation velocity of the i^{th} layer and i varies from 1 to N. From poststack seismic data the $t(i)'s$ can be readily determined, allowing for a more suitable parameter for time given as:

$$\tau(i) = \sum_{j=1}^{i-1} t(j)\,, i = 1, N \quad , \tag{2.5}$$

which represents the two way traveltime between the top of the i^{th} layer and the receiver on the earth's surface. Following this the seismic trace as convolution operation between reflectivity and wavelet can be represented by the equation:

$$T(i) = \sum_{j=1}^{N} r(j)\omega(i - \tau(j) + 1) + n(i) \quad , \tag{2.6}$$

Where $T(i)$ is the amplitude of the seismic trace, i representing the sample point at which the amplitude is measure, $r(j)$ is the reflectivity at the j^{th} sample point, ω is the wavelet, and $n(i)$ represents the noise present in the data. Equation 2.6 is similar to Equation 2.2; the difference in their form arises from the fact that Equation 2.2 represents the seismic trace as a function of time while Equation 2.6 represents the seismic trace in discrete samples of time and the convolution operation is expressed as an integration. Equation 2.6 represents a set of N equations for an N-layered 1-D earth model. In the general case where N is less than the number of total time samples in a seismic trace, the determination of impedance is an over-determined problem.

Given an initial impedance value, the modeled synthetic seismic trace M is given as:

$$M(i) = \sum_{j=1}^{N} r_0(j)\omega(i - \tau(j) + 1) \quad . \tag{2.7}$$

The error (e) between the true seismic trace (T) and the synthetic trace (M) defined in Equation 2.7, is given as:

$$e(i) = T(i) - M(i) \quad . \tag{2.8}$$

The goal of inversion is to obtain the correct model parameter values (impedance), this is achieved by minimizing an objective function, which is a function of the error between the observed seismic trace ($\boldsymbol{T}$) and the modeled synthetic seismic trace ($\boldsymbol{M}$). In the present case of an over-determined problem, a least-squares norm is used to minimize the objective function. If the objective function is represented as

$$\boldsymbol{J} = e^T e = \ (\boldsymbol{T} - \boldsymbol{Wr})^{\boldsymbol{T}}(\boldsymbol{T} - \boldsymbol{Wr}) \ , \tag{2.9}$$

where J is the objective function, $\boldsymbol{T}$ is the vector comprised of all the samples of the actual seismic trace represented as:

$$\boldsymbol{T} = \begin{bmatrix} T(1) \\ T(2) \\ \vdots \\ T(NSAMP) \end{bmatrix} \tag{2.10}$$

$\boldsymbol{r}$ is the vector with all the reflection coefficients at all sample points represented as:

$$\boldsymbol{r} = \begin{bmatrix} r(1) \\ r(2) \\ \vdots \\ r(NSAMP) \end{bmatrix} \tag{2.11}$$

and $\boldsymbol{W}$ is a matrix of with N (number of layers) columns and NSAMP (number of time samples in a seismic trace) rows, whose elements are the seismic wavelet, shifted by the two way times ($\tau(i)$) to the top of each layer, represented as:

$$\boldsymbol{W} = \begin{bmatrix} \omega(1) & 0 & \dots \\ \omega(2) & 0 & \dots \\ \vdots & \omega(1) & \\ \omega(m) & \omega(2) & \\ 0 & \vdots & \ddots \\ 0 & \omega(m) & \\ \vdots & \vdots & \\ 0 & 0 & \end{bmatrix} \qquad 2.12$$

then minimizing the objective function $\boldsymbol{J}$(defined in Equation 2.9 is) with respect to the reflectivity ($\boldsymbol{r}$), produces a set of normal equations, solving which, the value of reflectivity is obtained as follows:

$$r = (\boldsymbol{W^T W} + \boldsymbol{\lambda I})^{-1} \boldsymbol{W^T T} \quad . \qquad 2.13$$

Here $\boldsymbol{\lambda}$ is a prewhitening factor added to stabilize the inversion procedure, $\boldsymbol{I}$ is the identity matrix, $\boldsymbol{W}$ is defined in Equation 2.12. $\boldsymbol{T}$ is defined in Equation 2.10. Once $\boldsymbol{r}$ is obtained, impedance is calculated as a convolution sum by

$$I(j) = I(1) \prod_{j=2}^{i} [(1 + r(j))/(1 - r(j))] \ . \qquad 2.14$$

However, Equation 2.14 suffers from the drawbacks that the impedance is very sensitive to noise in reflectivity, and it also suffers from non-uniqueness, which means that many combinations of reflectivity produce the same seismic trace. To address this non-

uniqueness problem, model-based inversion is used. In a model-based inversion, constraints are used to limit the model space in the vicinity of the initial guess model. The objective function for model based impedance inversion can be represented as:

$$\boldsymbol{J} = \boldsymbol{w_1} \times (\boldsymbol{T} - \boldsymbol{W} * \boldsymbol{r}) + \boldsymbol{w_2} \times (\boldsymbol{M} - \boldsymbol{H} * \boldsymbol{r}), \tag{2.15}$$

where, $\boldsymbol{T}$ is defined by the Equation 2.10, W is defined by the Equation 2.12, r is the final reflectivity, $\boldsymbol{M}$ is the vector consisting of initial impedance guess represented as:

$$\boldsymbol{M} = \begin{bmatrix} M(1) \\ M(2) \\ \vdots \\ M(NSAMP) \end{bmatrix}, \tag{2.16}$$

$\boldsymbol{H}$ is an operator that convolves the wavelet ($\boldsymbol{W}$) with the final reflectivity ($\boldsymbol{r}$) to produce the final impedance and '*' denotes the convolution operation. $w_1$and w_2 are the weights assigned to errors in the seismic trace prediction and the impedance prediction, respectively. The weights have values between 0 and 1. Assigning a weight 1 implies that there is complete confidence in that data against which that weight is assigned. A weight 0 implies the opposite thing. Two methods are available to apply constraints known as the stochastic inversion and constrained inversion.

Stochastic inversion applies 'soft' constraints, i.e. the initial guess impedance model is considered as external information and it is added to the seismic data, each with some weighing factor. If initial impedance is$I_0(i), i = 1, NSAMP$,
and logarithm of impedance (L) is given as

$$L(i) = \log[I_0(i)], \tag{2.17}$$

then using logarithmic expansion of the terms $\log(1 + r(j))$ and$\log(1 - r(j))$, Equation 2.14 can be rewritten as

$$I_0(i) \cong L(1) + \sum_{j=2}^{i} 2[r(j) + (r^3(j)/3) + (r^5(j)/5) + \ldots]. \quad 2.18$$

Considering that the reflection coefficients are not too large (less than 0.2) the higher order terms become negligibly small compared to the lower order terms in the above series. For example when $r = 0.2$, it can be observed that in the cubic term the first significant digit occurs in the third decimal place. Following this, Equation 2.18 can be written as

$$L(i) - L(1) \cong \sum_{j=2}^{i} 2r(j) \quad . \quad 2.19$$

Then the new objective function can be written as

$$J = e^T e = (\boldsymbol{L} - \boldsymbol{Hr})^{\boldsymbol{T}}(\boldsymbol{L} - \boldsymbol{Hr}), \quad 2.20$$

where $\boldsymbol{r}$ is defined in Equation 2.11, $\boldsymbol{L}$ is defined as:

$$\boldsymbol{L} = \begin{bmatrix} L(1) - L(1) \\ L(2) - L(1) \\ \vdots \\ L(NSAMP) - L(1) \end{bmatrix} \quad , \quad 2.21$$

and $\boldsymbol{H}$ is defined as:

$$\boldsymbol{H} = \begin{bmatrix} 2 & 0 & 0 & \dots & 0 \\ 2 & 2 & 0 & \dots & 0 \\ \vdots & \vdots & 2 & \dots & \vdots \\ 2 & 2 & \vdots & \dots & 0 \\ 2 & 2 & 2 & 2 & 2 \end{bmatrix} \quad . \tag{2.22}$$

Then reflectivity, $\boldsymbol{r}$ is solved for using the set of normal equations

$$\boldsymbol{H^T H r = H^T L} \; . \tag{2.23}$$

The combined least squares objective function, with the model included as a constraint is given as

$$\boldsymbol{J = w_1 (L - Hr)^T (L - Hr) + (1 - w_1)(T - Wr)^T (T - Wr).} \tag{2.24}$$

To optimize for the different units for the two parts of the objective function the following normalizing parameters, called mean squared signal levels, are used:

$$TMS = \frac{1}{NSAMP} \sum_i T(i)^2 \quad , \tag{2.25}$$

$$LMS = \frac{1}{NSAMP} \sum_i L(i)^2 \quad . \tag{2.26}$$

The objective function in Equation 2.24 becomes

$$\boldsymbol{J = \frac{w_1 (L - Hr)^T (L - Hr)}{LMS} + \frac{(1 - w_1)(T - Wr)^T (T - Wr)}{TMS}} \quad . \tag{2.27}$$

The solution thus obtained also contains the low frequency component, which was not present in the solution obtained by minimizing the objective function in Equation 2.9. The low frequency component in the optimized solution comes from the first term in the right hand side of Equation 2.27, which is derived from the constraining low frequency impedance model.

Constrained inversion, in contrast to stochastic inversion, sets 'hard' constraints. More specifically, it sets the limits on the deviation of model parameters using the initial guess. The logarithm of impedance can then be approximated as

$$L(i) \cong L(0) + \sum_{j=2}^{i} 2r(j) \quad . \tag{2.28}$$

In the case of an m layered earth the following vector $\boldsymbol{L}$ is defined as

$$\boldsymbol{L} = \begin{bmatrix} L(0) \\ L(1) \\ \vdots \\ L(m) \end{bmatrix} \quad . \tag{2.29}$$

The reflection coefficients for m layers are

$$r(1) = (1/2)[L(1) - L(0)]$$
$$r(2) = (1/2)[L(2) - L(0)]$$
$$\vdots$$
$$r(m) = (1/2)[L(m) - L(m-1)] \quad .$$

The set of equations above can be written in the matrix form as

$$\boldsymbol{r} = \boldsymbol{DL}, \tag{2.30}$$

where $\boldsymbol{D} = \frac{1}{2}\begin{bmatrix} -1 & 1 & 0 & 0 & 0 & \dots \\ 0 & -1 & 1 & 0 & 0 & \dots \\ 0 & 0 & -1 & 1 & 0 & \dots \\ \vdots & \vdots & \vdots & \vdots & \vdots & \ddots \end{bmatrix}$. 2.31

Combining Equation 2.30 with the original optimization function in Equation 2.9 the new objective function using the hard constraint is

$$\boldsymbol{J} = (\boldsymbol{T} - \boldsymbol{WDL})^{\boldsymbol{T}}(\boldsymbol{T} - \boldsymbol{WDL}) \ . \tag{2.32}$$

Then $\boldsymbol{L}$, defined in Equation 2.29 is solved as

$$\boldsymbol{L} = (\boldsymbol{D^T W^T W D})^{-1}\boldsymbol{D^T W^T T} \ . \tag{2.33}$$

In Hampson-Russell®, Equation 2.33 is solved by the conjugate-gradient method. The conjugate gradient method is based on using the gradient of the error (objective) function with respect to model parameters to find the minimum of the error (objective) function. The next step in obtaining realistic estimates of impedance from seismic data is the scaling of the inversion result.

2.2.2 Scaling of inversion results

Scaling of the impedance inversion result obtained from solving for Equation 2.33 is important because the inverted impedances and the seismic traces have different scaling factors. This is solved by dividing the both the sides of the equation

$$\boldsymbol{W^T W r = W^T T} \quad , \tag{2.34}$$

which is the simplest solution of the minimization of the objective function presented in Equation 2.9. The scaling factor for the left hand side of the Equation 2.34 is

$$avgModelAmp = \sqrt{\left({}^{1}/_{N}\right)\sum_{i}(W^T W r)_i^2} \quad , \tag{2.35}$$

$$avgTraceSize = \sqrt{\left({}^{1}/_{N}\right)\sum_{i}(W^T T)_i^2} \quad . \tag{2.36}$$

Then the Equation 2.34 after scaling appears as:

$$\frac{\boldsymbol{W^T W r}}{avgModelAmp} = \frac{\boldsymbol{W^T T}}{avgTraceSize} \quad . \tag{2.37}$$

Thus the unequal scaling of seismic traces and the inverted impedance results are removed in STRATA®.

2.2.3 Wavelet extraction

There are three commonly applied methods of wavelets extraction: deterministic, statistical and well log based. Hampson-Russell® offers all the three capabilities of obtaining a wavelet. Strata® uses a combination of statistical and well log based wavelet extraction, where the statistical method that uses seismic data for wavelet extraction is followed by the well log based wavelet extraction. I describe in the following paragraphs the theories behind these two methods of wavelet extraction.

The statistical method of determining a wavelet in STRATA® uses seismic data. In this method a window of seismic data is chosen in the zone of interest for the purpose of extraction of the wavelet. In the present case I chose a window within the gas hydrate stability zone as it is the chief zone of interest of my study. The amplitude series extracted from this window is auto-correlated. The amplitude spectrum of the wavelet is then calculated by taking the square of the auto-correlation of the amplitudes within the selected data window. Because the autocorrelation does not provide the phase of the wavelet, an estimated phase is added to the amplitude spectrum of the wavelet. In the present case, a zero phase wavelet was chosen. The inverse Fourier transform of the result obtained describes the wavelet. All the wavelets obtained by this procedure applied to different traces are then summed up to obtain a single composite wavelet.

The well log based method of determining a wavelet in STRATA® uses sonic and density well log data. The wavelet extraction from well logs is an inversion problem in itself. Given a wavelet $w(t)$ and the reflectivity series $r(t)$ a synthetic seismic trace can be represented as,

$$w(t) * r(t) = s(t) , \qquad 2.38$$

where '*' represents the convolution operator. Sonic and density well logs are used to calculate the reflectivity series and matched with the seismic trace in the analysis window. Equation 2.38 can also be interpreted as least-squares shaping problem, where the goal here is to predict the wavelet using a least squares prediction filter. A least squares prediction filter works on the principle that given an output, which is the seismic trace in this case, a filter is to be designed such that a desired output, in this case the wavelet, can be obtained. In matrix notation the Equation 2.38 can be represented as

$$\boldsymbol{WR} = \boldsymbol{S}, \qquad 2.39$$

where $\boldsymbol{W}$ is matrix representation of the wavelet, $\boldsymbol{R}$ is matrix representation of the reflectivity series and $\boldsymbol{S}$ is the matrix representation of the synthetic seismic trace. If the actual seismic trace is represented as $\boldsymbol{T}$ then the error between the observed seismic trace ($\boldsymbol{T}$) and the synthetic seismic trace ($\boldsymbol{S}$) is represented as

$$\boldsymbol{E} = \boldsymbol{T} - \boldsymbol{S}, \tag{2.40}$$

and the sum of the squared errors is

$$\boldsymbol{E}^2 = (\boldsymbol{T} - \boldsymbol{S})(\boldsymbol{T} - \boldsymbol{S})^T, \tag{2.41}$$

Minimizing the squares of the error gives a set of normal equations that can be solved to obtain the wavelet. Because the number of samples in the wavelet is less than the number of samples in the seismic analysis window, this is an over determined inversion problem that is solved using least squares. The amplitude envelop of the wavelet is calculated using the Hilbert transform of the seismic trace. Because the well log data also contain higher frequencies above the seismic frequency range, a suitable frequency filter is applied to limit the wavelet frequency within the seismic frequency range.

2.2.4 Initial model building

As discussed in Section 2.2.1, the inversion algorithm in STRATA® requires an initial 1D P-impedance model. The initial model is a low-frequency impedance model obtained from the low-frequency component of the sonic and density well logs. To define the impedances in thick layers, the model information is derived by picking major reflectors on poststack seismic section. These horizons act as the guiding points for the

impedance values at all trace locations using interpolation well location. Through interpolation, a low-frequency blocky impedance model is built. Because the goal is to extract the low frequency data from well log data, a low pass frequency filter of less than 10 Hz is applied to obtain the low frequency data to be combined with the seismic frequency range data. Typically 0-10 Hz is the frequency range chosen because seismic data is not effectively recorded in this frequency range and because most of the data in this frequency range is lost during processing.

2.2.5 Impedance inversion steps

The procedure for impedance inversion in STRATA® is shown in a flowchart in Figure 2.1. Prior to inversion, the seismic data are processed for attenuation of noise and to obtain a stacked migrated seismic section. This prepares the seismic data for poststack impedance inversion. The next step is horizon picking to identify the main reflectors present in the 2D seismic section. The picked horizons are used in building the initial (starting) impedance model, including the low frequency trend, and well log correlation. After the horizons are picked, a wavelet is extracted statistically for correlating the picked events on the seismic and well logs at the location of the wells. Correlation between the events picked on seismic data and the corresponding events on the synthetic is maximized by adjusting the well logs to attain the best possible match with the composite traces obtained from the actual seismic trace at the well location. Following this, correlation is done again by using a wavelet extracted from well logs to maximize the match between the synthetic and the observed seismic trace at the well location. Because the inversion is model based, an initial low frequency impedance model is built with well-logs and seismic data, with the picked seismic horizons acting as constraints for inversion.

First, inversion analysis is carried out at the well location to calculate the scaling parameters for seismic amplitudes. Inversion at the well location is iterated multiple times. Inversion at the well location also gives the scaling parameters which are later used in inversion of other traces for scaling the inverted parameters. After obtaining a satisfactory match between the observed seismic trace and the synthetic seismic trace calculated from the inverted parameters from inversion analysis at the well location, model based impedance inversion is done for all the traces in the seismic section. The scaling parameters obtained during inversion at the well location are used for scaling the inverted parameters at other trace locations. Inversion is iterated multiple times to obtain a better approximation of the model parameters. The end product of the poststack impedance inversion is pseudo P-impedance log at every trace location along the seismic profile.

2.3 IMPEDANCE INVERSION OF REAL SEISMIC DATA AND SENSITIVITY ANALYSIS

2.3.1 Impedance inversion of real seismic data: Results

The steps for preparing seismic data for poststack inversion is discussed in Section 2.1, where a series of seismic data processing steps applied to the seismic data from the region of study is outlined. Figure 2.2 shows the time-migrated seismic data after processing. Six principal reflectors, including the BSR, are identified and picked on the migrated seismic section. These interpreted horizons are used for building the initial P-impedance model. The three primary horizons of interest are the seafloor, the bottom simulating reflector (BSR) and the top of the free gas zone under the BSR. Other major reflectors are picked based on their amplitude strength. The interpreted BSR horizon is included in the discussion illustrating the location of the BSR, and it is not used in

building the initial guess impedance model. This is because the BSR does not represent a geological layer but appears on a seismic section because it is a physical phase boundary. Therefore, the interpolation of the impedance values will lead to erratic values if the BSR is considered as a geological reflector. The northeast (NE) end of the seismic profile shown in Figure 2.2 is closer to the shore, and the southwest (SW) end is down-dip the shore. The well used for present study is located closest to CDP number 490 on the seismic line shown in the Figure 2.2. It is located at a distance of 30m away from the seismic line. It can be observed from the seismic section that the strengths of the reflectors' amplitudes reduces from NE to SW. However, some of the sedimentary beds become clearer in the SW section of the line. The BSR is represented as the yellow horizon interpreted in the seismic section in Figure 2.2. The BSR has higher amplitude at the NE end of the seismic section, where it can be seen cutting across the dipping geological layers. The visibility of the BSR becomes poor in the vicinity of the well but becomes visible toward the SW end of the seismic section. The bright amplitude event beneath the BSR is attributed to the free gas region (Collett et. al., 2009).

Correlation of well logs provides the link between interpreted seismic horizons to the synthetic seismic traces calculated from the well logs. Composite seismic traces, the average of the seismic traces around the well log location are used for correlation with the synthetic seismograms. Figure 2.3 and Figure 2.4 show the wavelets extracted statistically from seismic data and wavelet extracted from well log respectively. It is observed that the statistically extracted wavelet from seismic data is a zero phase wavelet. The zero phase wavelet is user supplied information and hence expected. The wavelet extracted from the well is rotated relative to a zero phase wavelet. Figure 2.5 shows a suite of well logs used for generating synthetic seismograms, the correlation between the synthetic seismic traces (blue traces in Figure 2.5) and the composite seismic traces (red

traces in Figure 2.5). It can be visually observed from Figure 2.5 that there is a reliable match between the synthetic and the actual seismic trace at the well location. The match between the synthetic seismic data and observed seismic data is measured by a factor known as the correlation factor. The correlation factor between the synthetic generated using the wavelet extracted from seismic and the actual composite seismic trace is 0.4. When the wavelet extracted from well is used correlation factor between the synthetic and the composite seismic trace increases to 0.6. Thus the correlation of the interpreted horizons between the synthetic and the actual seismic trace is better for the wavelet extracted from well. Hence it can be inferred that the minimum phase wavelet extracted from the well log is an improved approximation for the actual seismic wavelet.

Following the well log correlation a low frequency starting initial P-impedance is built as shown in Figure 2.6. The model building is guided by the interpreted geological horizons, which act as guide for interpolation between well logs. The interpolated values of P-impedance thus obtained are filtered by applying a high cut frequency filter of 10-15 Hz. The next step following initial model building is inverting the seismic data for impedance. This is carried out in two stages, first inverting for the seismic trace at the well location, followed by inverting for all the seismic traces. The impedance inversion result at the well location is shown in Figure 2.7. The result shows that there is a correlation factor of 0.994 between the original and the predicted impedance values and the error in fraction is 0.109. The scaling parameters used in the inversion of all the other traces are obtained from the inversion done of the seismic trace at the well location. These scaling parameters are used to limit the reflection coefficient values within the physically feasible range.

Figure 2.8 shows the P-impedance obtained from the inversion of the complete seismic section. Impedance inversion is done only up to the top of the free gas layer

because the well logs do not extend beyond that depth. Hence, the impedance values of the inverted section of two way traveltime greater than the two way traveltime of the well bottom are not to be taken into consideration. The impedance ranges from 2200 g/cm^3× m/s to 3200 g/cm^3 × m/s. The cooler colors are the regions of high impedance, which is as expected, because the presence of gas hydrates increases the P-impedance of the host rocks. The impedance in the GHSZ varies between 2800-3100 g/cm^3 × m/s. The high resistivity zone of 1400ms-1600ms, as seen in Figure 2.5 falls within the region of high impedance. This also coincides with the high P-wave velocity. Impedance of the sediments with the gas-hydrates increases when the gas-hydrates constitute the load bearing part of the host rock. In the present scenario because the P-impedance of the sediments increases, it can be interpreted that gas-hydrates make up a part of the matrix. The impedance values right beneath the gas hydrates zone show low impedance, as expected from the impedance of free gas zone. P-impedance is the output of the impedance inversion, provides a means to investigate the spatial extent of gas-hydrates. The P-impedance values obtained from inversion are the direct indicative of the extent of the gas-hydrates in the region. With the assumption that the increase in P-impedance occurs only due to the replacement of water from pore spaces by gas-hydrates, P-impedance can be used to calculate the saturation of gas-hydrates. However, as there are no known direct relationship between gas-hydrates saturation and P-impedance, I use an alternative method for estimation of gas-hydrates saturation. The alternative method to estimate gas-hydrates saturation uses seismic attributes calculated from P-impedance to predict petrophysical properties, which are related to gas-hydrates saturation through the Archie's equation. The method is presented and discussed in details in Chapter 4.

2.3.2 Sensitivity of impedance inversion to the starting model

Model based impedance inversion in STRATA® requires a 2D initial guess impedance model. The theory of initial model building is discussed in Section 2.2.4. In this section I present a study to investigate the effect of frequency range of the starting initial model on the final impedance result. The impedance inversion process as discussed in Section 2.2.5 is repeated each time with a different initial impedance model. The initial models are generated over various ranges of seismic frequencies. Figure 2.9 shows a low frequency initial P-impedance model derived from the stacked CDP section, but limited to the frequency range of 10-15 Hz, the P-impedance inversion result obtained with this initial P-impedance model as the initial impedance model. Figure 2.10 shows a high frequency initial P-impedance model derived from the stacked CDP section, but limited to the frequency range of 35-40 Hz and the P-impedance inversion result obtained with this initial impedance model as the initial impedance model. Comparing the P-impedance inversion results from Figure 2.9 and Figure 2.10 it is observed that the inverted P-impedance result is almost the same in both the cases of low frequency and high frequency initial impedance models. Hence, I conclude that even a low frequency initial P-impedance model can be used to obtain almost similar features as that can be obtained from a high frequency initial P-impedance model. This becomes important considering the fact that in field seismic data the higher frequencies are lost and the data is predominantly low frequency. It has been demonstrated here that even a low frequency initial impedance model gives a good enough result. Therefore, the lack of high frequencies in the initial guess is not a major problem in impedance inversion.

2.4 SUMMARY AND DISCUSSIONS

Inversion of poststack time migrated seismic data is applied to obtain P-impedance along the complete 2D seismic profile 6.25 km long. Both surface seismic and

borehole well log data are used for the inversion process. A model based inversion algorithm in STRATA® uses an extracted wavelet and initial P-impedance model built based on structural interpretation of reflection profile. The wavelet is obtained using two approaches: statistical and well log. The initial model is built with the aid of the interpreted seismic horizons. A very high correlation (70.9) between the inverted impedance and actual impedance at the well location indicates that the results obtained at the well location are good. Using the scaling parameters obtained from inversion analysis at the well location, inversion of the complete seismic section is done. An observation on the P-impedance inversion of the seismic section reveals high impedance in the gas hydrates zone and low impedance in the free gas zone underneath it. This is in agreement with the general assumption that impedance increases in the presence of gas hydrates because of the higher P-wave velocity of the gas hydrates and decreases in the presence of gas. Thus impedance helped me to estimate the lateral extent of the gas hydrates zone.

I carried out analysis to study the sensitivity of the starting model to the final impedance model. My analysis reveals that use of high frequency starting models introduces bias in the final impedance model. A low-frequency starting model (10-15Hz) is adequate for obtaining a realistic solution in that it provides missing low frequency information and high frequency content of the inverted model is extracted entirely from the seismic data.

Processing steps	Parameters
Butterworth band-pass filter	4-12-400-420 Hz
Normal Move out (NMO) velocity analysis at Every	10 CDP (~62.5 m)
True amplitude recovery (TAR):	Spherical divergence correction $g(t) = 1/(time^* vel^{**}2)$
Predictive deconvolution Operator length:	80 ms
NMO correction	NMO stretch mute values: zero
Automatic gain control (AGC)	Time window: 500 ms
CMP stack	Mean
Kirchhoff time migration	Max. dip: 180^{o}, max. frequency: 50Hz, smoothed velocity field

Table 2.1: Flow of processing applied to seismic data to obtain a stacked migrated section. This processed data is used for post-stack migration. The processed common mid-point (CMP) seismic gathers are used for pre-stack seismic inversion.

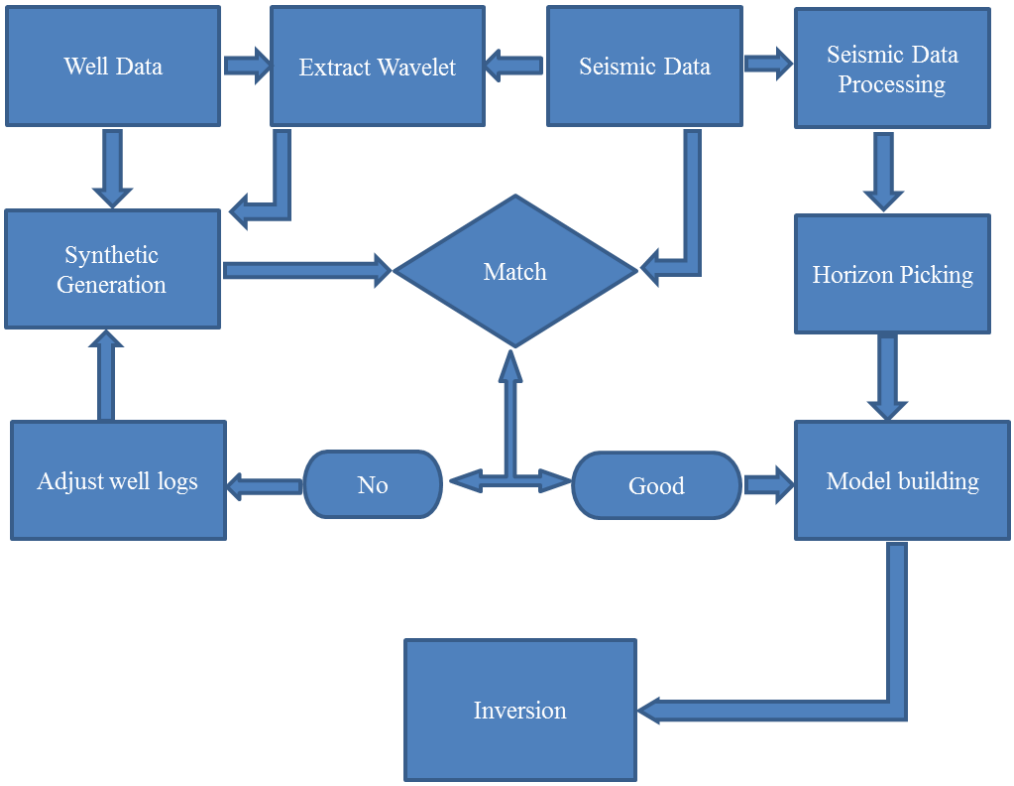

Figure 2.1: Flowchart of model based post-stack impedance inversion. Both processed seismic and well log data at a point within the seismic depth are required. The flowchart can be broadly divided into the following activities namely wavelet extraction, synthetic generation and well log correlation with seismic, initial impedance model building, inversion of all seismic traces. The wavelet is first generated statistically using seismic data and then using well log data. The wavelet along with well log data is used for generating synthetic seismic data to be compared with the real seismic data. The mismatch between the observed and synthetic seismic data is checked using an objective function that gives a measure of the accuracy of the predicted model parameters. The scaling parameters for the whole seismic section inversion are obtained from inversion at the well location. Interpreted seismic data with seismic horizons is used for building an initial impedance model. The initial impedance models along with the previously obtained scaling parameters are used for inversion for all seismic traces. The inversion process is iterated multiple times to obtain a better approximation of model parameters.

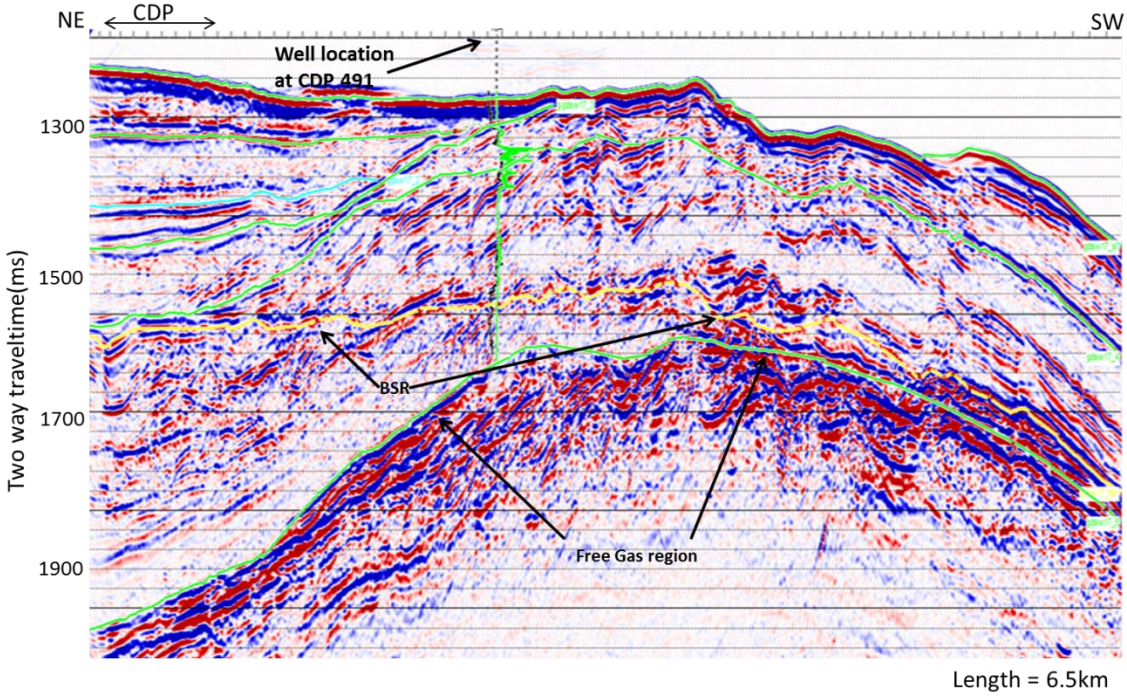

Figure 2.2: Seismic section with the picked horizon on display. Sonic log (green) and resistivity log (black) at CDP 490 are displayed on the seismic section to emphasize the GHSZ. Six horizons used for initial model building are shown in green and blue colour. The yellow dashed line is the BSR. The bright reflecting zone beneath the BSR is the free gas region. Resistivity log (green) is also shown.

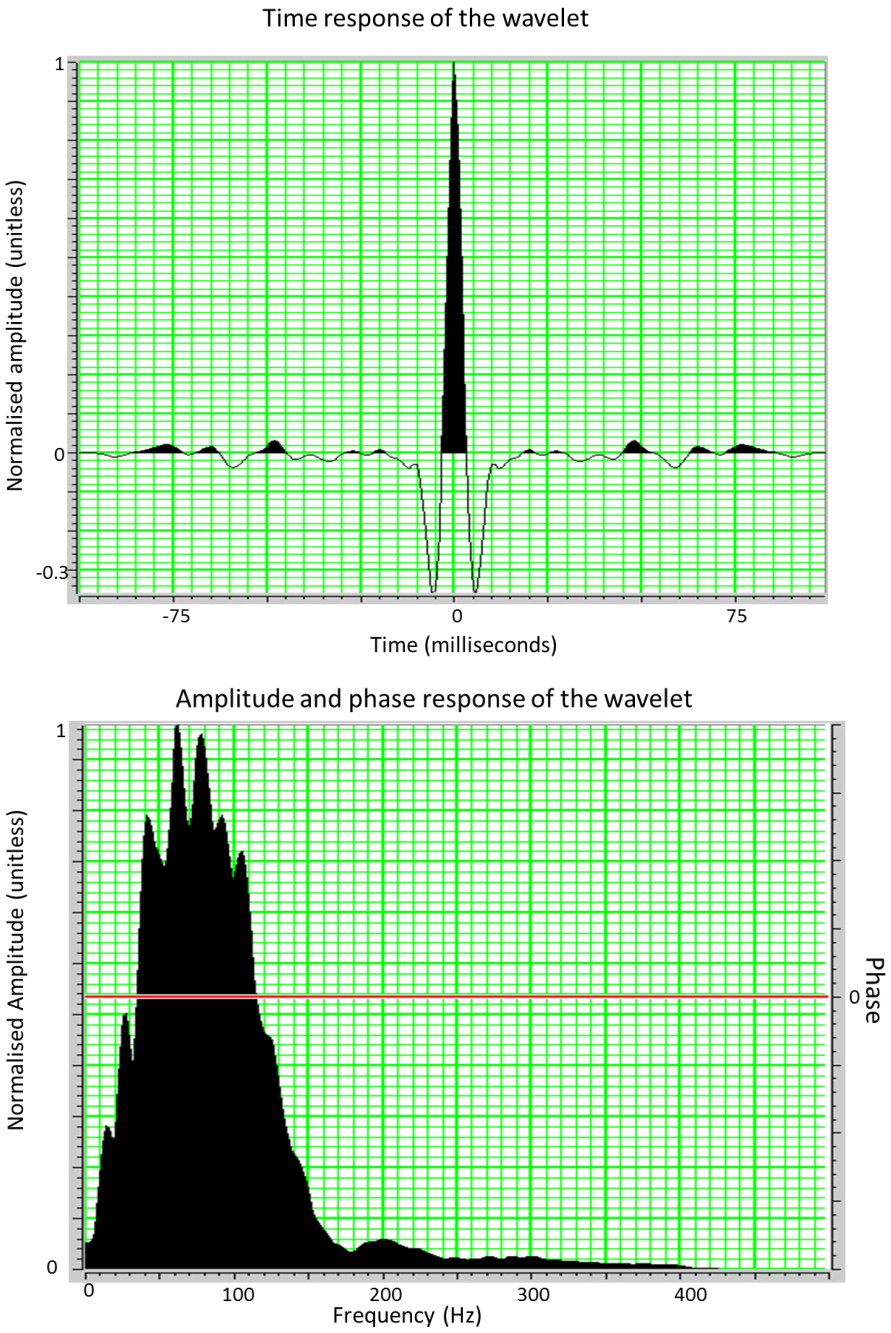

Figure 2.3: Statistically extracted wavelet from seismic data. Its time response shown in the upper panel shows that it is a zero phase wavelet. Its amplitude spectrum is shown in the lower panel. The peak frequency is 50 Hz.

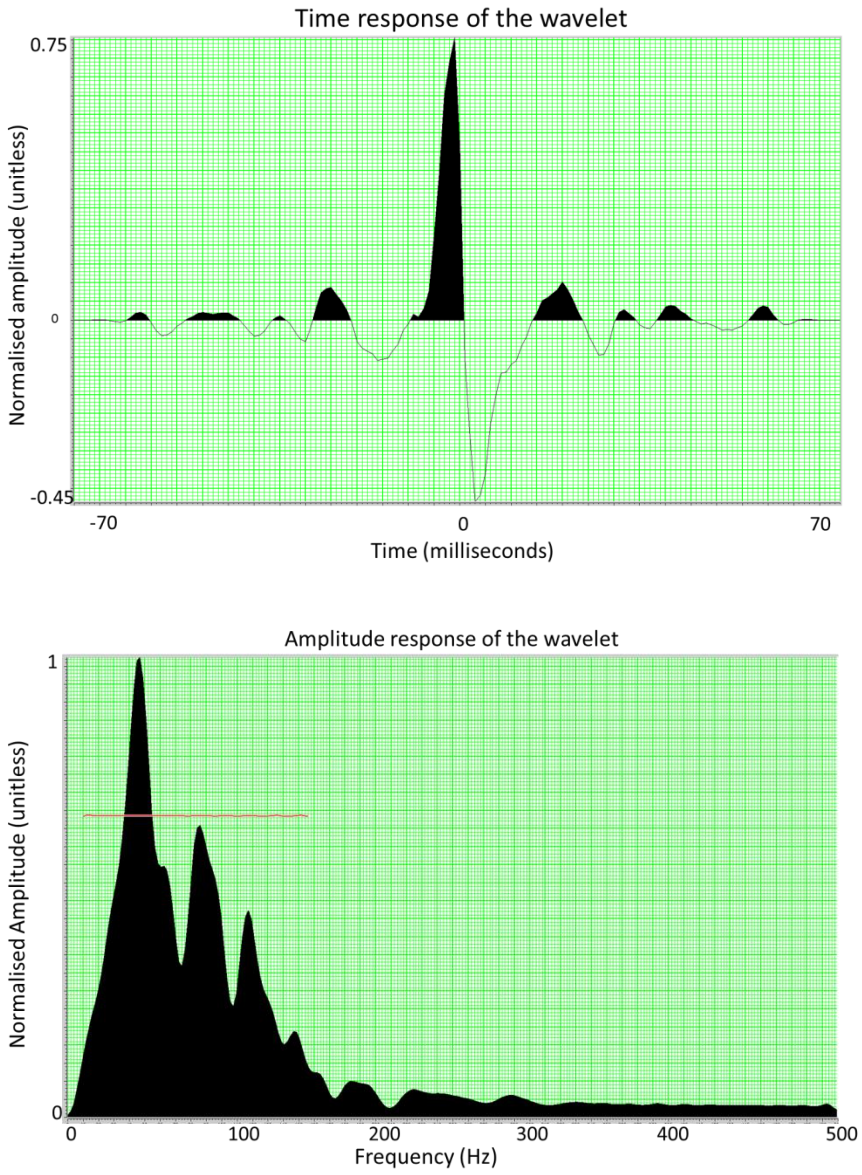

Figure 2.4: Wavelet extracted from well log and seismic data. The time response of the wavelet shown in the upper panel shows that it is a rotated wavelet relative to a zero phase wavelet. Its amplitude spectrum is shown in the lower panel. Its peak frequency is 50 Hz.

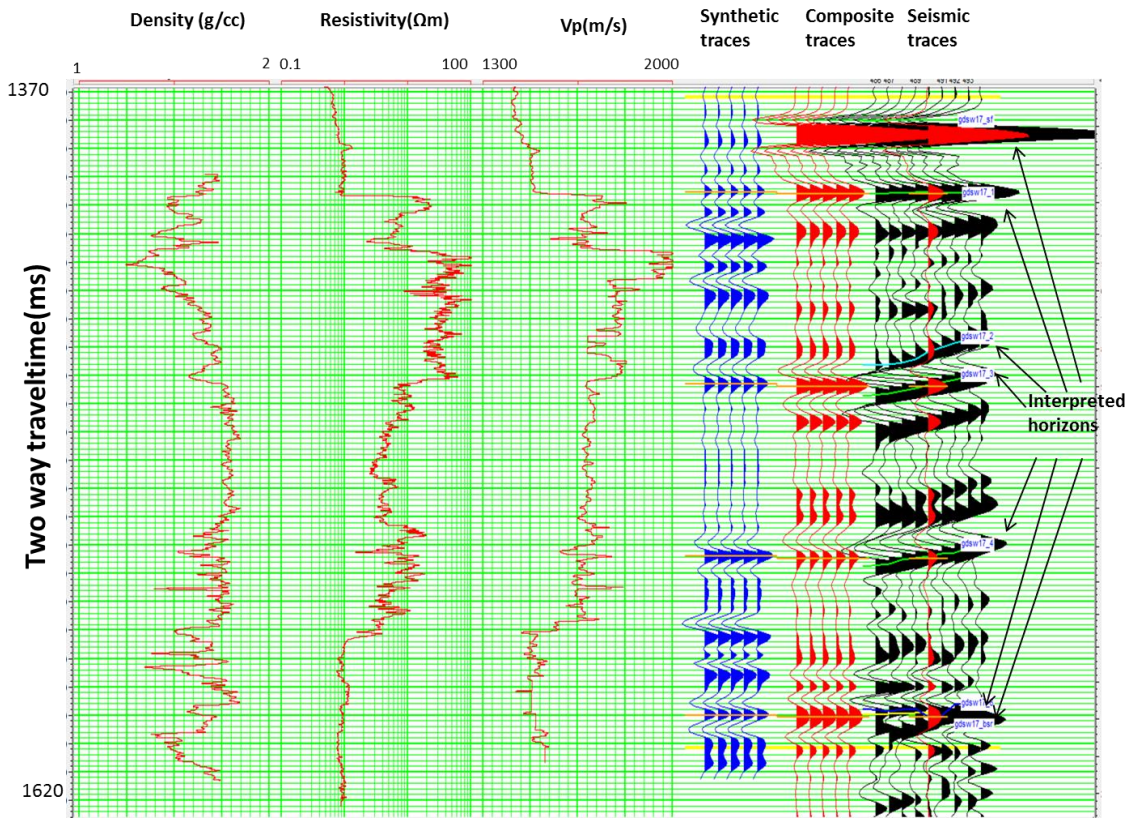

Figure 2.5: Correlation of well log data with seismic data. The logs, in order from left to right, are density, deep resistivity and P-wave velocity. The panel on the right shows from left to right, the synthetic traces (blue) generated using the well extracted wavelet, the composite traces (red) at the well location and the seismic traces (black) in well vicinity with the red being the trace at the well log location. Note the good correlation between the synthetic and composite traces, a correlation factor of 0.6 between the synthetic and composite traces is obtained.

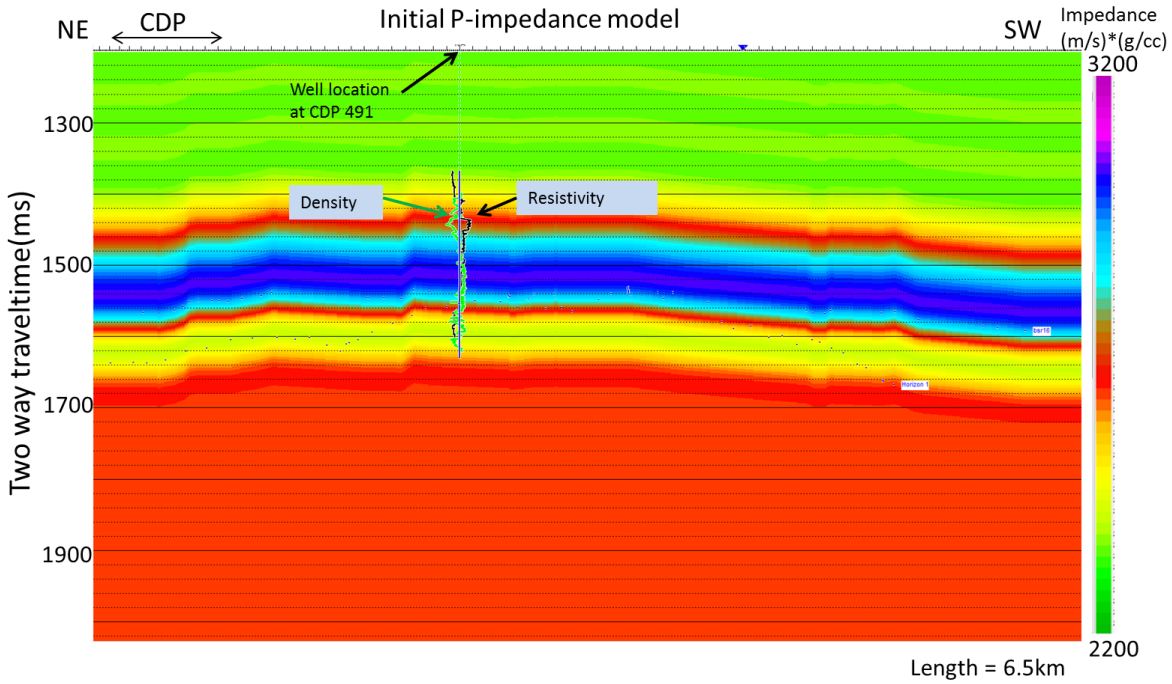

Figure 2.6: Low frequency initial P-impedance model with the color bar guide of impedance values ranging from 2200 to 3200 g/cm^3× m/s. The green end of the color bar indicates low impedance and the purple end high impedance. The resistivity log (black) and the density log (black) are also shown.

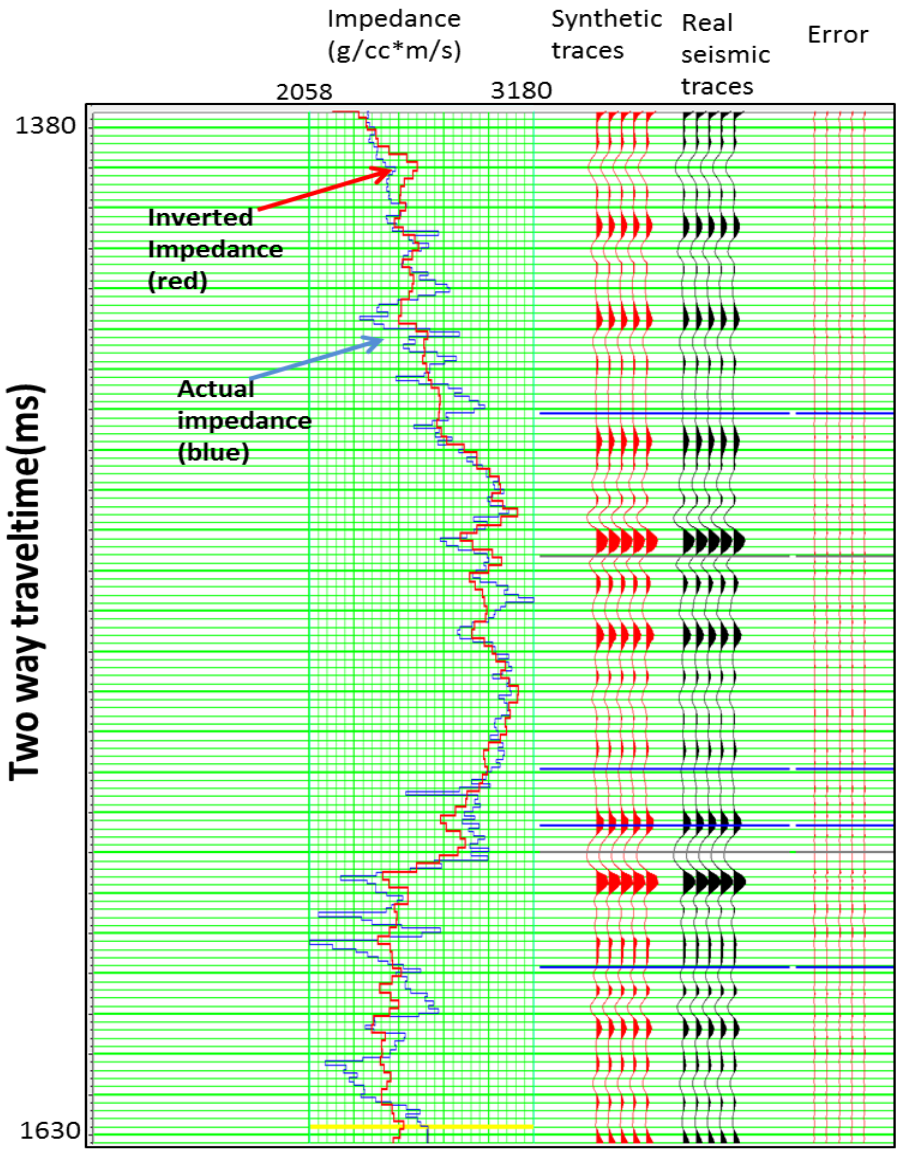

Figure 2.7: Inversion analysis at the well location. The curves in the left panel display the inverted impedance (red) and impedance from well log (blue). The center panel shows the synthetic (red) and the seismic (black). The right panel shows the error of the predicted impedance.

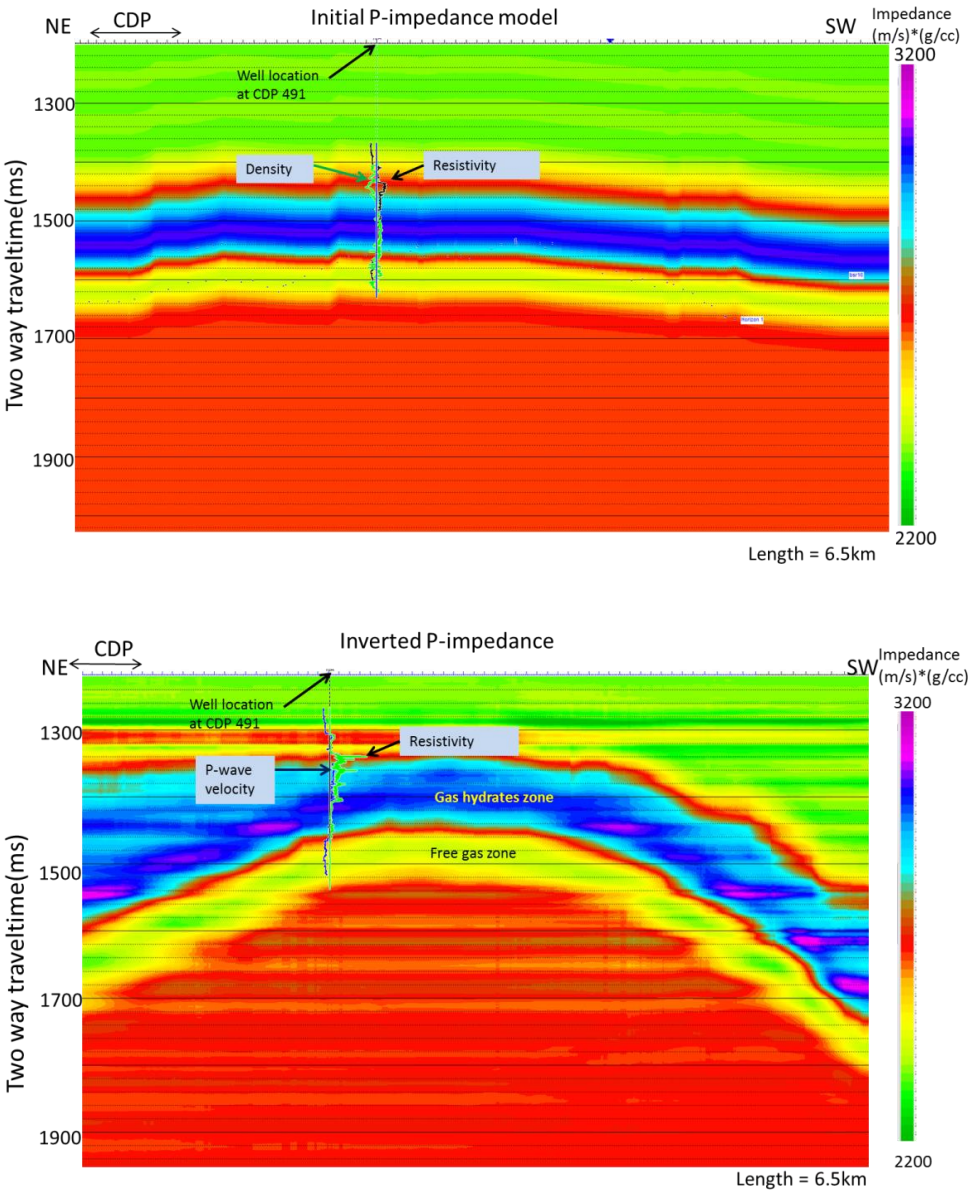

Figure 2.8: The low frequency initial impedance model (above) and the inverted P-impedance (below) of the whole seismic section obtained after 50 iterations. The color bar indicating the impedance values ranging from 2200 to 3200 g/cm^3× m/s is shown to the right of the image. The impedance in the GHSZ varies between 2800-3100 g/cm^3 × m/s .The lower end of the color bar (green) indicates low impedance and the upper end (purple) indicated high impedance. The resistivity log (black) and the density log (black) are also shown. The cooler colors indicate the gas-hydrates zone. Also note the low impedance values (yellow) in the free gas region.

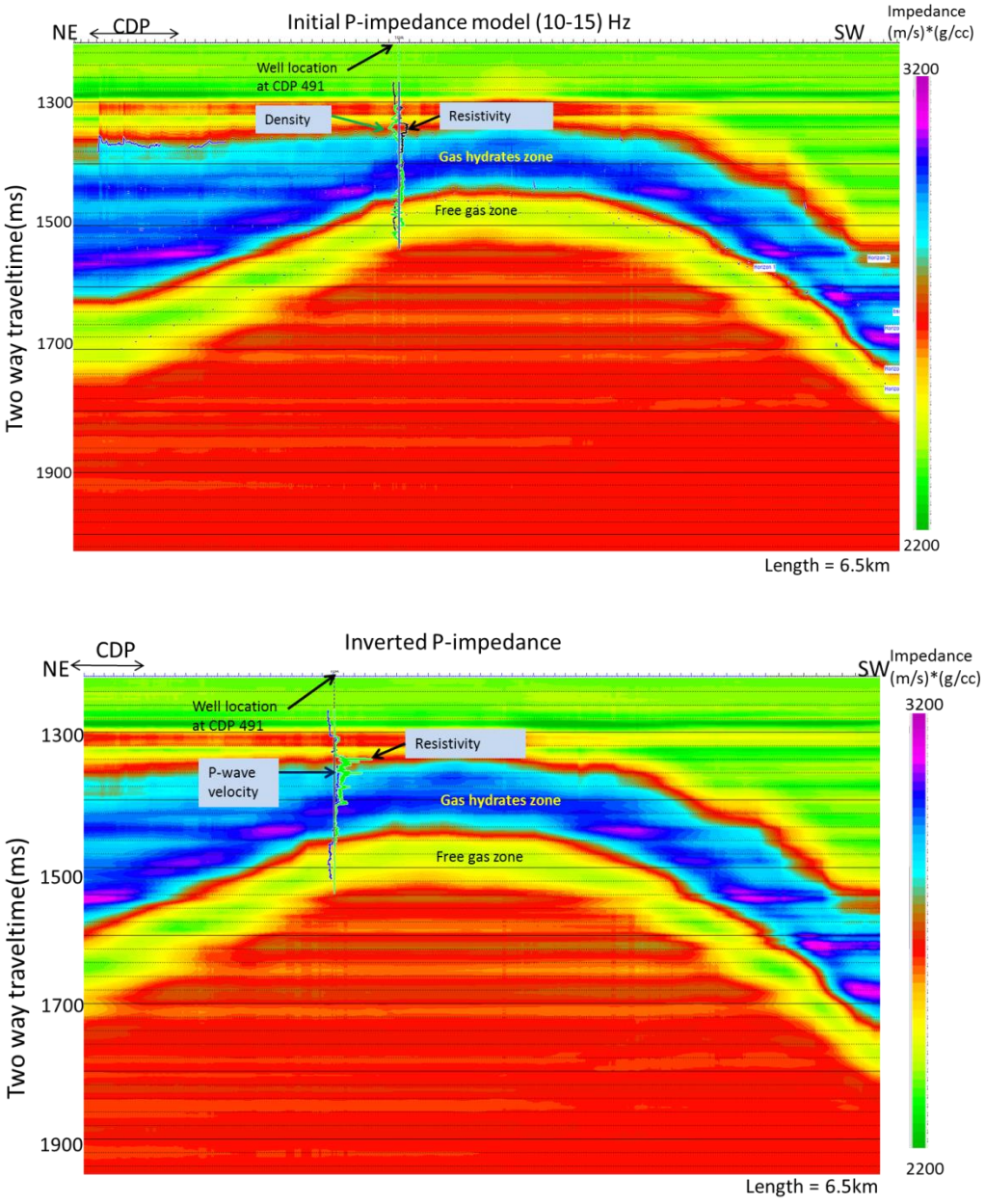

Figure 2.9: Initial model 10-15 Hz on the top and the inverted impedance (bottom). By comparing the inverted P-impedances from this figure and Figure 10, it is observed that starting with a low frequency initial impedance model produces the same features as obtained when starting with a high frequency initial model. This is useful considering the general quality of field seismic data is dominated by the low frequency. Hence the lack of higher frequencies may not be an important factor in obtaining better P-impedance inversion result.

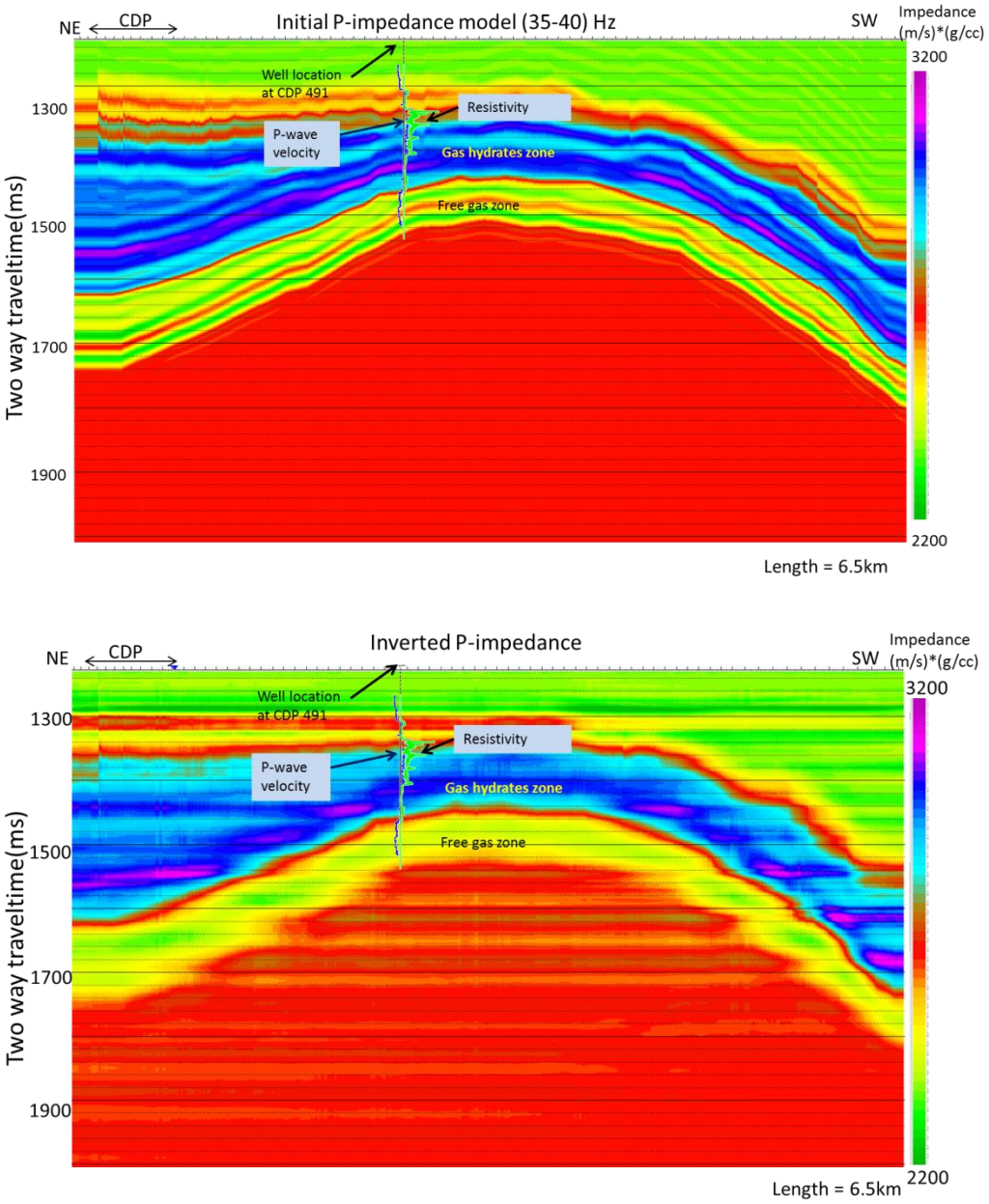

Figure 2.10: Initial model 35-40 Hz on the top and the inverted impedance (bottom). By comparing the inversion results from Figure 9 and Figure 10 it is observed that despite of the considerable difference in the initial impedance models, the inverted impedance results almost appear the same.

2.5 REFERENCES

Collett, T., M. Riedel, J. Cochran, R. Boswell, J. Presley, P. Kumar, A. Sathe, A. Sethi, M. Lall, V. Sibal, and the National Gas Hydrate Program (NGHP) Expedition 01 Scientists, 2008, Indian NGHP Expedition 01 initial reports: Directorate General Hydrocarbon report.

Lancaster, S., and Whitcombe, D., 2000. "Fast track coloured Inversion." In SEG Technical Program Expanded Abstracts 2000, 1572–1575. SEG Technical Program Expanded Abstracts. Society of Exploration Geophysicists. http://dx.doi.org/10.1190/1.1815711.

Levy, S., and P. Fullagar. 1981. "Reconstruction of a Sparse Spike Train from a Portion of Its Spectrum and Application to High-resolution Deconvolution." GEOPHYSICS 46 (9) (September 1): 1235–1243. doi:10.1190/1.1441261.

Lindseth, R., 1979. Synthetic sonic logs- a process for stratigraphic interpretation. GEOPHYSICS 44, 3–26.

Oldenburg, D., Scheuer, T., Levy, S., 1983. Recovery of the acoustic impedance from reflection seismograms. GEOPHYSICS 48, 1318–1337.

Russell Brian H., 1988. Introduction to Seismic Inversion Methods, Course Notes Series. Society of Exploration Geophysicists.

Russell, B., and Hampson, D., 1991. "Comparison of Poststack Seismic Inversion Methods." In SEG Technical Program Expanded Abstracts 1991, 876–878. SEG Technical Program Expanded Abstracts. Society of Exploration Geophysicists. http://dx.doi.org/10.1190/1.1888870.

Sen, Mrinal K. 2006. Seismic Inversion. Society of Petroleum Engineers.

Torres-Verdín, C., Victoria, M., Merletti, G., and Pendrel, J., 1999, Trace-based and geostatistical inversion of 3-D seismic data for thin sand delineation: An application to San Jorge basin, Argentina: The Leading Edge, 18, 1070–1077.

Chapter 3: Prestack inversion

This chapter presents inversion of prestack seismic data using an inversion process to estimate multiple attributes, particularly P and S-impedances and Poisson's ratio. I briefly discuss the principles of prestack inversion implemented in the commercially available Hampson-Russell®, followed by presentation of the application of prestack inversion to the 2D seismic line of my study region. Finally I discuss the results and provide my observations from the 2D seismic line used for the study.

3.1 INTRODUCTION

Prestack inversion is a method of statistical inversion that uses seismic reflection amplitude, traveltime and waveform information from multi-offset prestack CMP seismic data to invert for multiple elastic properties such as acoustic impedance and Poisson's ratio (Sen, 2006, p.85). Prestack inversion has commonly been used to invert for P and S-impedances (Goodway et al., 1997; Gray and Anderson, 2000). Interpretation of these parameters is an important tool for lithology and fluid discrimination because these elastic properties can be linked quantitatively to reservoir properties of interest. (Goodway et al., 1997; Burianyk, 2000; Gray and Andersen, 2000). Several approaches from various investigations have been adopted for prestack inversion. Generalized linear inversion (GLI) is one class of such methods (Tarantola, 1986; Mora, 1987; Demirbag et al., 1993; Pan et al., 1994). Global optimization based methods such as simulated annealing (SA) and genetic algorithms (GA) are another class of prestack seismic inversion that have also been used, especially inversion for non-linear situations (Sen and Stoffa, 1991; Mallick, 1995).

For the purpose of the present study, Hampson-Russell®, an industrial inversion software package that includes inversion applications is used for preforming prestack

inversion. The inversion process is called simultaneous because P-impedance (Z_p), S-impedance (Z_s) are inverted for simultaneously. These parameters can be readily expresses in terms of other physical quantities including individual elastic constants, P and S- wave velocity and Poisson's ratio (Hampson and Russell, 2005).

3.2 PRE-STACK INVERSION PRINCIPLES

The simultaneous inversion methodology used in STRATA® expands the work of Simmons and Backus (1996) and Buland and Omre (2003). The prestack inversion algorithm in STRATA® is based on three main assumptions: 1) Validity of a linear approximation of reflectivity, 2) PP, and PS reflectivity are representable as functions of angle given by the Aki-Richards equations (Aki and Richards, 2002), and , significantly, 3) the existence of a linear relationship between P-impedance and S-impedance. These assumptions generally require small contrasts in Vp, Vs and ρ across a reflecting interface and small (less than 30^o) angles of incidence.

Zoeppritz equations (Zoeppritz, 1919) are the most general representation of the P and S–wave reflection, transmission and mode-conversion coefficients. Although the Zopperitz equations are exact representations, using them to understand the physical significance of the reflection and transmission coefficients is difficult. Aki and Richards (2002) have given linear approximations, in terms of the $\sin^2$ of the angle of incidence, of the reflection coefficients assuming small contrasts in layer impedances and small angles of incidence. The P-P reflection coefficient (r_{PP}) as a function of angle of incidence (θ) in the Aki-Richards representation as:

$$r_{PP\theta} = c_1 r_P + c_2 r_S + c_3 r_D \,, \qquad 3.1$$

where,

$$r_P = \left[\frac{\Delta V_P}{V_P}\right], \tag{3.2}$$

$$r_S = \left[\frac{\Delta V_S}{V_S}\right], \tag{3.3}$$

$$r_D = \frac{\Delta \rho}{\rho}, \tag{3.4}$$

$$c_1 = 1 + (\tan^2\theta), \tag{3.5}$$

$$c_2 = -4\left(\frac{V_S}{V_P}\right)^2 (\tan^2\theta), \tag{3.6}$$

$$c_3 = 0.5(\tan^2\theta) - 2\left(\frac{V_S}{V_P}\right)^2 (\sin^2\theta), \tag{3.7}$$

As mentioned earlier, the work done by Buland and Omre (2003) is an underlying aspect of the present inversion technique. According to them, the reflection coefficient in Equation 3.1 can also be extended to a time-continuous reflectivity function (Stolt and Weglein, 1985) and can be represented as:

$$r_{PP\theta} = c_1 \frac{\partial}{\partial t}\ln(V_P) + c_2 \frac{\partial}{\partial t}\ln(V_S) + c_3 \frac{\partial}{\partial t}\ln(\rho), \tag{3.8}$$

Comparing Equation 3.1 and Equation 3.8 it can be observed that for each of the corresponding terms in brackets in the right hand size of Equation 3.1,

$$\left[\frac{\Delta V_P}{V_P}\right] = \frac{\partial}{\partial t}\ln(V_P), \quad \left[\frac{\Delta V_S}{V_S}\right] = \frac{\partial}{\partial t}\ln(V_S), \quad \frac{\Delta \rho}{\rho} = \frac{\partial}{\partial t}\ln(\rho). \tag{3.9}$$

$$\frac{\Delta V_P}{V_P} = \frac{\partial}{\partial t}(\ln V_P) \ , \qquad 3.10$$

$$\frac{\Delta V_S}{V_S} = \frac{\partial}{\partial t}(\ln V_S), \qquad 3.11$$

$$\frac{\Delta \rho}{\rho} = \frac{\partial}{\partial t}(\ln \rho) \qquad 3.12$$

Hampson and Russell (2005) derived the linearized relationship between reflectivity for $\theta = 0$ at the i^{th} interface and impedance Z_{Pi} of the i^{th} and Z_{Pi+1} $(i+1)^{th}$ layer, that I have presented it in a modified manner using the partial differentiation operator with respect to time as $\frac{\partial}{\partial t}$ instead of Δ:

$$r_{Pi} \approx \frac{1}{2}\frac{\partial}{\partial t}(\ln Z_{Pi}) = \frac{1}{2}[\ln Z_{Pi+1} - \ln Z_{Pi}] \quad . \qquad 3.13$$

The reflectivity is related to the seismic trace as the convolution between the wavelet and the reflectivity. Equation 3.13 may be represented in matrix form as:

$$\begin{bmatrix} r_{P1} \\ r_{P2} \\ \vdots \\ r_{PN} \end{bmatrix} = \frac{1}{2}\begin{bmatrix} -1 & 1 & 0 & \cdots \\ 0 & -1 & 1 & \ddots \\ 0 & 0 & -1 & \ddots \\ \vdots & \ddots & \ddots & \ddots \end{bmatrix}\begin{bmatrix} L_{P1} \\ L_{P2} \\ \vdots \\ L_{PN} \end{bmatrix} \quad , \qquad 3.14$$

where,

$$L_P = ln\, Z_P \quad . \qquad 3.15$$

and r_P is defined in Equation 3.13. A compact representation of reflectivity r in the matrix form where $\boldsymbol{R}$ is a vector of reflectivity in Equation 3.14 is

$$\boldsymbol{R} = \frac{1}{2}\boldsymbol{D}\boldsymbol{L} \quad , \tag{3.16}$$

where $\boldsymbol{D}$ is the matrix representation of differentiation, where $\boldsymbol{L}$ is the vector of the natural log of impedances (from Equation 3.15) of N layers. Similarly the shear and density reflectivity (Hampson and Russell, 2005) can be written as

$$r_{Si} \approx \frac{1}{2}[L_{Si+1} - L_{Si}] \quad , \tag{3.17}$$

Where L_S is the natural logarithm of S-impedance, which can be represented as:

$$L_{Si} = ln\, Z_{Si} \quad , \tag{3.18}$$

And density reflectivity is

$$r_{Di} \approx \frac{1}{2}[L_{Di+1} - L_{Di}] \quad , \tag{3.19}$$

where L_D is the natural logarithm of density, which can be represented as:

$$L_{Di} = ln\, \rho_i \quad . \tag{3.20}$$

As discussed in Section 2.1, the seismic trace can be represented as the convolution of wavelet and reflectivity. Then using Equation 3.16, a poststack seismic trace ($\boldsymbol{s}$) can be written as a convolution of the wavelet and reflectivity, which can be represented in the matrix form as the multiplication of $\boldsymbol{W}$, the convolution matrix made of the wavelet, $\boldsymbol{D}$ is the matrix representation of differentiation and $\boldsymbol{L}$ is the matrix made of natural logarithms of impedances, defined in the Equation 3.15,

$$\boldsymbol{s} = \frac{1}{2}\boldsymbol{WDL} \quad , \tag{3.21}$$

From the Aki-Richards linearization of Zoeppritz equations (Aki and Richards, 2002), P-wave reflection coefficients can be represented as a function of the average of the incident and transmitted angles of the P-wave. Hence the prestack seismic reflection trace, which is the convolution of the angle-dependent wavelet and reflection coefficient, using the Fatti (1994) simplification in Equation 3.1, can be represented as the multiplication of the $\boldsymbol{W_\theta}$, matrix representation of the angle dependent wavelet, $\boldsymbol{D}$ the matrix representation of the differentiation and with $\boldsymbol{L_p}$, $\boldsymbol{L_S}$, $\boldsymbol{L_D}$ as defined in Equations 3.15, 3.18 and 3.20 respectively.

$$\boldsymbol{s_\theta} = (1/2)c_1\boldsymbol{W_\theta DL_p} + (1/2)c_2\boldsymbol{W_\theta DL_S} + (1/2)c_3\boldsymbol{W_\theta DL_D} \quad , \tag{3.22}$$

where c_1, c_2, c_3 defined in Equations 3.5, 3.6 and 3.8 respectively. One of the main differences between poststack seismic inversion and prestack seismic inversion is that the wavelet in the former method is a constant wavelet whereas the wavelet in the latter one

is angle dependent. For a range of angles, the Equation 3.22 can be written in matrix form as

$$\begin{bmatrix} s_{\theta 1} \\ s_{\theta 2} \\ \vdots \\ s_{\theta N} \end{bmatrix} = \begin{bmatrix} c_1(\theta_1)W_{\theta 1}D & c_2(\theta_1)W_{\theta 1}D & c_3(\theta_1)W_{\theta 1}D \\ c_1(\theta_2)W_{\theta 2}D & c_2(\theta_2)W_{\theta 2}D & c_3(\theta_2)W_{\theta 2}D \\ \vdots & \vdots & \vdots \\ c_1(\theta_N)W_{\theta N}D & c_2(\theta_N)W_{\theta N}D & c_3(\theta_N)W_{\theta N}D \end{bmatrix} \begin{bmatrix} L_p \\ L_S \\ L_D \end{bmatrix} \quad , \qquad 3.23$$

which is of the from

$$\boldsymbol{d} = \boldsymbol{Gm}. \qquad 3.24$$

The impedances can be solved for by inverting the $\boldsymbol{G}$ matrix. However, a drawback of this method is that it does not consider the interdependency between the background trends of P-impedance, S-impedance and density (Hampson and Russell, 2005). Because impedance is the goal of inversion in the present methodology, the linear relationships for the interdependent impedances are given by Hampson and Russell (2005) as follows:

$$L_S = kL_P + k_c + \Delta L_S \quad , \qquad 3.25$$

$$L_D = \mathrm{m}L_P + \mathrm{m_c} + \Delta \mathrm{L_D} \quad , \qquad 3.26$$

where L_P, $L_S$and L_D are defined in Equations 3.15, 3.18 and 3.20, respectively. ΔL_S and ΔL_D are the deviations from the linear relationship. Equations 3.25 and 3.26 represent

straight lines. Analyzing Equation 3.25, it can be observed that if L_S is considered a variable and plotted against L_P , then k represents the slope, and $(k_c + \Delta L_S)$ is the intercept of Equation 3.25. Similarly in Equation 3.26, if L_D considered a variable and plotted versus L_P, then for the straight line thus formed, m is the slope, and m_c is the intercept.

A small change in L_S can be represented by differentiating Equation 3.25. As discussed earlier in this section that D represents the differentiation operator, the differentiation of L_S is represented as:

$$DL_S = kDL_P + D\Delta L_S \quad . \tag{3.27}$$

Where k has been discussed earlier in the context of Equation 3.25. The derivative for Equation 3.26 similarly as for Equation 3.25 is

$$DL_D = \mathrm{m}DL_P + D\Delta L_D \quad . \tag{3.28}$$

Where m has been discussed earlier in the context of Equation 3.26. Notice that the k_c and m_c that are present in Equations 3.25 and 3.26 do not appear in the Equations 3.27 and 3.28 because they are constants.

By substituting the differentiation of the natural logarithm of the impedance (DL, L representing the natural logarithm of impedance in general) in Equations 3.27 and 3.28 in the Fatti (1994) equation in 3.22, the modified Fatti equation is:

$$s_\theta = (1/2)c_1 W_\theta DL_p + (1/2)c_2 W_\theta (kDL_P + D\Delta L_S) + (1/2)c_3 W_\theta (\mathrm{m}DL_P + D\Delta L_D) \quad . \tag{3.29}$$

Where the terms c_1, c_2, c_3 are defined in Equations 3.5, 3.6, 3.7, respectively. By rearranging the terms in Equation 3.29 and grouping the same terms according to the impedances L_p, L_S, L_D the angle-dependent seismic trace (s_θ) can be expressed as

$$s_\theta = \tau_1 W_\theta D L_p + \tau_2 W_\theta D L_S + c_3 W_\theta D \Delta L_D \quad , \tag{3.30}$$

where

$$\tau_1 = (1/2)c_1 + (1/2)\, kc_2 + mc_3 \quad , \tag{3.31}$$

and

$$\tau_2 = (1/2)c_2 \ . \tag{3.32}$$

For a range of angles, Equation 3.29 can be represented in the matrix form as

$$\begin{bmatrix} s_{\theta 1} \\ s_{\theta 2} \\ \vdots \\ s_{\theta N} \end{bmatrix} = \begin{bmatrix} \tau_1 W_{\theta 1} D & \tau_2 W_{\theta 1} D & c_3 W_{\theta 1} D \\ \tau_1 W_{\theta 2} D & \tau_2 W_{\theta 2} D & c_3 W_{\theta 2} D \\ \vdots & \vdots & \vdots \\ \tau_1 W_{\theta N} D & \tau_2 W_{\theta N} D & c_3 W_{\theta N} D \end{bmatrix} \begin{bmatrix} L_p \\ \Delta L_S \\ \Delta L_D \end{bmatrix} . \tag{3.33}$$

This again is in the form of normal equations (Equation 3.23), and the impedances can be solved using matrix inversion techniques. The prestack inversion algorithm in Hampson-Russell® uses an initial guess P-impedance model for stabilizing the matrix inversion. The initial guess model can be represented as

$$[L_P \quad \Delta L_S \quad \Delta L_D]^T = [ln Z_{P0} \quad 0 \quad 0]^T \quad , \qquad 3.34$$

where Z_{P0} is the initial P-impedance guess model. The inverse problem in Hampson-Russell® is solved using an iterative conjugate gradient method applied to solving for the P and S-impedances. When L_P, L_S and L_D are estimated then the estimated values of the P and S-impedances and density are given as:

$$Z_P = exp(L_P) \quad , \qquad 3.35$$

$$Z_S = exp(kL_P + k_c + \Delta L_S) \quad , \qquad 3.36$$

$$\rho = exp(mL_P + m_c + \Delta L_D) \quad . \qquad 3.37$$

3.3 PRESTACK INVERSION OF REAL DATA: METHODOLOGY AND RESULTS

The workflow of prestack inversion in Hampson-Russell® can be represented in the following steps:

1. Generating angle gathers from the processed and NMO corrected CDP gathers. This converts the offset-dependent CDP gathers to angle-dependent gathers. For each set of gathers, angle-dependent wavelets are generated for each range of angles.
2. Estimating the constants k and m of the linear relationships in Equations 3.25 and 3.26 using well logs.
3. Building the initial P-impedance model.

4. Solving the inverse problem in Equation 3.30 to obtain the logarithm values of the impedances
5. Calculating the final values of P-impedance, S-impedance and density using the Equations 3.35-3.36.

The inputs required for prestack inversion are the processed, NMO corrected offset dependent CDP gathers (Figure 3.1). During processing, proper care is taken to preserve the relative amplitude in the seismic traces so they will be suitable for inversion. The dominant frequency range is 50-100 Hz. In the following sections I will go through the steps of prestack inversion and their results achieved when applied to the 2D seismic line from the region of my study.

The first task is the generation of angle gathers from the prestack seismic data. Two sets of angle gathers are generated for angles 0^{o} -45^{o} from the processed, NMO corrected offset dependent CDP gathers. One set is for the near offset data, with angle range of 0^{o} -15^{o} and the second set for far offsets with the angles ranging from 15^{o} -45^{o}. One of the main differences between post-stack inversion and pre-stack inversion is that the wavelet used in pre-stack inversion varies with offset or angle in this case. Wavelet extraction using seismic and well data has been discussed earlier in Chapter 2 and in several publications (Buland and Omre 2003, Danielson and Karlsson, 1984; Lines and Treitel, 1985; Newman, 1986; Nyman et al., 1987; Richard and Brac, 1988; Poggiagliolmi and Allred, 1994). The STRATA® module for prestack inversion in Hampson-Russell® uses statistical methods applied to seismic data for extraction of a zero-phase wavelet. Two wavelets are generated for the corresponding angle gathers; one for near-angle gathers (Figure 3.2) and the other for far-angle gathers (Figure 3.3). In practice offset rather than angle, is the parameter required for extraction of wavelet in the present method. Thus, for the near angle gather, an offset range of 0-500m was used

while for the far angles' gathers, 500-1500m offset range was used for the wavelet extraction. To extract the wavelets a time window of 1400- 1800 milliseconds of the seismic data was chosen because it is the window within which the gas hydrates appear on the seismic data. The extracted wavelets are constant zero phase wavelets, each of length 200 milliseconds with a 25 milliseconds taper. The peak frequency in each wavelet is approximately 80 Hz.

It was discussed in the preceding section that the P and S-impedances and density are interdependent, and there exists linear relationship among them, as represented in the Equations 3.25 and 3.26. The parameters of the linear relationship between the background trends of P-impedance, S-impedance and density are obtained from the regression of $\ln Z_P$ on $\ln Z_S$ (Figure 3.4) from which k and k_c are obtained and the regression of $\ln Z_D$ on $\ln Z_P$ (Figure 3.5) gives the parameters m and m_c. The values obtained are $k = 3.87476$, $k_c = -26.6849$ and $m = 1.04893$, $m_c = -7.77296$.

The next step in prestack inversion is the building of an initial guess impedance model (Figure 3.6, Figure 3.7 and Figure 3.8). Pre-stack inversion in Hampson-Russell® requires initial models for P-impedance, S-impedance and density. The principles for building an initial model discussed in Section 2.2.4 of the Chapter 2 are also applicable in building an initial impedance model for prestack seismic inversion. Horizons obtained from the interpretation of seismic data are used here to build a low frequency initial model using the NMO corrected CDP gathers and well log data. Smoothly varying initial low frequency models of P- impedance, S- impedance and density are shown in Figures 3.6, 3.7, and 3.8 respectively. The advantage of using a low frequency initial model is that it constrains the model search space (Sen, 2006, p.60, Sen and Stoffa, 1995, p.48). It also incorporates the low frequency component derived from well log data into the inversion result, thus addressing the issue of generating only relative values and not

absolute values in the inversion result that arises from the band limitation in the lower frequency range of seismic data (Ghosh, 2000).

Prior to prestack inversion of all the CDP gathers, inversion analysis is done at the well location. Figure 3.9 shows the result of prestack inversion at the well location. It shows the four quantities that are inverted for in the prestack inversion, P-impedance, S-impedance, density and Vp/Vs. It is observed that the inverted logs and the original logs match very well. The resultant synthetic seismic traces for each of the angles at CDP 490 are also shown in Figure 3.9. The synthetic traces have a total correlation factor of 0.65 with the original seismic traces at the well location and a total error of 0.74. Using the initial models as a starting guess, the resulting P-impedance, S-impedance, Vp/Vs and inverted density sections are shown in Figure 3.10, 3.11, 3.12, and 3.13, respectively. From the inverted P-impedance result shown in Figure 3.10 it is observed that there is a significant improvement in the resolvability of the geologic features when compared to the poststack impedance inversion results. The inverted P-impedance values have a range of 2046 (m/s)×(g/cm^3) to 3082 (m/s)×(g/cm^3). The high P-impedance zone is the gas hydrates region. The impedance in the GHSZ varies between 2800-3080 g/cm^3 × m/s, which is almost in the same range as the results obtained from prestack inversion. The low P- impedance zone may correspond to free gas, which is generally expected from marine gas hydrate regions. Again, the results are realistic only for the two-way traveltime of the logged depth which is around 1500 milliseconds. Figure 3.11 shows the inverted S-impedance. It is observed that the gas hydrates region has higher S-impedance as emphasized by the cooler colors. The presence of gas hydrates increases the S-impedance of the host rocks as gas-hydrates have higher shear modulus compared to both gas and water, which are generally the pore filling fluids. A possible interpretation of increase in shear modulus in the presence of gas-hydrates is that they form a part of the

load bearing matrix, hence increasing the rigidity of the rock. Figure 3.12 shows the Vp/Vs obtained from pre-stack inversion. Vp/Vs varies proportionally with Poisson's ratio. Hence low values of Vp/Vs are interpreted as gas regions. It is observed in Figure 3.11 that the Vp/Vs increases in the free gas zone. The Vp/Vs is low in the gas hydrates region as major portion of the gas is used in the formation of gas-hydrates. Figure 3.13 is the inverted density obtained from pre-stack inversion. It is observed that there is no anomaly on the density section because the presence of gas-hydrates doesn't affect any changes in density even though it replaces water from the pore spaces, because the density of the gas-hydrates is very close to that of water.

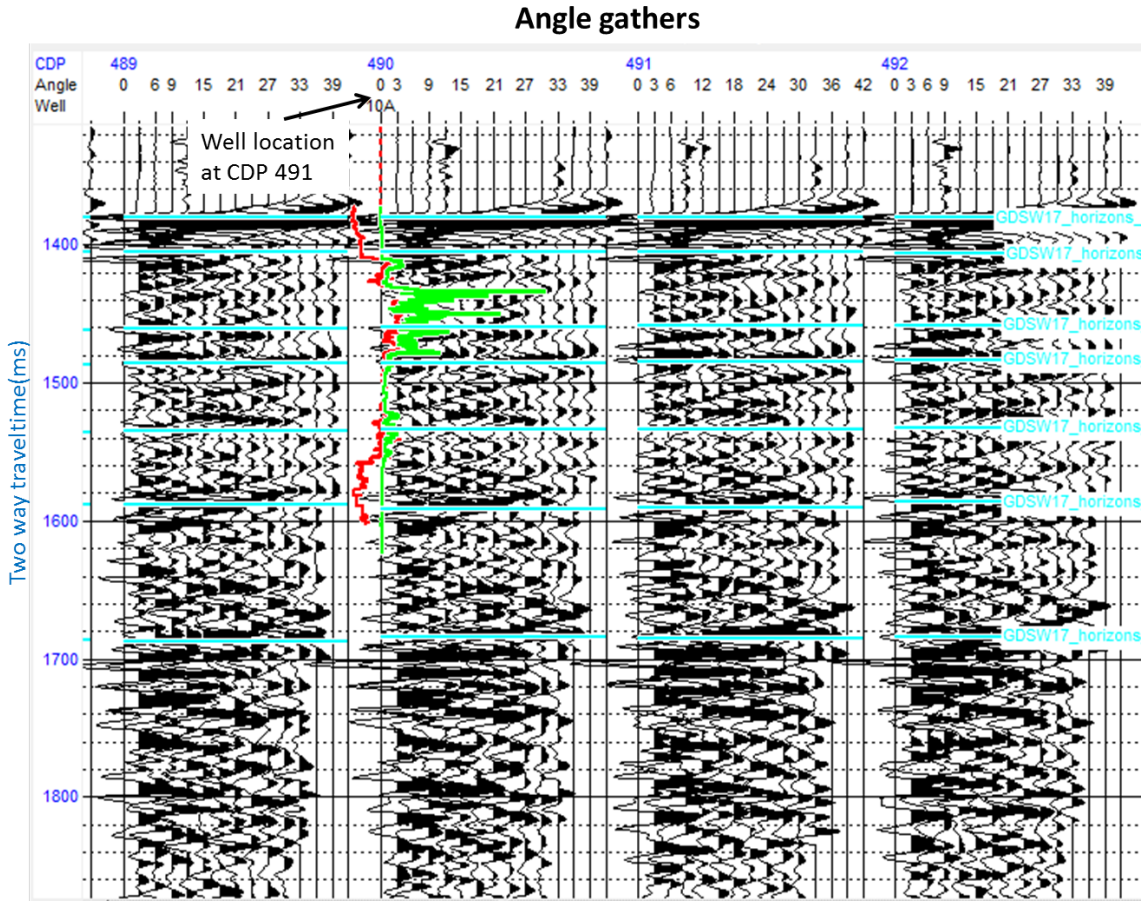

Figure 3.1: NMO corrected CMP gathers for CMPs near CMP 490 (well location). Resistivity log (green) and P-wave log (red) is shown in the figure. The interpreted horizons can also be shown on the records. Angle gathers were created for angles ranging from 0^{o} to 45^{o}.

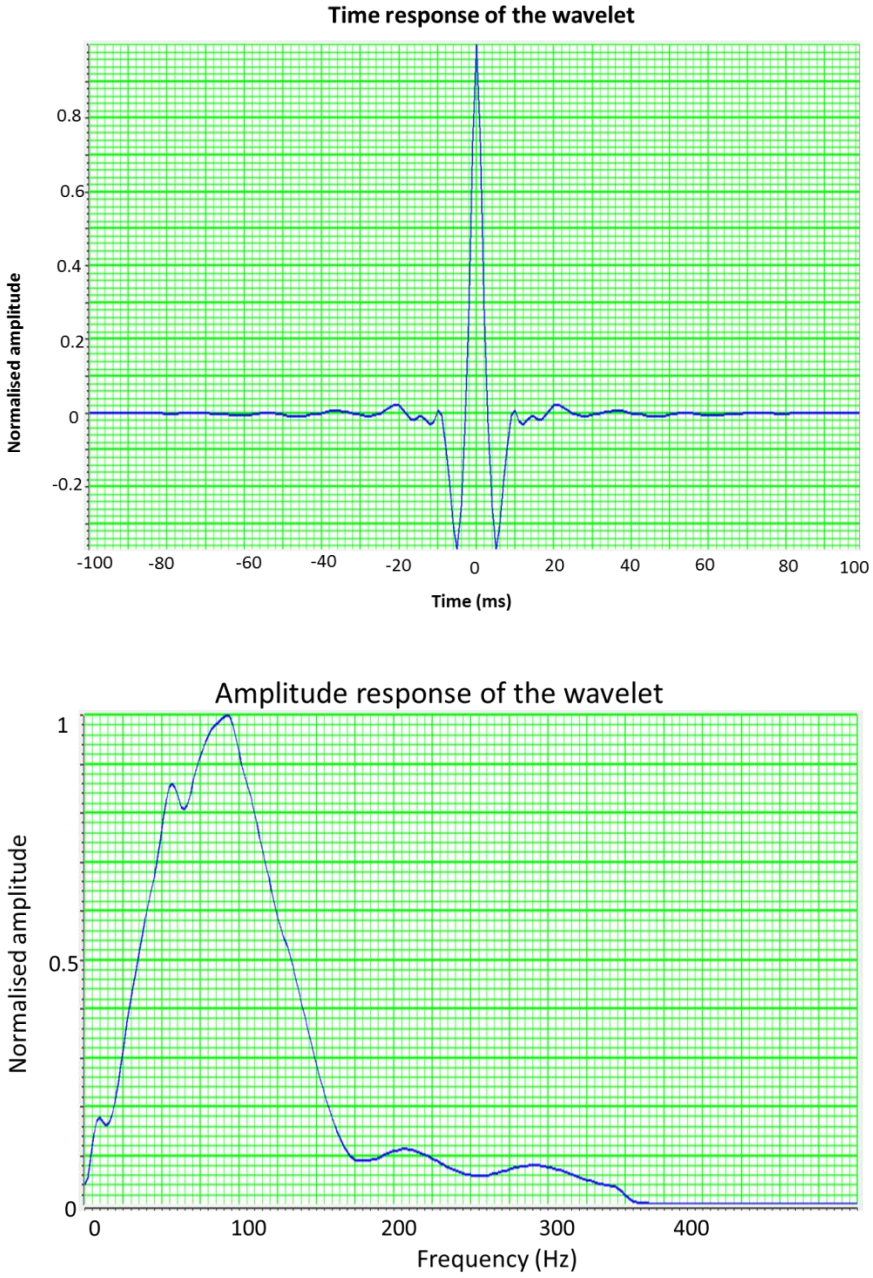

Figure 3.2: Near offset (0-500m) wavelet with its time response on the top and amplitude response below. The wavelet is zero phase and the dominant frequency is in the range 50-80 Hz.

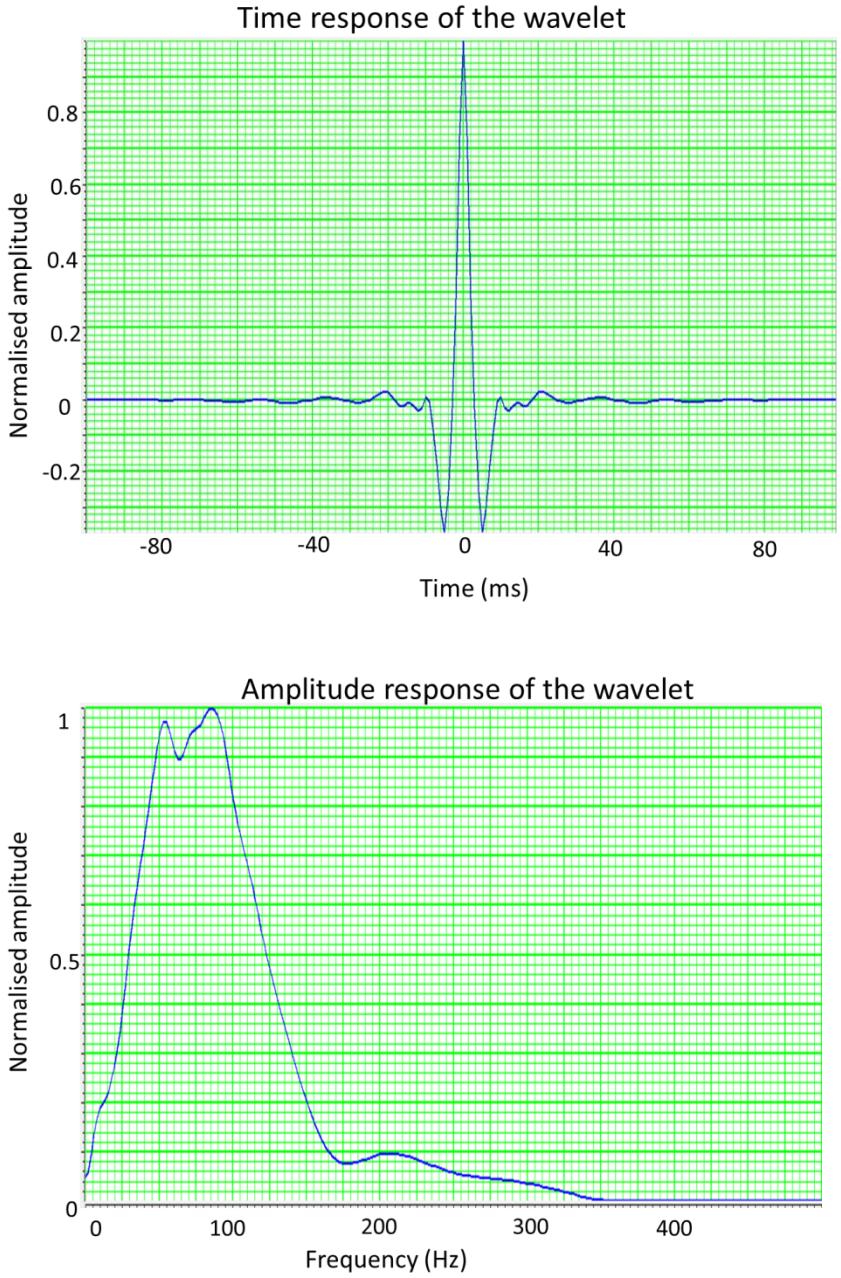

Figure 3.3: Far offset (500-1500m) wavelet with its time response on the top and amplitude response below. The wavelet is zero phase and the dominant frequency is in the range 50-80 Hz.

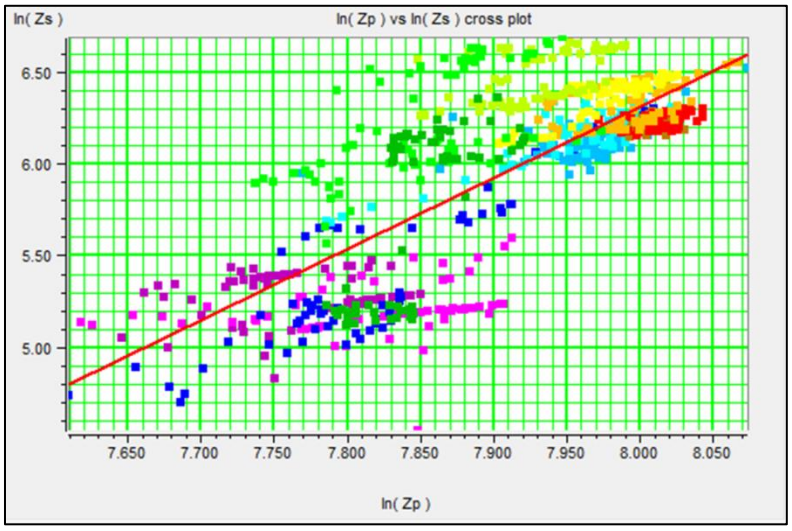

Figure 3.4: Regression of ln(Zs) on ln(Zp). The slope of the regression line gives the value of the slope k and the intercept the value of kc in Equation 3.22. The values are used to obtain S-impedance (Zs) from P-impedance (Zp).

.

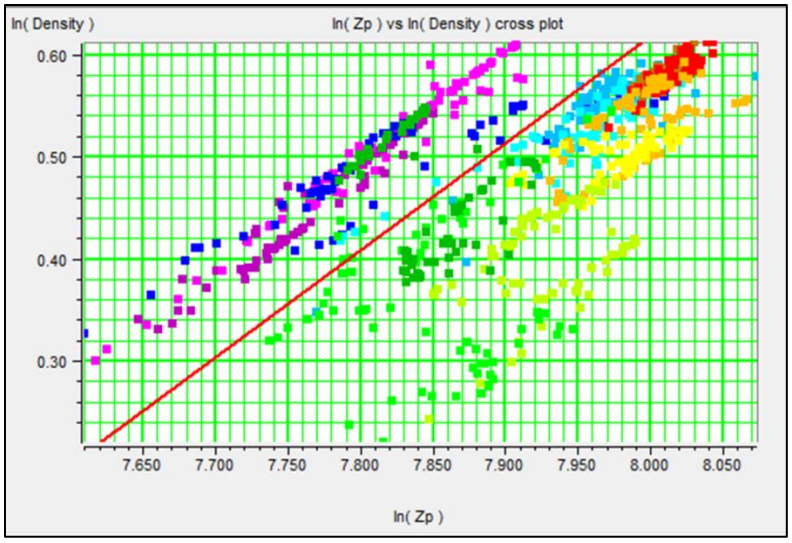

Figure 3.5: Regression of $ln(\rho)$ on $ln(Z_p)$. The slope of the regression line gives the value of the slope m and the intercept the value of m_c in Equation 3.23. The values are used to obtain density (ρ) from P-impedance (Z_p).

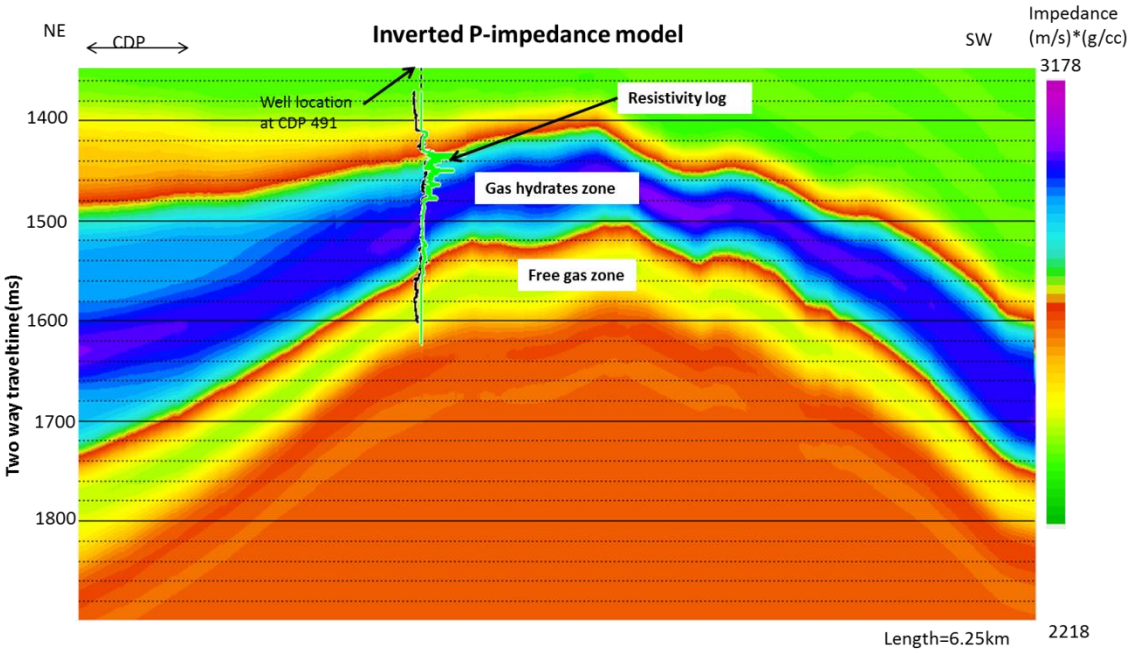

Figure 3.6: Low frequency initial P-impedance model. The color panel on the right shows the range of impedance which varies from 2280-2800 (g/cc) (m/s). The marked gas hydrate zone is shows high impedance. Beneath the gas hydrate zone is a low impedance layer, which is the free gas layer. The resistivity log is also shown. High resistivity coincides with the high P-impedance zone. The P-wave velocity (black curve) also coincides with the high P-impedance zone. Gas-hydrates with their higher shear modulus compared to water or gas increases the bulk modulus of the host rock.

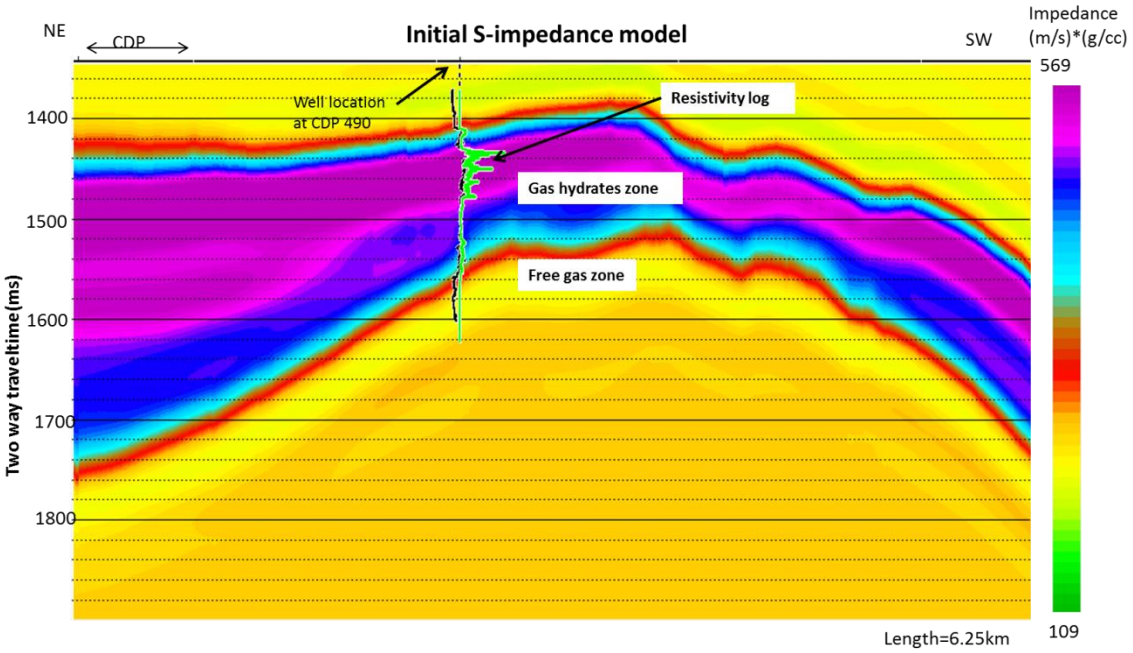

Figure 3.7: Low frequency initial S-impedance model. The color panel on the right shows the range of impedance which varies from 109-569 (g/cc)(m/s). The marked gas hydrate zone is shows high impedance. Beneath the gas hydrate zone is a low impedance layer, which is the free gas layer. The resistivity log is also shown. High resistivity coincides with the high S-impedance zone. Higher S-impedance also coincides with the high P-wave velocity log (black curve). Gas-hydrates with their higher shear modulus compared to water or gas increases the shear modulus of the host rock.

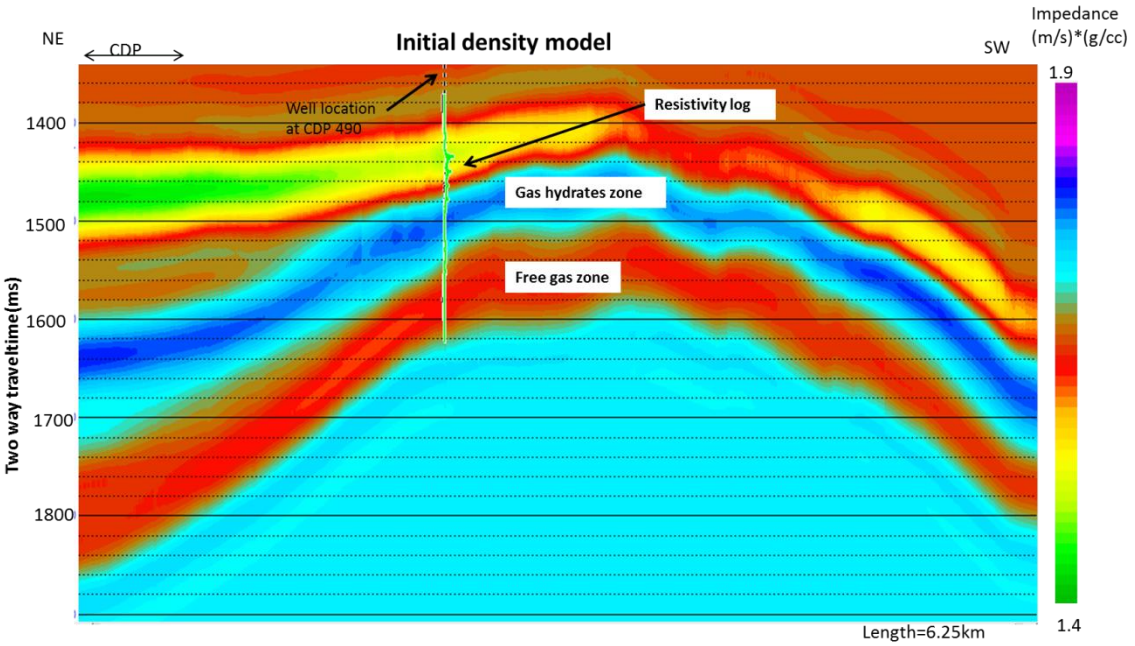

Figure 3.8: Low frequency initial density model. The color panel on the right shows the range of density which varies from 1.4-1.9 (g/cc). The marked gas hydrate zone shows high impedance. Along with P and S-impedance initial model, an initial density model is required for pre-stack inversion.

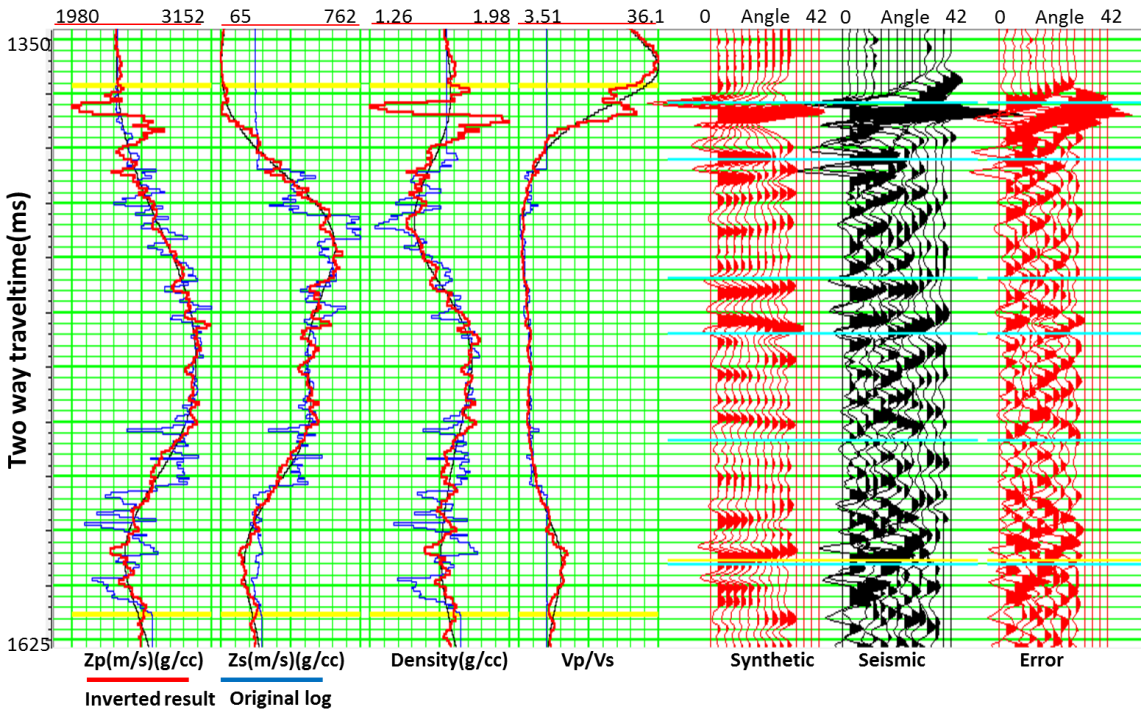

Figure 3.9: Inversion analysis at the well location. Four panels on the left panel show the comparison between the original log (blue) and the inverted results (red). From left to right the displayed logs are Zp, Zs, density, Vp/Vs. The synthetic angle gathers are shown in red and the original angle gathers at CDP 490 are shown along with the error at every angle.

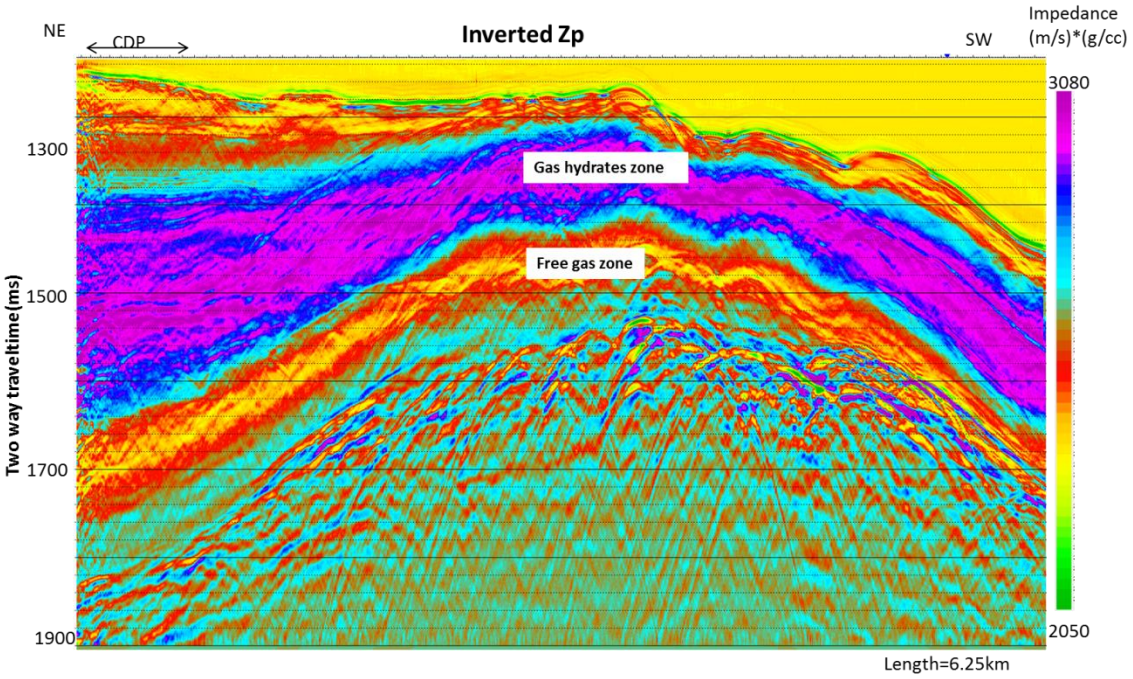

Figure 3.10: Inverted P-impedance. The range of impedance is 2050(g/cc) (m/s) the green end to 3050 (g/cc) (m/s) the purple end. The gas hydrates region has the highest impedance. The impedance in the GHSZ varies between 2800-3080 g/cm^3 × m/s. The free gas zone beneath the gas hydrates zone has low impedance.

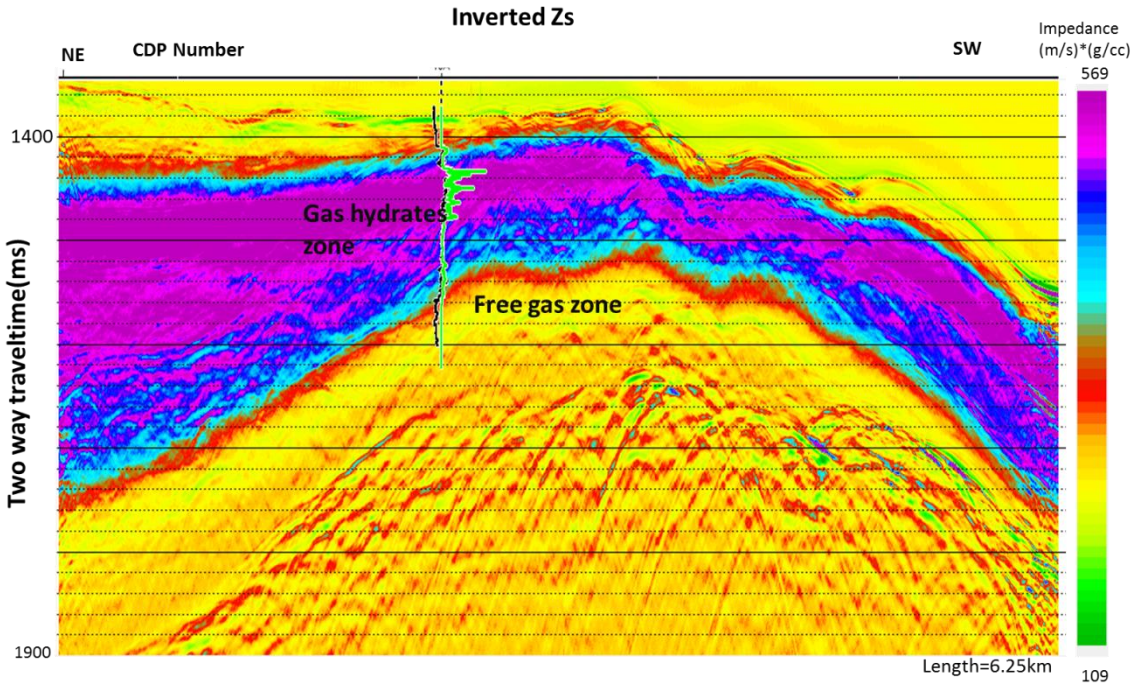

Figure 3.11: Inverted S-impedance along the seismic profile. The range of impedance is 109 (g/cc) (m/s) the lower (green) end to 569 (g/cc) (m/s) the higher (purple) ends. In the gas hydrates region the density varies from 1.7 g/cc to 1.8 g/cc.

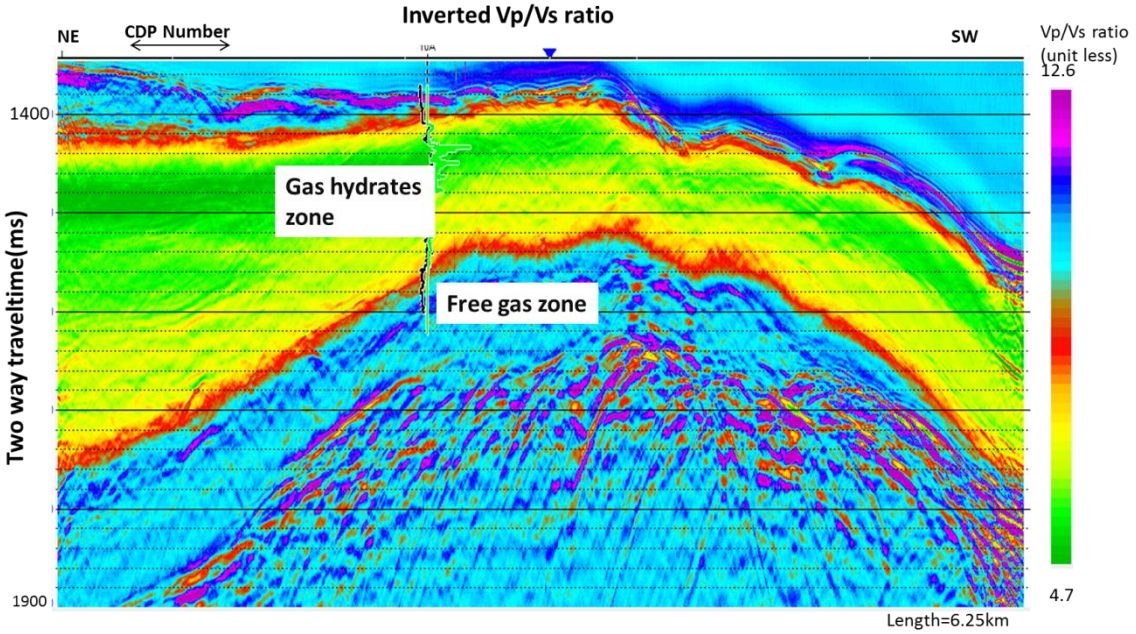

Figure 3.12: Inverted Vp/Vs along the seismic profile. The ratio varies from 4.7 at the lower end (green) end to 12.6 towards the higher (purple) end. In the gas-hydrates zone Vp/Vs ratio is low compared to the surrounding regions. This is expected because the gas in the pore spaces has been used up for the formation of gas hydrates hence decreasing the Vp/Vs ratio. The free gas region has higher Vp/Vs values.

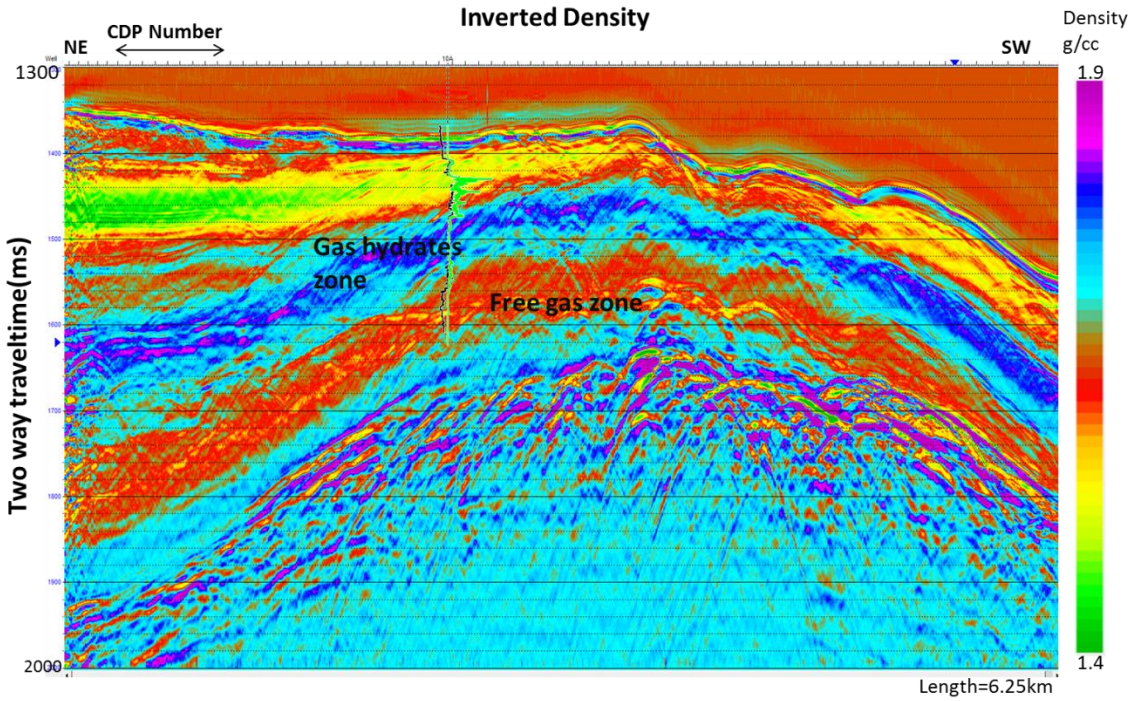

Figure 3.13: Inverted density along the seismic profile. The range of impedance is 1.4 g/cc at the lower (green) end to 1.9 g/cc the higher (purple) end. In the gas hydrates region the density varies from 1.7 g/cc to 1.8 g/cc.

3.4 SUMMARY

In comparison with the impedance results from poststack inversion, prestack inversion provides a broader range of parameters, albeit more computationally intensive method. The goal was to obtain multiple impedance attributes, P-impedance (Zp), S-impedance (Zs) and density, from the seismic data. NMO corrected CDP gathers obtained from seismic data processing done in the previous chapter were used as the input data for prestack inversion. Angle gathers ranging from angles 0^{o}- 45^{o} were generated and two wavelets corresponding to near offset and far offset were generated too. These were used for inversion analysis at the well location which produced a very close approximation of the seismic trace at the well location. Using the horizons interpreted in the previous chapter a low frequency initial model was built and inversion was done for the whole line producing Zp, Zs and density. Comparing the Zp obtained from poststack inversion and prestack inversion it is observed that there is more detailed delineation in prestack inversion results. Because the resolvability of geologic features was poor in poststack impedance inversion, prestack inversion provided an alternate means to invert seismic data for P-impedance. Better resolvability of the elastic properties is important because they are used in the next chapter for determination of gas hydrates saturation. The better the resolution of the impedance result, the better will be the delineation of the gas hydrates saturated zone.

3.5 REFERENCES

Aki, K., and P. G. Richards, 2002, Quantitative seismology, 2nd Edition: W. H. Freeman and Company.

Buland, Arild, and Henning Omre. "Bayesian Linearized AVO Inversion." Geophysics, 68, no. 1 (January 2003): 185–198. doi:10.1190/1.1543206.

Burianyk, M., 2000, Amplitude-versus-offset and seismic rock property analysis: A primer: CSEG Recorder, 25, No. 9, 6–16.

Castagna, J. P., M. L.Batzle, and R. L.Eastwood, 1985, Relationships between compressional-wave and shear-wave velocities in clastic silicate rocks: Geophysics, 50, 571–581.

Danielson, V., and Karlsson, T. V., 1984, Extraction of signatures from seismic and well data: First Break, 2, no. 4, 15–21.

Demirbag, E., Coruh, C., and Costain, J. K., 1993, Inversion of P-wave AVO, in Offset-dependent reflectivity—Theory and practice ofAVO Analysis: Soc. Expl. Geophys., 287–302.

Fatti, J., G.Smith, P.Vail, P.Strauss, and P.Levitt, 1994, Detection of gas in sandstone reservoirs using AVO analysis: a 3D seismic case history using the Geostack technique: Geophysics, 59, 1362–1376.

Gardner, G. H. F., L. W.Gardner, and A. R.Gregory,1974, Formation velocity and density — The diagnostic basics for stratigraphic traps: Geophysics, **50**, 2085–2095.

Goodway, W., Chen, T., and Downton, J., 1997, Improved AVO fluid detection and lithology discrimination using Lame petrophysical parameters; "Lambda*Rho", "Mu*Rho" and "Lambda/Mu fluid stack", from P and S Inversions: Ann. Mtg., Can Soc. Expl. Geophys., Abstracts, 148–151.

Gray, D., and Andersen, E., 2000, Application of AVO and inversion to formation properties: World Oil, 221, July, 85–90.

Hampson, D. P., Russell, B. H., and Brad Bankhead. “Simultaneous Inversion of Prestack Seismic Data.” SEG Technical Program Expanded Abstracts 2005. 0 vols. Society of Exploration Geophysicists, 2005. 1633–1637. Web. 3 Dec. 2012. SEG Technical Program Expanded Abstracts.

Lines, L. R., and Treitel, S., 1985,Wavelets, well logs and Wiener filters: First Break, 3, No. 8, 9–14.

Mallick, S., 1995, Model-based inversion of amplitude-variations with offset data using a genetic algorithm: Geophysics, 60, 939–954.

Mora, P., 1987, Non-linear two-dimensional elastic inversion of multioffset seismic data: Geophysics, 52, 1211–1228.

Newman, Barry J. 1986. Deconvolution of Noisy Seismic data—A Method for Prestack Wavelet Extraction. GEOPHYSICS 51 (1) (January): 34–44. doi:10.1190/1.1442037.

Nyman, D. C., Parry, M. J., and Knight, R. D., 1987, Seismic wavelet estimation using well control: 57th Ann. Internat. Mtg., Soc. Expl. Geophys., Expanded Abstracts, 535–537.

Pan,G. S.,Young, C.Y., and Castagna, J. P., 1994, An integrated targetorientated prestack elastic waveform inversion: sensitivity, calibration, and application: Geophysics, 59, 1392–1404.

Poggiagliolmi, E., and Allred, R.D., 1994, Detailed reservoir definition by integration of well and 3-D seismic data using space adaptive wavelet processing: The Leading Edge, 13, 749–754.

Richard, V., and Brac, J., 1988, Wavelet analysis using well log information: 58th Ann. Internat. Mtg., Soc. Expl. Geophys., Expanded Abstracts, 946–949.

Richards, P.G., and Frasier, C.W., 1976, Scattering of Elastic Waves from Depth-dependent Inhomogeneities, Geophysics, Vol. 41, p. 441-458.

Sen, M. K., and Stoffa, P. L., 1991, Nonlinear one-dimensional seismic waveform inversion using simulated annealing: Geophysics, 56, 1624–1638.

Simmons, J. L. and M. M.Backus, 1996, Waveform-based AVO inversion and AVO prediction-error: Geophysics, 61, 1575–1588.

Tarantola, A., 1986,Astrategy for nonlinear elastic inversion of seismic reflection data: Geophysics, 51, 1893–1903.

Zoeppritz, K., 1919, Erdbebenwellen VIII B. Über Reflexion and durchgang seismischer wellen duch unstetigkeitsflachen, , Gottinger Nachr. 1, p. 66-84.

Chapter 4: Gas Hydrates Saturation Estimation

In this chapter I present the primary results of my thesis - the estimation of gas hydrates saturation using surface seismic data calibrated with well data. This was accomplished with computed impedance profiles estimated by two different inversion approaches using different (poststack and prestack) types of data. In this chapter I use the inversion attributes and the well logs to calculate gas hydrates saturation. First I briefly discuss some of the previous approaches to the calculation of gas hydrate concentration. Then I introduce the methods for predicting well logs using multi-attribute analysis and neural networks. Following this, I discuss the principles of gas hydrates estimation method I used in my analysis. Finally I present the gas hydrates saturation results and discuss the results.

4.1 INTRODUCTION

Historically, gas-hydrate saturation has been estimated by different geophysical methods using both surface and borehole based observations. Some of these methods involve relating gas hydrates saturation to seismic propagation velocities, whereas some other methods use rock physics models to estimate the amount of gas hydrates. Wood et al.(1994), Yuan et al.(1996), Korenaga et al. (1997) used the Wyllie et al. (1958) time average equation, that related gas-hydrates saturation to acoustic velocity and porosity, to calculate saturation. Ecker et al. (2000) have used theoretical rock physics models for the quantification of gas hydrates in marine sediments. They have used interval velocities obtained from stacking velocity analysis, in rock physics models to calculate porosity. Porosity thus calculated is under-predicted in gas-hydrates zones. This anomaly is introducing gas-hydrates saturation as a factor in the rock physics models, which accounts for the reduction in porosity. Some other methods, for example Ojha et. al.

(2010), have used amplitude versus angle (AVA) to model P-wave reflection data from a BSR to estimate gas-hydrate saturation.

I present another method to estimate gas-hydrate saturation at all trace locations along a seismic profile. The novelty of the approach lies in the method for estimation of well logs that are used for estimating gas-hydrate saturation from seismic observations. The Hampson-Russell® software application EMERGE® is used to statistically predict well log properties from seismic observations in the present study. The algorithm for well log prediction uses a multivariate analysis of seismic attributes and subsequent use of neural-network to estimate well log properties from seismic attributes. Using this method a desired well log property is estimated at any seismic trace location. Water saturation can be represented as a function of formation resistivity and porosity by Archie's equation (Archie, 1942). Assuming that the pores are either water saturated or gas-hydrates saturated, gas-hydrates saturation is given by the fractional pore-space that is not occupied by water (Lu and McMechan, 2002). Because porosity and resistivity are measured only at well location, the values of porosity and resistivity that are required to estimate water saturation are available only at the well location. Using a subset of seismic attributes identified by multivariate analysis, neural networks were employed to estimate these two log properties can be estimated at any trace location. With the predicted formation resistivity and porosity, the gas hydrates saturation can be calculated as the fractional pore space not saturated with water, along the complete seismic profile.

Historically a variety of seismic attributes have been used to predict well logs (for example, Anderson, 1996; Schultz et al., 1994; Hampson et al., 2001; Leiphart and Hart, 2001). One of these methods is based on finding empirical relationships between porosity and impedance obtained from inversion of seismic data. These methods have a drawback of being deterministic. The relationship between many reservoir properties and seismic

data may not always be deterministic (Todorov et al., 1998). Because deterministic methods do not have the ability to consider the non-linearity and ambiguity in the relationship to predict reservoir properties, statistical methods are more useful in predicting the non-linear behavior of a reservoir property as a function of seismic attributes (Hampson et. al., 2001). There are numerous examples of predicting reservoir properties using statistical methods such as multivariate analysis and neural networks (for example, Russell et al., 1997; Schuelke and Quirein, 1998; Pearson and Hart, 1999; Hart and Balch, 2000). Although these methods have been questioned about their validity, because they do not have a geological basis of reservoir property prediction, some applications of these methods (Ronen et al., 1994; Hirsche et al., 1997; Kalkomey, 1997; Hart, 1999; Pearson and Hart, 1999) have proven that they are indeed useful in reservoir property prediction in some situations. Statistical methods have the advantage of presenting a framework to link petrophysical data to the more error prone seismic data. These statistical methods can also characterize the uncertainty in the predicted reservoir property (Hirsche et al. 1997). Hampson et. al. (2001) have suggested using multivariate analysis to predict petrophysical properties away from wells. Multivariate analysis as the name suggests, uses multiple seismic attributes from the seismic data. The purpose of this method is to find a suitable relationship that connects the seismic attributes and the well log to be predicted at the well location. This relationship is found out by using statistical methods. Figure 4.1 shows a flow chart of the method employing both seismic and well log data for well log prediction.

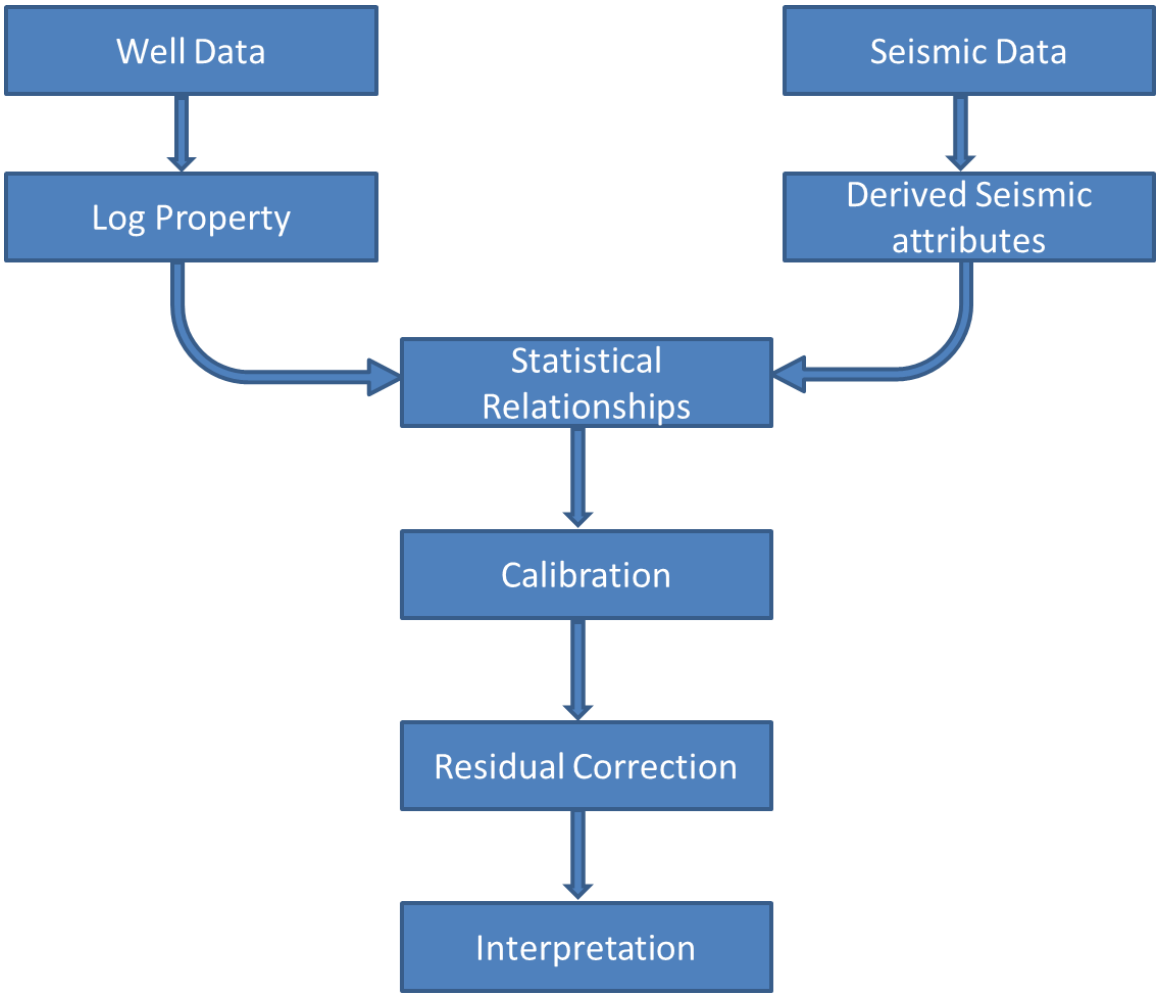

Figure 4.1: Flowchart of well log prediction from derived seismic attributes. Examples of attributes used are included in Figure 4.2 (adopted from Schultz et. al., 1994).

4.2 MULTI-ATTRIBUTE ANALYSIS FOR LOG PREDICTION

4.2.1 Multi-attribute analysis principles

Multi-attribute analysis is the method to predict a target petrophysical property from the seismic attributes derived from the inversion of seismic data. Prior to performing this analysis, in the preliminary stage of this study well log observations in

depth were tied to the seismic observations in time. Because this method depends on how well the well data is tied to the seismic data, a good correlation factor is needed before this method can be implemented. This is established in the Chapter 2, where I have demonstrated that well log data is tied to the seismic data and the seismic events are correlated to a good degree of accuracy. Given that there exists a good well to seismic tie, multi-attribute analysis can be used to obtain accurate statistical relationships between petrophysical properties from well log and seismic attributes derived from inversion of seismic data. In this section I briefly discuss the main points of the multi-attribute analysis method and neural networks that form the basis of log prediction. In broader terms the class of statistics used to relate seismic attributes to log properties is called multivariate analysis in which multi-variate inputs (several seismic attributes) are used to observe more than one outcome (of several log properties).

Seismic attributes are often defined as some mathematical transform of the seismic trace data (e.g. Taner et al., 1979). Seismic attributes have been broadly classified into two categories by Chen and Sidney (1997) which are namely, window-based attributes which are calculated within a particular window of time following a geologic layer in seismic data and horizon-based attributes which are continuously calculated along the seismic trace and have value at every time sample. Hampson et. al, (2001) have used horizon-based seismic attributes, which produce an output with the same number of samples as the input. In this method, a statistical relationship is developed through analysis of the seismic attributes data to improve the predictive power of the transform from a seismic trace to various petrophysical properties. Because the goal is to develop a predictive function from one data set to another data set, a prerequisite of developing a better statistical relationship between two data types is that they must be as independent of each other as possible until the point of developing the relation (Schultz et. al., 1994).

The statistical relationship between the input and the desired output can be linear or non-linear. Some of the examples of using linear statistical relationship for prediction of reservoir property are Gastaldi et al., (1997); Russell et al., (1997); Hart and Balch, (2000). Gastaldi et al., (1997) use geostatistical methods, developing empirical relationships between seismic attributes and reservoir properties to predict net pay sand. The advantages of using geostatistics is that it provides a means to combine different types of data and also gives a measure of uncertainty in the estimations of reservoir properties. Russell et al., (1997) use multivariate statistics to predict a well log property from three seismic attributes. In this method the log properties are represented as a function of the weighted convolutional sum of the seismic attributes. Using this method it was demonstrated that the log property prediction could be done to a greater accuracy without using geologic information. Hart and Balch, (2000) predicted the reservoir porosity by using seismic attributes derived from interpretation guided forward seismic modeling.

The common idea behind all these methods is deriving a relationship between the log properties and seismic attributes, which is used for prediction of log properties. In the previously discussed methods the predictive relationships are linear. A linear relationship means that when the log property is cross plotted against the seismic attribute, a linear equation is solved to obtain the coefficients of the linear regression fit. The coefficients of a linear relationship can be obtained using the method of least-squares. This idea of linear regression can be extended to include multiple seismic attributes, and the coefficients of the transform equation can be obtained by solving for the least squares problem of fitting the desired log property as a function of the input seismic attributes. Considering an example of predicting a log property (L) using three seismic attributes (A_1, A_2, A_3), the mathematical representation of this formulation is:

$$L(t) = w_0 + w_1A_1(t) + w_2A_2(t) + w_3A_3(t) \quad , \tag{4.1}$$

where $L(t)$ is the log property predicted, $A_n(t)$ are the derived seismic attributes, w_0, w_1, w_2, w_3, are the coefficients of the linear regression (Hampson et. al., 2001).

There are two drawbacks of the above formulation. First, it doesn't consider the fact that the frequency content of well logs is greater than the seismic frequency. Due to this reason finding a one-to-one correlation between every log property sample and seismic attribute sample is non-optimal. The second problem is that it predicts only the linear relation between the dependent (well log) and the explanatory variables (seismic attributes). These two issues are addressed in the following two paragraphs.

The first issue of optimality is solved by assuming that each sample on the well log is a representation of multiple neighboring points on the seismic attribute traces. This is solved by assuming that the log property is related to multiple seismic attributes through convolution. Convolution is an operation that relates multiple points of an operator to an output. Hence the Equation 4.1 can be represented as a convolution operation between the operator lengths w_i and the seismic attributes A_i as:

$$L = w_0 + w_1 * A_1 + w_2 * A_2 + w_3 * A_3 \ , \tag{4.2}$$

where w's are the operator lengths (weights) and A's are the seismic attributes and '*' represents convolution. The operator coefficients (weights) are obtained by minimizing the mean-squared prediction error function

$$(E) \quad -\sum(L \qquad)$$

The weights are obtained by solving for a set of normal equations (Hampson et. al., 2001), which can be represented in the matrix form as :

$$\begin{bmatrix} w^{1} \end{bmatrix} \begin{bmatrix} \sum & \sum A & \sum A & \sum A & \sum \\ \sum A & \sum & \sum A & \sum A & \sum A \\ \sum A & \sum & \sum A & \sum & \sum A \\ \sum A & \sum & \sum A & \sum & \sum \\ \sum & \sum & \sum & \sum & \sum A \\ \sum & \sum & \sum & \sum & \\ \sum & \sum & \sum & \sum & \\ \sum & \sum & \sum & \sum & \end{bmatrix}$$

where the vector on the left hand side of the Equation 4.4 consists of the convolution operators' coefficients (weights), the terms on the right hand side are comprised of the seismic attributes , and the

gth. Seismic attributes derived from impedance values are used for prediction of well log properties. The advantage of using seismic attributes derived from inverted impedance values along with the attributes derived from seismic data is that they incorporate non-linear behavior. Because there are many attributes that can be calculated, the selection of a subset that affects the log property the most has to be determined to decide which attributes are to be used for log prediction. In addition, it is required that

ideally the seismic attributes are independent of one another. This is achieved by stepwise regression method suggested by Draper and Smith (1996). This method is advantageous over trying every possible combination of the available attributes to find out which combination predicts the logs the best. It works on the principle that if initially an attribute is known to predict a particular log the best, then a combination of two attributes that best predicts the well log would have to include the first attribute. When this is generalized it can be stated that if a combination of *M* attributes is known to give the best prediction, then a combination with one more attribute would include the group of previous *M* attributes represented as a single attribute and the new attribute with their weights derived anew using the Equation 4.4. Following this approach, each time it reduces to solving for the least squared problem with effectively two attributes. This simple step reduces the computation cost for the selection of the optimum attributes to estimate the well logs. With the use of a larger number of attributes, the error is generally expected to come down to a given level. A nominal number of attribute selections can be obtained by plotting the error against the number of attributes. Observing from the error versus number of attributes plot, it can be determined that at what number of attributes the error doesn't change significantly. The point at which the there is no significant change in error minimization can be used to select the optimum number of attributes for multi-attribute analysis.

To deal with the second drawback, that is the limitation to linearity of the transform relation, Hampson et al. (2001) suggest the use of neural networks. Artificial neural networks have been used for log property prediction (for example, Himmer and Link, 1997; McCormack, 1991; Schultz et al., 1994). There are two approaches for using neural networks to predict well logs. The first one is called the multilayer feed-forward neural network (MLFN) the description of which can be found in many textbooks (for

example, Masters, 1994). MLFN has been used for well log prediction by Liu and Liu (1998). The network consists of three layers. The first is the input layer comprised of all the seismic attributes connected to a second layer of weights through as many nodes as attributes. A third layer, the output layer, has a single node representing the log being predicted and a hidden layer that lies in between the input and the output layer. The number of nodes for the hidden layer is decided by experimentation. The process of finding the optimum weights between different nodes is called training of the neural network (Hampson et al., 2001). The weights are estimated using a non-linear optimization technique. A second type of neural network is called probabilistic neural network (PNN) (Masters, 1994). It is based on mathematical interpolation techniques using neural networks to predict well logs. It is an easier method to understand than the MLFN whose nodes' weighing method is like a black box (Hampson et. al., 2001). In the present studies PNN is the neural network method used for well log prediction. In the following section I present the application of PNN to predict resistivity and porosity log properties.

4.2.2, Multi-attribute analysis applied to the prediction of resistivity and porosity

Resistivity and porosity normally derived from well log data are the two properties required for the estimation of gas hydrates saturation when using Archie's law. Because one of the goals of the present study is the estimation of gas hydrates saturation at all the trace locations on a seismic profile, these two well log properties (resistivity and porosity) are required at all the trace locations. Hence the target logs of the multivariate statistical analysis are resistivity and porosity. First I present the resistivity prediction using attributes calculated from impedance results obtained from prestack inversion. Porosity prediction follows a similar methodology as the one for resistivity prediction.

First consider the case of predicting resistivity. The input attributes are the P-impedance results that are obtained in the previous chapter from pre-stack inversion. The reason to use attributes derived from impedance values including attributes derived directly from seismic reflection strength is that it brings in non-linearity in the transform equations developed using the impedance derived attributes, thus increasing their predictive ability. Figure 4.2a shows all the attributes calculated form the P-impedance and seismic reflection strength. It also shows the correlation between the predicted results and the actual logs and their prediction error. Only few of the attributes are used in developing the transform equation. Using a larger number of attributes does not generally mean that they would increase the predictive power of the transform equations instead making the solving the Equation 4.4 more difficult as the number of operators increases with the increasing number of attributes. Figure 4.2b shows seven of the attributes derived from inverted impedances, to predict the well log property of resistivity using multi-attribute analysis. It is observed that the filtered P-impedance in the frequency range of 15-20-25-30 Hz has the least prediction error in predicting resistivity. This is the first seismic attribute used in the stepwise regression. Subsequently in each step, the seismic attributes with their prediction error progressively increasing are used for resistivity prediction. Figure 4.3 displays the error variation with the increasing number of attributes used for log prediction. Seven attributes calculated from P-impedance are used for the prediction of resistivity. It can be observed from Figure 4.3 that the well log prediction error decreases with increasing number of attributes. The rate of reduction in error decreases after seven seismic attributes. Hence seven seismic attributes are used for the petrophysical property prediction. It is observed from Figure 4.4 that the log predicted from multi-attribute analysis of the surface seismic data matches the actual resistivity well log to a great extent within the 1450-1560 ms on the well log. A cross-plot of the

predicted and measured resistivity values show a general trend of correlation. A few of the larger values of measured resistivity may be due to the anomalous resistivity values recorded during logging. The correlation between predicted and measured is 0.895 with an average error of 6.97%.

Figure 4.5 shows resistivity log prediction result obtained using probabilistic neural network training of the attributes derived from the P-impedance data. Using neural networks, it is observed that there is a marked improvement in the log prediction as compared to using multi-attribute analysis. It can be observed from figure 4.5 that the predicted log very closely matches the measured resistivity. The correlation is 0.997 with an average error of 1.17%, which is an improvement from the prediction from multi-attribute analysis applied to the attributes derived from P-impedance and reflection strength data. Because the predicted result is good, neural networks is used to predict resistivity in the complete seismic profile. The predicted resistivity is shown in Figure 4.6. Because gas hydrates have high electrical resistivity, their presence increases the resistivity of the host rocks. As expected it can be observed from the figure that the resistivity is high in the gas hydrates zone. I also observed that the highest predicted resistivity along the seismic profile is 21 ohm-m, while the highest resistivity observed on the resistivity log is considerably higher. It may be due the way the neural network method weighs the higher resistivity values. Because the probabilistic neural network method (PNN) that is used here for prediction of petrophysical properties uses a weighing method that inversely weighs the data according to the Euclidian distance between the training data (log data) and the seismic attributes, the higher resistivity values have a lower weight. Hence, they do not appear in the final values predicted along the seismic profile.

Using the similar multi-attribute analysis and neural networks methods that are used for resistivity prediction along the seismic profile, porosity is also predicted along the complete seismic profile. Neutron porosity is measurement of the amount of hydrogen present in the formation which can be either in the form of water or gas hydrates. Hence it is useful in providing estimates of formation porosity. It again uses a combination of multi-attribute analysis and neural networks to predict porosity. In the first stage multi-attribute analysis is used to predict porosity. Figure 4.7 shows the list of attributes derived from P-impedance and seismic reflection strength data used to predict porosity well log property. In this case the target log is porosity shown in the first column and the second column shows the list of seven attributes here. The attribute 'amplitude weighted phase' has the least training error. Figure 4.8a shows the neutron porosity predicted using multi-attribute analysis, using the attributes listed in the Figure 4.7. The correlation between the porosity predicted using these attributes and the observed porosity is 0.783, and the error is 4.03%. Figure 4.8b shows the neutron porosity predicted using neural networks. The correlation between the predicted porosity and the observed porosity is as high as 0.976, and the error is as low as 1.41%, which is an improvement over those achieved by using multi-attribute analysis of the attributes derived from P-impedance and seismic reflection strength data. It can be observed that the predicted porosity almost perfectly matches the observed porosity. Because the results at the well location are quite good, the same transform relationship between the seismic attributes and porosity is used to predict the porosity along the seismic profile. The predicted porosity along the seismic profile is shown in the Figure 4.9. The neutron porosity is the porosity type estimated at the well location and along the profile. Because now both porosity and resistivity values are obtained at all the sample points on seismic section, the next step is to estimate gas hydrates saturation.

4.3 GAS HYDRATES SATURATION ESTIMATION: PRINCIPLES AND RESULTS

The ultimate goal of my thesis work is the estimation of saturation of gas hydrates along the given seismic section. Saturation prediction of gas hydrates has been done using rock physics (for example, Ecker et. al, 2000; Chand et al., 2006), using empirical relationship between acoustic impedance and saturation (for example, Lu and McMechan, 2002), and using methods based on amplitude variation with offset (AVO) (for example, Tivella and Carcione, 2001). The method I use here is an application of the method described in details in Lee and Collett (2009) who have used a modified Archie's law (Archie, 1942) for gas hydrates saturation estimation at the well location using well logs. The reason to use this specific approach is that the Archie's law relating saturation to resistivity has been modified considering that fractures induce anisotropic behavior of electrical resistivity. Extensive fracturing in the region of study has been reported by Collett et al. (2008). Hence, this is the reason for using an anisotropic equation for estimating gas hydrates saturation. I apply the method to predict saturation at the well location and then extend it to predict saturation along whole seismic profile.

The basis of the method of predicting saturation of gas hydrates in the present study is the Archie's (Archie, 1942) equation that relates saturation to resistivity and porosity. The formation resistivity (R_0) is related to water resistivity (R_w) by

when all the pore spaces are occupied by brine. In this equation and are called Archie's parameters; is also known as the cementation factor. Water saturation can be calculated from the resistivity log using the relation:

$$\left(\frac{\quad}{\quad}\right)^{1/n}$$

where R_t is the true formation resistivity, obtained from the deep resistivity log data where invasion of drilling fluids is minimum, and n is the saturation exponent. The value of m varies between 1.3 to 2 for sandstones (Archie, 1942) and that of n varies between 1.715 and 2.1661 (Pearson et al., 1983). The values of the Archie's constants calculated in these works have been done assuming an isotropic medium (Lee and Collet, 2009). These values may not be appropriate for a medium containing gas hydrates. In the presence of gas hydrates the pore shape and pore space is changed. It has been shown in Collett et al. (2008) that there are fractures present in the Krishna-Godavari basin based on the X-ray images of the cores. Considering that the presence of factures may introduce anisotropy in rocks, Lee and Collett (2009) suggested the following values for anisotropic medium as $m = 2$ and $n = 3$ be used in Archie's realtion. R_w is calculated using Arp's formula (Arp, 1953),

$$(T \quad 7)/(T \quad 7)$$

where R_{w2}, are water resistivites at temperatures and respectively. In the present studies the reference resistivity and the temperature are the values at the

sea floor. The gas hydrates saturation based on resistivity was given by Lee and Collett, (2001) as

where S_w is defined in Equation 4.6.

Gas hydrates saturation was calculated using Equation 4.8. Resistivity and porosity values were obtained using multi-attribute analysis and neural network methods described in Section 4.2. The gas hydrates saturation calculated at the well location is shown in Figure 4.10. The saturation calculated using the above mentioned formulae were verified with the values obtained from the cores recovered from multiple drilling sites around the well. In the figure the blue line is the gas hydrates saturation predicted using the modified Archie's equation. It can be observed from Figure 4.10 that at three depth locations the calculated saturation approximately matches up against the measured saturation. The red dots on the plots are the saturation values obtained from the cores recovered from the wells drilled adjacent to the well from which well logs were recorded. It can be observed that the predicted saturation matches very well in three out of four situations. The mismatch in some of the points can be due to the fact that the cores are not exactly from the same location as the original well.

The estimation of gas hydrates saturation at all trace locations is done based on the same principles that are used for estimation of gas hydrates saturation at well location. Because the values of well log properties that are obtained from multi-attribute analysis and neural networks give the resistivity and porosity values at all trace locations, saturation estimation is extended to the whole seismic section. The result obtained appears as shown in Figure 4.11. The warm colors are the region with greater gas

hydrates saturation. Saturation of gas hydrates varies between 50-70 %. Because the saturation has been predicted using predicted well logs the saturation at depths greater than the depth of the well logs (the blue region in Figure 4.11) is not to be considered. Gas-hydrates are found at particular combinations of pressure and temperature known as the gas hydrates stability zone, which is chiefly dependent upon the depth beneath seafloor. It is observed from the resistivity log that there is an order of magnitude jump in the resistivity between 1400-1600 ms. This region coincides with the GHSZ, so the estimated gas hydrates saturation is valid in this region.

4.4 SUMMARY AND DISCUSSIONS

I have used a novel approach for the prediction of gas hydrates saturation using a combination of well logs and seismic attributes derived from both reflection amplitude and the impedance values derived from the P-wave reflections. The underlying relationship for saturation prediction is the Archie's equation, which arguably is suitably modified for anisotropy effects that are induced due the infiltration of gas hydrates in the pore spaces causing fracture. Porosity and resistivity values that are required for the estimation of gas hydrates saturation are predicted at trace locations away from the well using multi attribute analysis and neural networks. The saturation estimation at well location matches well with the saturation calculated from the cores. At one point the saturation does not match with the core measurement. This may be due to factors such as loss of pressure in the cores during recovery or anisotropic behavior of logs not predicted accurately at locations away from the well (Lee and Collet, 2009) or even the vertical resolution of the seismic reflection data. Finally, using the approach for saturation at well location, I have extended it to estimate saturation along the complete seismic profile.

Target	Attribute	Error	Correlation
Resistivity	inverted	13.465720	0.494805
Resistivity	Sqrt(inverted)	13.468457	0.494495
Resistivity	(inverted)**2	13.470811	0.494228
Resistivity	Log(inverted)	13.475118	0.493738
Resistivity	1 / (inverted)	13.501376	-0.490742
Sqrt(Resistivity)	1 / (inverted)	13.794060	-0.628233
Sqrt(Resistivity)	Log(inverted)	13.816192	0.631323
Sqrt(Resistivity)	Sqrt(inverted)	13.833294	0.631978
Sqrt(Resistivity)	inverted	13.853625	0.632102
Sqrt(Resistivity)	(inverted)**2	13.901905	0.630935
Log(Resistivity)	1 / (inverted)	14.616787	-0.752168
Log(Resistivity)	Log(inverted)	14.639491	0.753927
Log(Resistivity)	Sqrt(inverted)	14.659010	0.753828
Log(Resistivity)	inverted	14.682955	0.753155
Log(Resistivity)	(inverted)**2	14.741306	0.750295
Resistivity	Time	14.912352	-0.271772
Resistivity	Apparent Polarity	15.067817	-0.233343
Resistivity	Integrated Absolute Amplitude	15.100475	-0.224378
Resistivity	Average Frequency	15.127392	-0.216695
(Resistivity)**2	(inverted)**2	15.142688	0.293016
(Resistivity)**2	inverted	15.222445	0.294379
(Resistivity)**2	Sqrt(inverted)	15.267947	0.294662
Resistivity	Cosine Instantaneous Phase	15.293777	0.160862
(Resistivity)**2	Log(inverted)	15.316375	0.294649
Resistivity	Amplitude Envelope	15.345113	-0.139019
Resistivity	Amplitude Weighted Frequency	15.395356	-0.113551
Resistivity	Dominant Frequency	15.408924	-0.105609
(Resistivity)**2	1 / (inverted)	15.421670	-0.293644
Resistivity	Filter 5/10-15/20	15.443062	0.082261
Resistivity	Filter 35/40-45/50	15.446454	-0.079564

Figure 4.2a: List of attributes derived from seismic reflection and p-impedance data used for prediction of resistivity. The first column shows the well log property to be predicted by the derived attributes, the second column shows the seismic attributes used in prediction of the well log property. Third column shows the training error, which helps in deciding the attributes that are best suited for resistivity prediction. The first seven attributes (highlighted) with the least training error are chosen for resistivity prediction.

	Target	Final Attribute	Training Error
1	Resistivity	Amplitude Envelope(inverted)	12.448688
2	Resistivity	Integrated Absolute Amplitude(inverted)	10.179756
3	Resistivity	Quadrature Trace(inverted)	9.437803
4	Resistivity	Filter 45/50-55/60(inverted)	8.747048
5	Resistivity	Filter 5/10-15/20(inverted)	8.267747
6	Resistivity	Filter 35/40-45/50(inverted)	7.634403
7	Resistivity	Filter 15/20-25/30(inverted)	6.973784

Figure 4.2b: List of seven trace attributes used for prediction of resistivity. The first column shows the well log property to be predicted, the second column shows the attributes used in prediction of the well log property. The third column shows the training error. Observe that the attributes calculated from the inverted P-impedance have the least training error. The attribute with the lowest training error is the first attribute used in step-wise regression for resistivity prediction using multi-attribute analysis.

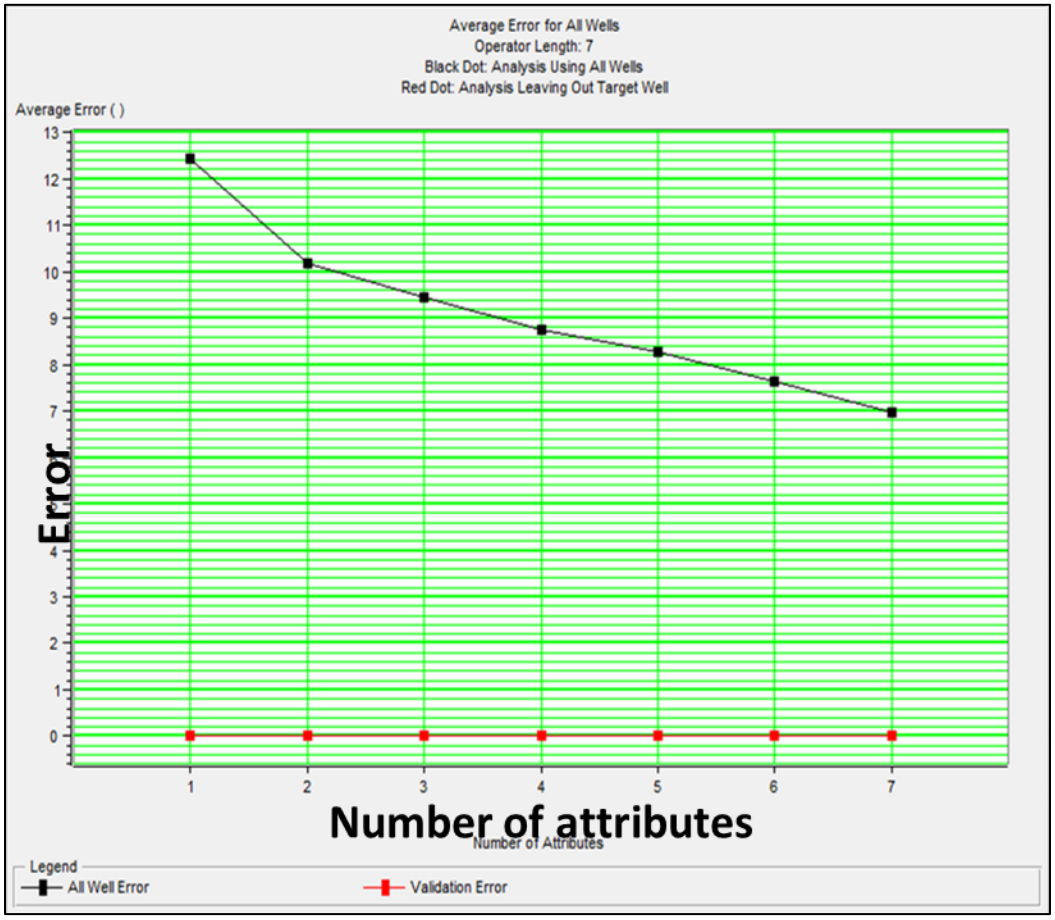

Figure 4.3: Well log prediction error versus number of attributes. The attributes are the same as in Figure 4.2a.The figure shows that with the increasing number of seismic attributes used in the prediction of well log property, the error decreases. Although a total of 21seismic attributes are generated from the inverted impedance values, only 7 attributes with the least training error are used for resistivity prediction using multi-attribute analysis. This is because the decrease in error is not significant when more attributes are used.

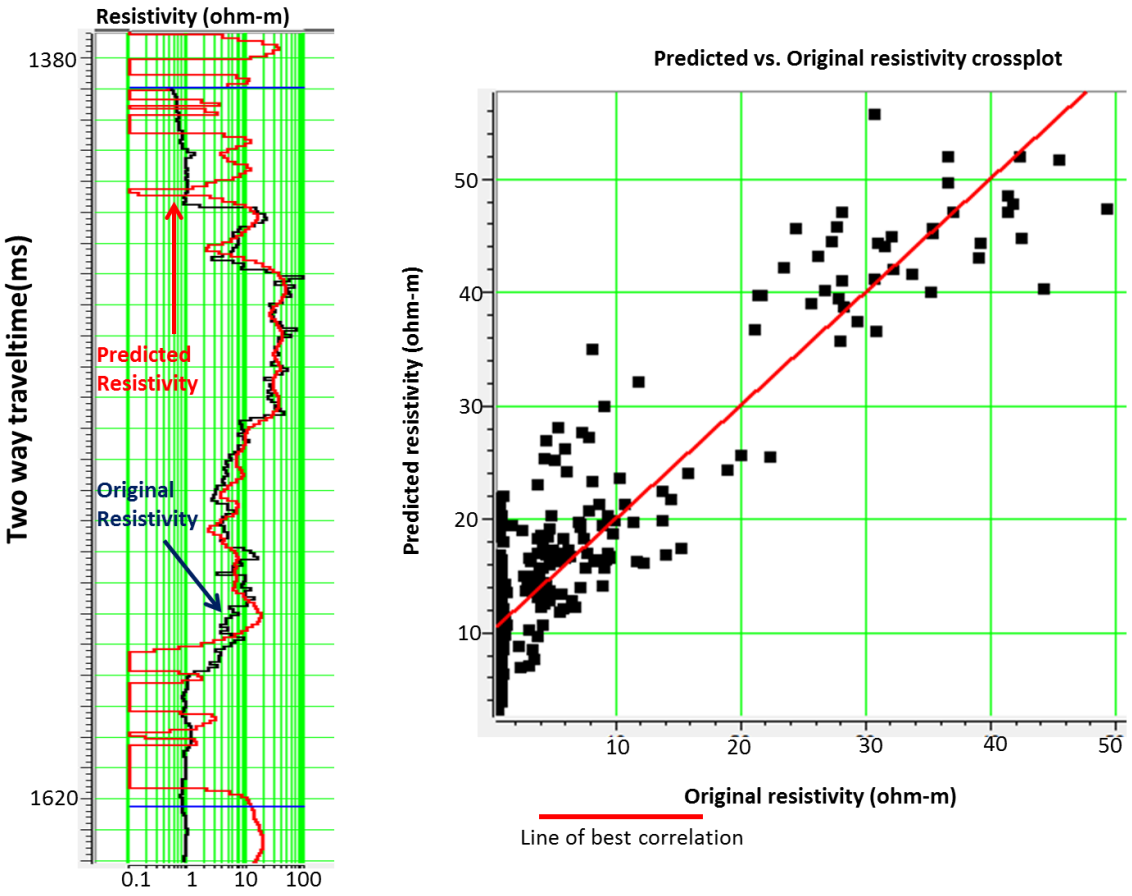

Figure 4.4: Plot on the left shows a comparison of observed resistivity log (blue) with the predicted resistivity log (red) using multi-attribute analysis. The correlation factor is 0.89, and the error is 6.97%. The figure on the right is the cross plot of the predicted (y-axis) against observed resistivity (x-axis). A general correlation trend (red line) between the actual resistivity and predicted resistivity is observed.

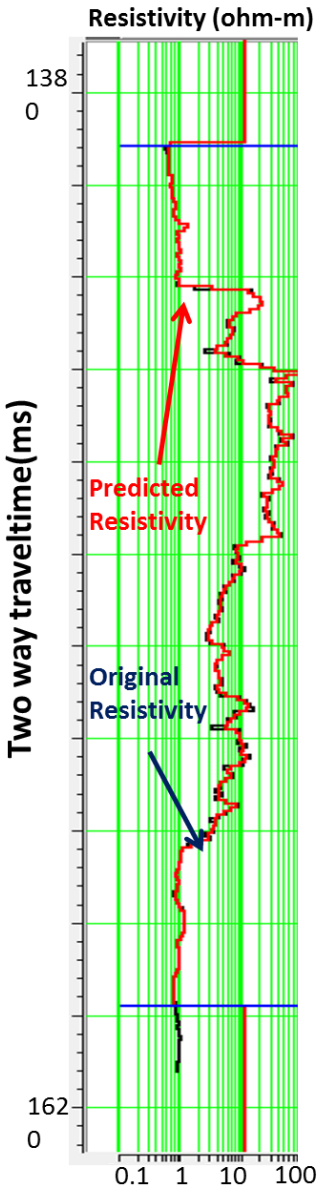

Figure 4.5: Predicted resistivity (red) using neural networks and the observed resistivity (black). The predicted resistivity (red) is almost same as the observed resistivity (black). The correlation factor is 0.99, and the error is 1.17%. Comparing the predicted well between the figure above and Figure 4.4, it is observed that there is a significant improvement in the well log prediction using neural networks. Hence neural networks is used to predict the resistivity along the seismic profile.

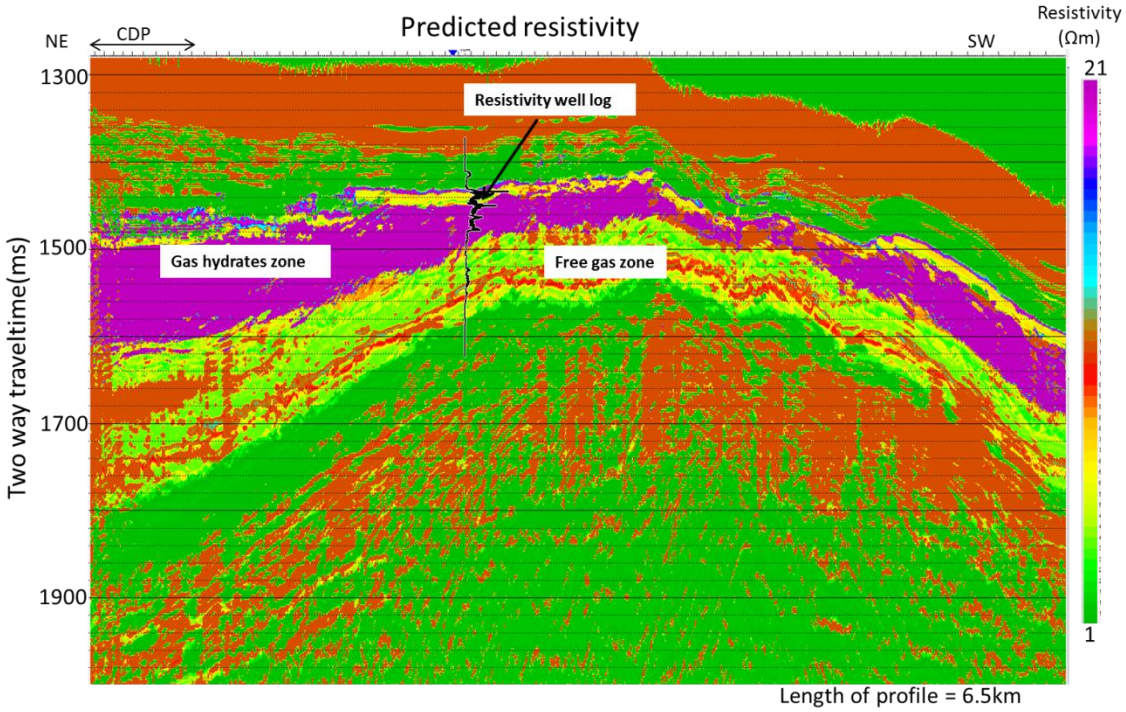

Figure 4.6: Predicted resistivity using neural networks along the section. The gas hydrates zone (magenta) is highly resistive. The original well log (black) is superimposed on the predicted resistivity section. The colorbar shows the resistivity range. The lowest resistivity value (green) is 1Ω and the largest values (purple) is 21Ω. The large resistivity values that are observed on the resistivity logs are not predicted using the neural-network.

	Target	Final Attribute	Training Error
1	(Porosity)**2	(inverted)**2	5.083000
2	(Porosity)**2	Filter 15/20-25/30	4.680735
3	(Porosity)**2	Time	4.445838
4	(Porosity)**2	Cosine Instantaneous Phase	4.327034
5	(Porosity)**2	Instantaneous Frequency	4.223327
6	(Porosity)**2	Derivative Instantaneous Amplitude	4.119845
7	(Porosity)**2	Amplitude Weighted Phase	4.027689

Figure 4.7: List of seven trace attributes used for prediction of porosity. The left panel shows the well log property that is desired to and the second column shows the attributes obtained from the impedance inversion of seismic data. The last column shows the training error. These are the 7 attributes with least training error that are used for neutron porosity prediction.

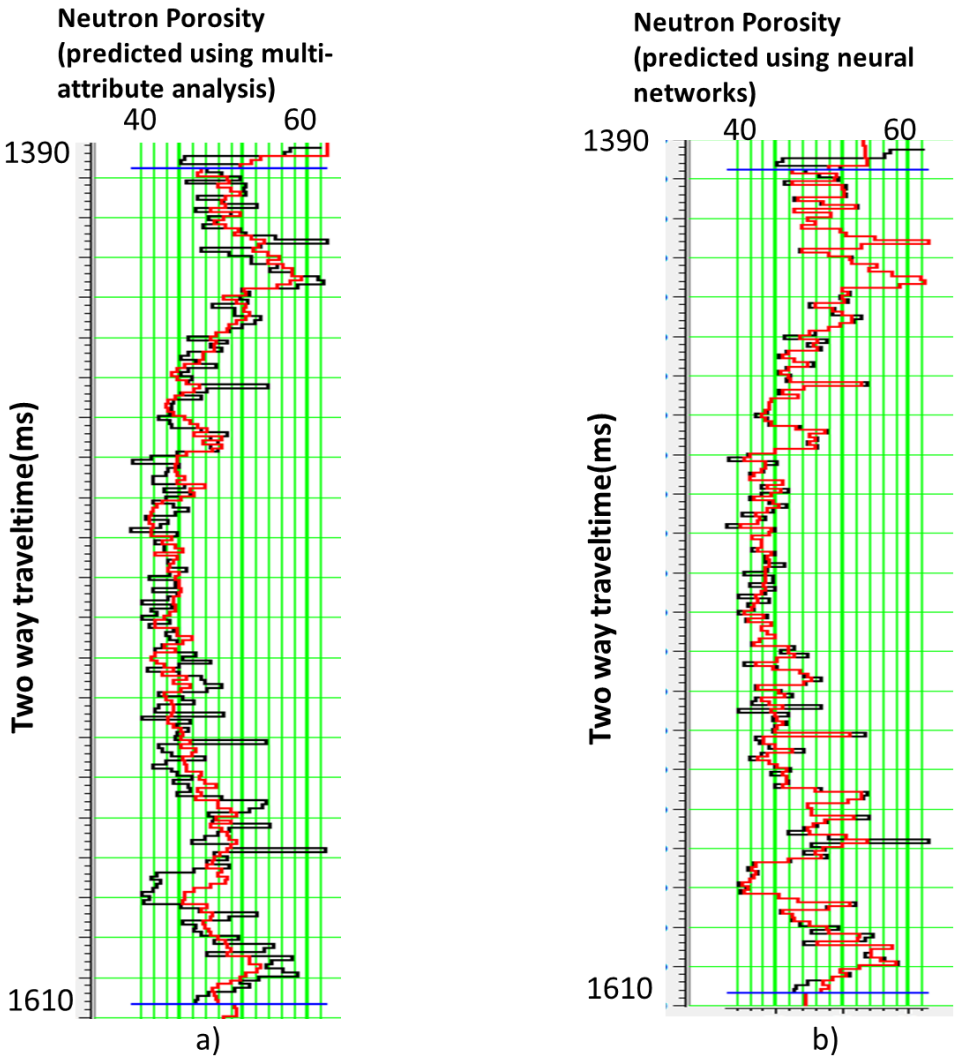

Figure 4.8: (a) Predicted porosity (red) from the attributes derived from trace amplitude and P-impedance data and the observed neutron porosity (black) using multi-attribute analysis. The correlation factor between the predicted and the original neutron porosity is 0.78 and the error is 4.02%. (b) Predicted porosity (red) and the original porosity (black) using neural networks. The correlation factor between the predicted and the original neutron porosity is 0.97 and the error is 1.41%. The predicted porosity in this case is almost same as the observed porosity. Hence neural networks are used to predict porosity along the seismic profile.

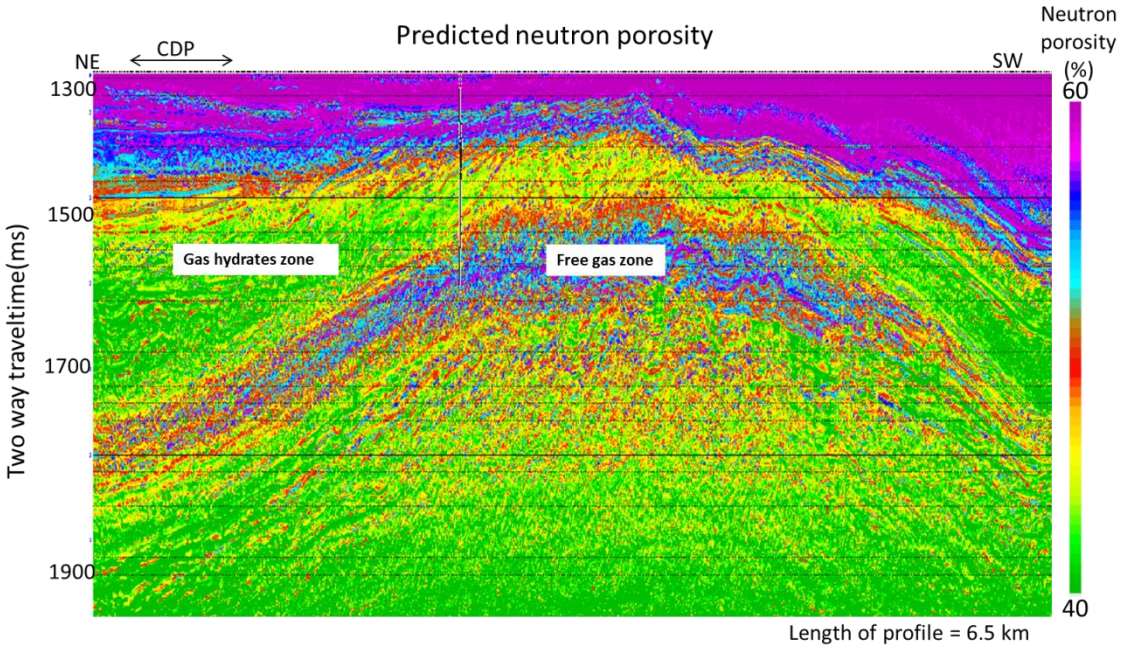

Figure 4.9: Predicted porosity using neural networks along the section. The colorbar at its lowest porosity (green color) is 40% neutron porosity and the largets porosity (purple) is 60 % neutron porosity. The presence of gas-hydrates reduces the neutron porosity. In the free gas region porosity increases. Netron porosity measures hydrogen index which is indicative of the amount of hydrogen in hydrocarbons in saturated pores, which is converted to porosity. Lower neutron porosity corresponds to region of larger gas-hydrates saturation.

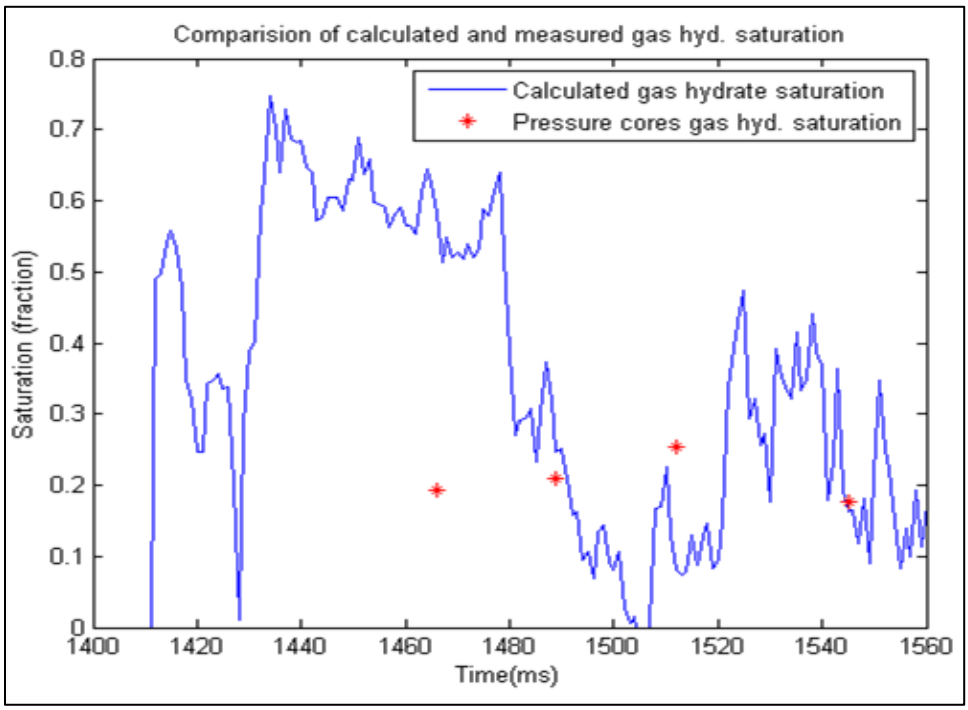

Figure 4.10: Estimated gas-hydrates saturation (blue line) at the well location against the measured saturation (red stars) from cores. The measured saturations are from cores recovered from surrounding wells. Anisotropy, loss in pressure in the cores are some of the reasons that the measured gas-hydrates saturation do not match up with the predicted saturation.

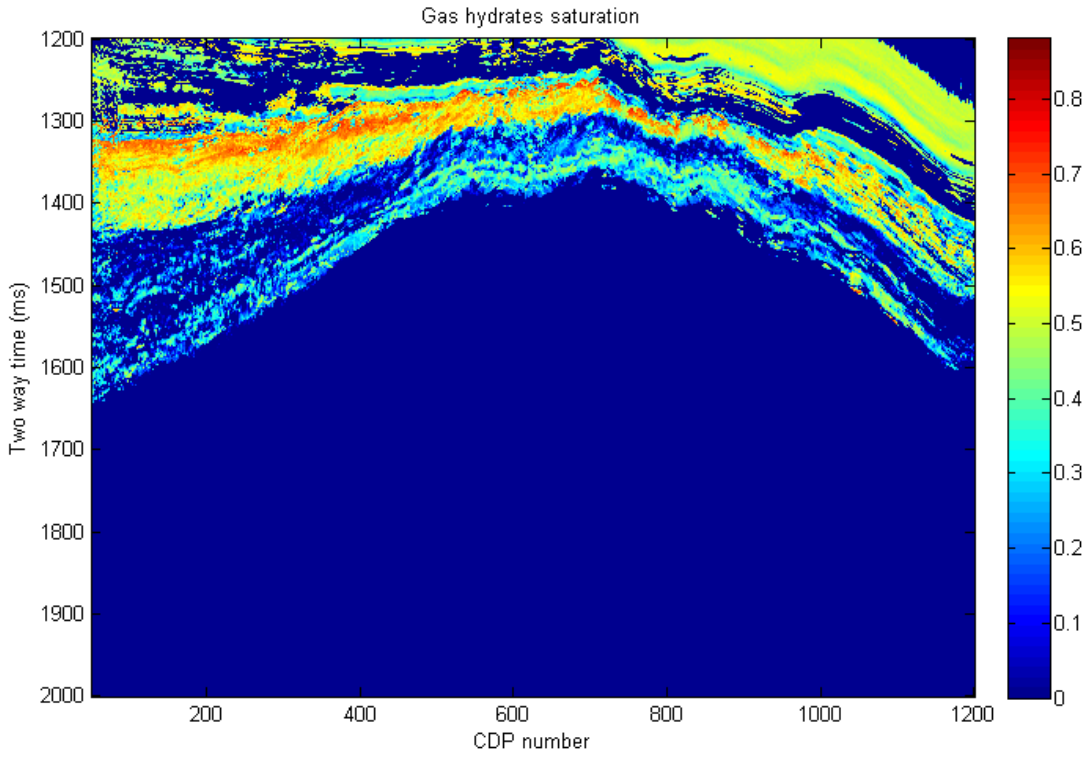

Figure 4.11: Gas hydrates saturation estimation at all trace locations. The warmer colors represent the region with higher saturation of gas hydrates. The higher gas-hydrates saturation occurs within the GHSZ. The GHSZ occurs between 1300-1450 ms two-way traveltime. Because the estimation of gas-hydrates saturation is based on the predicted resistivity and neutron porosity well logs, which have been guided by the interpreted horizons, it can be observed that there is no gas hydrates estimated below the deepest predicted horizon which here is the top of the free gas region. Hence the gas-hydrates saturation reads as zero in this region. Within the region of prediction the gas-hydrates saturation varies between 0.4 to 0.7.

4.5 REFERENCES

Anderson, J. K., 1996, Limitations of seismic inversion for porosity and pore fluid: Lessons from chalk reservoir characterization exploration: 66th Ann. Internat. Mtg., Soc. Expl. Geophys., Expanded Abstracts, 309–312.

Archie, G. E., 1942, The electrical resistivity log as an aid in determining some reservoir characteristics: J. Petr. Tech., 5, 1–8

Arp, J. J. (1953), The effect of temperature on the density and electrical resistivity of sodium chloride solutions, Trans. Am. Inst. Min. Metall. Pet. Eng., 198, 327– 330

Chand, Shyam, Tim A. Minshull, Jeff A. Priest, Angus I. Best, Christopher R. I. Clayton, and William F. Waite. 2006. "An Effective Medium Inversion Algorithm for Gas Hydrate Quantification and Its Application to Laboratory and Borehole Measurements of Gas Hydrate-bearing Sediments." Geophysical Journal International 166 (2): 543–552. doi:10.1111/j.1365-246X.2006.03038.x.

Chen, Q., and Sidney, S., 1997, Seismic attribute technology for reservoir forecasting and monitoring: The Leading Edge, 16, 445–456.

Collett, T., M. Riedel, J. Cochran, R. Boswell, J. Presley, P. Kumar, A. Sathe, A. Sethi, M. Lall, V. Sibal, and the National Gas Hydrate Program (NGHP) Expedition 01 Scientists, 2008, Indian NGHP Expedition 01 initial reports: Directorate General Hydrocarbon report.

Dorrington, K., and C. Link. 2004. "Genetic-algorithm/neural-network Approach to Seismic Attribute Selection for Well-log Prediction." GEOPHYSICS 69 (1): 212–221.

Draper, N. R., and Smith, H., 1966, Applied regression analysis: John Wiley & Sons, Inc.

Gastaldi, C., Biguenet, J., and De Pazzis, L., 1997, Reservoir characterization from seismic attributes: An example from the Peciko field (Indonesia): The Leading Edge, 16, 263–266.

Hampson, D. P., Schuelke, J. S., and Quirein, J. A., 2001, Use of multiattribute transforms to predict log properties from seismic data: Geophysics, 66, 220–236.

Hart, B. S., 1999, Geology plays key role in seismic attribute studies: Oil & Gas J., 97, July 12, 76–80.

Hart, B. S., and Balch, R. S., 2000, Approaches to defining reservoir physical properties from 3-D seismic attributes with limited well control: An example from the Jurassic Smackover Formation, Alabama: Geophysics, 65, 368–376.

Himmer, P., and Link, C. A., 1997, Reservoir porosity prediction from 3-D seismic data using neural networks: 67th Annual International Meeting, Society of Exploration Geophysicists, Expanded Abstracts, 842–845.

Hirsche, K., Porter-Hirsche, J., Mewhort, L., and Davis, R., 1997, The use and abuse of geostatistics: The Leading Edge, 16, 253–260.

Kalkomey, C. T., 1997, Potential risks when using seismic attributes as predictors of reservoir properties: The Leading Edge, 10, 11–15.

Korenaga, J., Holbrook, W. S., Singh, S. C., and Minshull, T. A., 1997, Natural gas hydrates on the southeast US margin: Constraints from full waveform and travel time inversion of wide-angle seismic data: J. Geophys. Res., 102, 15345–15365.

Lee, Myung W., and Timothy S. Collett. Gas hydrate estimation error associated with uncertainties of measurements and parameters. US Department of the Interior, US Geological Survey, 2001.

Lee, M. W., and T. S. Collett. 2009. “Gas Hydrate Saturations Estimated from Fractured Reservoir at Site NGHP-01-10, Krishna-Godavari Basin, India.” J. Geophys. Res. 114 (B7) (July 16): B07102. doi:10.1029/2008JB006237.

Leiphart, D. J., and Hart, B. S., 2001, Comparison of linear regression and a probabilistic neural network to predict porosity from 3-D seismic attributes in lower Brushy Canyon channeled sandstones, southeast New Mexico: Geophysics, 66, 1349–1358.

Liu, Z., and Liu, J., 1998, Seismic-controlled nonlinear extrapolation of well parameters using neural networks: Geophysics, 63, 2035–2041

Lu, Shaoming, and George A. McMechan. 2002. Estimation of Gas Hydrate and Free Gas Saturation, Concentration, and Distribution from Seismic Data: Geophysics 67 (2): 582–593.

Masters, T., 1994, Signal and image processing with neural networks: John Wiley & Sons, Inc.

McCormack, M. D., 1991, Neural computing in geophysics: The Leading Edge, 10, 11–15.

Ojha, Maheswar, Kalachand Sain, and Timothy A. Minshull. 2010. Assessment of Gas-hydrate Saturations in the Makran Accretionary Prism Using the Offset Dependence of Seismic Amplitudes: Geophysics 75 (2): C1–C6.

Pearson, C. F., Halleck, P. M., McGuire, P. L., Hermes, R., and Mathews, M., 1983, Natural gas hydrate: A review of in situ properties: J. Phys. Chem., 87, 4180–4185.

Pearson, R. A., and Hart, B. S., 1999, Convergence of 3-D seismic attribute-based reservoir property prediction and geologic interpretation as a risk reduction tool: A case study from a Permian intraslope basin: 69th Ann. Internat. Mtg., Soc. Expl. Geophys., Expanded Abstracts, 896–899.

Ronen, S., Schultz, P. S., Hattori, M., and Corbett, C., 1994, Seismic guided estimation of log properties, part 2: Using artificial neural networks for nonlinear attribute calibration: The Leading Edge, 13, 674–678.

Russell, B., Hampson, D., Schuelke, J., and Quirein, J., 1997, Multiattribute seismic analysis: The Leading Edge, 16, 1439–1443.

Schuelke, J. S., and Quirein, J. A., 1998, Validation: A technique for selecting seismic attributes and verifying results: 68th Ann. Internat. Mtg., Soc. Expl. Geophys., Expanded Abstracts, 936–939.

Schultz, P. S., Ronen, S., Hattori, M., and Corbett, C., 1994, Seismic guided estimation of log properties, parts 1, 2, and 3: The Leading Edge, 13, 305–310, 674–678, 770–776.

Specht, Donald, 1990, Probabilistic neural networks: Neural Networks, 3, 109–118.

Specht, Donald, 1991, Ageneral regression neural network: IEEETrans. Neural Networks, 2, 568–576.

Taner, M. T., Koehler, F., and Sheriff, R. E., 1979, Complex seismic trace analysis: Geophysics, 44, 1041–1063.

Todorov, Todor, Robert Stewart, Daniel Hampson, and Brian Russell. “Well Log Prediction Using Attributes from 3C–3D Seismic Data.” In SEG Technical Program Expanded Abstracts 1998, 1574–1576.

Tinivella, Umberta, and Jose M. Carcione. 2001. Estimation of Gas-hydrate Concentration and Free-gas Saturation from Log and Seismic Data: The Leading Edge 20 (2): 200–203.

Wood, W. T., Stoffa, P. L., and Shipley, T. H., 1994, Quantitative detection of methane hydrate through high-resolution seismic velocity analysis: J. Geophys. Res., 99, 9681–9695.

Wyllie, M. R. J., Gregory, A. R., and Gardner, G. H. F., 1958, An experimental investigation of factors affecting elastic wave velocities in porous media: Geophysics, 23, 459–493.

Yuan, T., Hyndman, R. D., Spence, G. D., and Desmons, B., 1996, Seismic velocity increase and deep-sea gas hydrate concentration above a bottom-simulating reflector on the northern Cascadia continental slope: J. Geophys. Res., 101, 13655–13671.

Chapter 5: Discussions and Conclusions

Gas-hydrates with their worldwide distribution and prolific reserve potential hold a significant promise as a future energy source. With their inferred presence detected from BSRs along the eastern India offshore region, and some parts of the western offshore, the Andaman and Nicobar islands, gas-hydrates represent an opportunity for India in particular (Sain and Gupta, 2012). To progress beyond the exploratory stage, it is important to estimate the economic feasibility of producing energy from gas-hydrates. Further, the quantification of gas-hydrates is an important step in the exploration of gas-hydrates. Quantification of gas-hydrates is the primary goal of my thesis. The method I have presented is novel because it is a combination of seismic inversion and seismic attributes derived from them. The predicted petrophysical properties (electrical resistivity and neutron porosity) were then used to estimate gas-hydrates saturation by applying a modified form of Archie's law (Lee and Collett, 2009). In the preceding chapters, I have presented the application of poststack inversion and prestack inversion and a discussion of their results, the use of multi-attribute analysis and neural-network to predict well logs and henceforth the presentation of the results and discussions on them. In this chapter I tie all my observations together to exhibit their logical progression and the role of each step leading to another to achieve the ultimate goal of gas-hydrates estimation.

Gas-hydrates have high bulk and shear moduli compared to other normally occurring pore-filling fluids such as water and hydrocarbons. Although there are different points of view if they are just pore filling material or if they also form a part of the load bearing matrix, it has been observed in the region of present study that their presence increases sonic propagation velocity. This has a direct effect on the bulk impedance on

the rocks saturated with gas-hydrates. Therefore, obtaining either P or S-impedance can become a useful tool for the analysis of the presence of gas-hydrates.

I have used an inversion software application called STRATA® available with the commercially available software Hampson-Russell® for seismic reflection data inversion. I have shown from the impedance inversion results obtained from the inversion of poststack seismic data, that the gas-hydrates stability zone, which is the region where gas-hydrates are expected to be found, indeed has larger P-impedance values compared to the regions above and below it. A limiting aspect of the impedance can be the frequency content of the seismic data. Low frequency content is missing due to seismic data acquisition limitations and subsequent seismic data processing. This missing low frequency content can be introduced into the inversion result by using an independent low frequency initial model. A low frequency initial P-impedance model was generated from the well logs using the interpreted seismic data and regional geologic data acting as a guide. Six prominent seismic horizons were interpreted and used to generate the initial impedance model. Inversion analysis at a borehole location shows high correlation between observed and inverted impedances. In my sensitivity analysis of the impedance inversion results on the starting impedance model, I have shown that the starting model despite of being low frequency, produces results comparable to high frequency initial impedance model. This is because the low frequency content in the inverted impedance is derived from other sources such as well log data, and the high frequency content is derived from the seismic data. The P-impedance inversion results can be interpreted in terms of the zones saturated with gas-hydrates. The resistivity well log showed that there is an order of magnitude increase in the electrical resistivity in the region corresponding to sediments saturated with gas-hydrates, which has been confirmed from the cores recovered from coring in nearby boreholes. The increase in sonic wave propagation

velocity can also interpreted as a result of the gas-hydrates. From the inverted P-impedance results it is observed that the high impedance zones are contiguous to the high resistivity zone. A direct observation that can be inferred from this is that the inverted P-impedance can be used as a technique to interpret the gas-hydrates zones. This interpretation technique is more effective when there are multiple data corroborating the same interpretation, which in this case is the evidence of the presence of gas-hydrates. Although P-impedance results obtained from poststack inversion gave a preliminary estimate of the large impedance zones corresponding to gas-hydrates bearing sediments' zone, but the resolution was not high enough to produce a detailed map. Hence, prestack inversion was performed to obtain improved results.

I used the prestack inversion application in Hampson-Russell®, namely STRATA®, to invert NMO processed CDP gathers for multiple impedance volumes. The data were appropriately processed to preserve the original seismic reflection amplitudes while minimizing noise. NMO removal and stretch muting was applied to avoid spurious low frequencies in the CDP gathers. The basis of prestack inversion application in Hampson-Russell® assumed a linearized expression for reelection coefficients as function of the angle. I generated angle gathers in the range of 0-45^{o}. Two wavelets, one for near angles (0^{o} -15^{o}) and another for far angles (15^{o} -45^{o}) were generated using both statistical and well log based methods for the generation of synthetic seismic and inversion analysis at the well location and also to obtain the scaling parameters to apply to inversion at other seismic trace locations. As expected the prestack inverted impedances had higher resolution compared to poststack inversion results. This is because the way prestack inversion is parameterized with P-wave and S-wave reflection coefficients and density as the model parameters for the inversion problem. The angle dependent seismic traces help in resolving the changes in seismic reflection amplitudes as

function of these model parameters. From the results obtained it can be inferred that the presence of gas-hydrates not only affects the P-impedance but also the S-impedance. From Vp/Vs obtained from the inversion it shows that there is a general decrease in the ratio in the gas-hydrates region which can be interpreted as the reduction in the amount of gas in the sediment pores. However, density is very poor criteria to look for gas-hydrates because the density of gas-hydrates and water are similar. Because there is no significant change in the density across the gas-hydrates bearing zone, it can be said that the changes in impedance is primarily due to the change in the seismic propagation velocities. Although these impedance values give an idea of the presence of gas-hydrates zones, they do not give any direct insight of any petrophysical property. The goal of this thesis is to obtain gas-hydrates saturation; hence, the impedance values generated were used for obtaining such petrophysical properties.

The inverted impedance provides a means to predict petrophysical properties at all seismic trace locations away from the well location. This approach addresses some of the limitations associated with the previous methods, which were either limited to gas-hydrates saturation estimation only at the well location, or using a semi-empirical relationship between seismic velocities and well log data to predict gas-hydrates saturation. The rock physics of gas-hydrates is not completely understood and hence does not provide reliable results. I have used a combination of multivariate analysis and neural-network calculations for the estimation of well log property from the derived attributed from inverted impedance profiles obtained from inversion. Using inverted impedance profiles to derive attributes is advantageous because these attributes are non-linear, so they increase predictive power of the relationships developed between the attributes and the petrophysical property. I used EMERGE®, the well log and seismic data merging application in Hampson-Russell®, to predict well log properties away from

the well location. Using the impedance values at the well location obtained from prestack inversion, EMERGE® calculated many seismic attributes. Through stepwise regression, an optimum number of best seismic attributes were selected to predict the well log property. Seven attributes with the least prediction error were chosen. Neural-network was used to predict the well logs. The advantage of using a neural-network is that introduces non-linearity in the predictive transform relationships. Higher correlation between the estimated and the observed petrophysical properties achieved using neural networks shows that it is better of the methods for well log prediction. The advantage of using a non-linear method (neural-networks) over a linear method (multi-attribute analysis) for well log prediction is evident from the results. The seismic attributes derived from impedance profiles as well as the reflection seismic data were the training data set and the well log values were the target data. The transform equations derived at the training of the neural-network were used to predict the target well log property at other seismic trace locations. A limiting factor in this study was the availability of only one well log due to which a validation of the neural-network was not possible. Electrical resistivity and neutron porosity profiles were obtained using these methods. The results showed that higher electrical resistivity coincides with the region which can be inferred as gas-hydrates stability zone from impedance inversion result. This is interpreted as the presence of gas-hydrates increasing the electrical resistivity of the gas-hydrates saturated sediments. Neutron porosity in the case of gas-hydrates corresponds very closely to actual reservoir porosity (Collett, 2001). The neutron porosity profile showed low porosity in the gas hydrates region, which is caused as the gas in the pores is used up in formation of gas- hydrates, which causes reduction of the fluid volume. The predicted electrical resistivity and neutron porosity supplied the necessary data required for estimation of gas-hydrates saturation.

Of all the well logs, the ones that are most responsive to the gas-hydrates are the sonic and resistivity. Hence, they are the best choices for use in developing predictive relationships. I used modified Archie's law (Lee and Collett, 2009) for the estimation of gas hydrates. Gas-hydrates may cause fracturing in the host rock (Collett et. al., 2008). Previously existing well log based methods to characterize gas-hydrates bearing sediments considered unfractured reservoirs. This leads to reported discrepancies in estimated gas-hydrates saturation (Lee and Colleet, 2009). It has been shown that the measured electrical resistivity varies with direction which is influenced by fractures filled with gas-hydrates (Kenedy and Hendrick, 2004). The anisotropic Archie's equation has modified values for its constants, cementation parameter m, and saturation exponent n. Using the values $m = 0.5$ and $= 2$, the saturation estimates were closer to observed saturation recovered from nearby wells. Assuming that the pores in the rocks within the GHSZ are either saturated with water or gas-hydrates, the saturation of gas-hydrates was obtained by subtracting the water saturation from net fractional sum of saturations value of 1. The estimated gas-hydrates saturation at the well location is consistent with the saturation calculated from the cores at three corresponding depths. The result at one location does not match. It is to be noted here that the cores are not recovered from the same borehole where logging was done. With the predicted resistivity and neutron porosity input into the modified Archie's law, gas-hydrates saturation is estimated along the seismic profile. The estimated saturation varies between 50%-70%. Thus I have demonstrated the application of a new method for estimation of gas-hydrates saturation using a combination of well log and seismic data.

Some of the advantages of this approach over the previously existing approaches are the inclusion of non-linear behavior in the transform relationships which gives better results. The use of impedance derived attributes as well as the use of neural-networks

both bring in non-linearity in the transform equations. The training of neural networks also some of the outlier resistivity values, hence avoiding error in saturation estimation. Although the frequency content of seismic data is limited to a narrow range as compared to well logs ,this issue is addressed by using a convolutional operator to link multiple points on the well log to one single data point on seismic derived attributes. The predicted saturation estimates do not consider the mechanism of gas-hydrates' interaction with the host sediments; hence the disadvantages associated with rock physics methods of saturation estimation were avoided. The deviation of the estimated saturation can be attributed to anisotropy in rocks, and in the present formulation, there is no scope to vary the values of m and n with the direction of measurement. Other sources of errors can arise out of measurement errors from the cores and the lost mass during the recovery of the cores as gas-hydrates are unstable when the pressure and temperature conditions are disturbed. The accuracy method presented is expected to improve with more well data, which can be used for validation of the neural-network.

References

Collett, Timothy S. “A Review of Well-log Analysis Techniques Used to Assess Gas-hydrate-bearing Reservoirs.” In Geophysical Monograph Series, edited by Charles K. Paull and William P. Dillon, 124:189–210. Washington, D. C.: American Geophysical Union, 2001.

Collett, T. S., Riedel, M., Cochran,J., R. Boswell, J. Presley, P. Kumar, A. V. Sathe, A. Sethi, M. Lall, V. Sibal, and the NGHP Expedition 01 Scientists, 2008, Indian National Gas Hydrate Program (NGHP) Expedition 01, Initial Report: Directorate General of Hydrocarbons, Ministry of Petroleum and Natural Gas, India.

Kennedy, W. D., and D. C. Herrick (2004), Conductivity anisotropy in shale-free sandstone, Petrophysics, 45, 38– 58.

Lee, M.W., Collett, T.S., 2009. Gas hydrate saturations estimated from fractured reservoir at Site NGHP-01-10, Krishna-Godavari Basin, India. J. Geophys. Res. 114, B07102.

Sain K., and H. K. Gupta, 2012. Gas hydrates in India: Potential and Development, Gondwana Research, 22, 645-657.